ON THE MASS TRANSPORT PHENOMENA IN PROTON EXCHANGE MEMBRANE WATER ELECTROLYZERS

Von der Fakultät Energie-, Verfahrens- und Biotechnik der Universität Stuttgart zur Erlangung der Würde eines Doktors der Ingenieurwissenschaften (Dr.-Ing.) genehmigte Abhandlung

Vorgelegt von

JULIO CÉSAR GARCÍA NAVARRO

aus Mexiko-Stadt, Mexiko

Vorsitzender:	Prof. Dr. rer. nat. Siegfried Schmauder
Hauptberichter:	Prof. Dr. rer. nat. K. Andreas Friedrich
Mitberichter:	Prof. Dr. Pierre Millet

Tag der mündlichen Prüfung: 18.06.2020

Institut für Gebäudeenergetik, Thermotechnik und Energiespeicherung der Universität Stuttgart

2020

There would be a day — there must be a day — when he (King Arthur) would come back to Gramarye with a new Round Table which had no corners, just as the world had none — a table without boundaries between the nations who would sit to feast there. The hope of making it would lie in culture. If people could be persuaded to read and write, not just to eat and make love, there was still a chance that they might come to reason.

— T. H. White, *The Once and Future King*

DECLARATION

I hereby declare that this thesis, titled "On the mass transport phenomena in proton exchange membrane water electrolyzers" and the work presented in it are my own. I confirm that:

- This thesis is submitted in partial fulfillment for the obtention of a *Doktor der Ingenieurwissenschaften* (*Dr.-Ing.*) degree at the University of Stuttgart.
- I have carried out all the work depicted here myself, including but not limited to, mathematical modeling, experimental methods and results, construction of testing setups and hardware, graphics and diagrams, and further considerations.
- The work depicted here was carried out during my stay as a doctoral student at the German Aerospace Center, Institute of Engineering Thermodynamics, between March 2015 and December 2018 under the supervision of Prof. Dr. K. Andreas Friedrich; additional technical supervision was provided by Dr. Mathias Schulze.
- I have acknowledged and properly referenced the published work of others I have consulted for the writing of this thesis, whether by direct quotations or by paraphrased statements and results.
- Wherever the thesis features work carried out by myself jointly with others, I have made clear which parts I carried out myself and which ones are contributions from others.
- All images, figures and diagrams depicted in this work are of my own making, unless otherwise stated; I declare that images, figures or diagrams featured in this thesis that come from external sources have been

correctly referenced and the copyright holders of such images, figures or diagrams have expressly granted me rights to reproduce them.

- At the time of writing, parts of this thesis had been featured in the following publications:

  J. C. Garcia-Navarro, M. Schulze, and K. A. Friedrich. "Understanding the role of water flow and the porous transport layer on the performance of Proton Exchange Membrane Water Electrolyzers." *ACS Sustain. Chem. Eng.* 7.1 (2019), pp. 1600–1610. DOI: 10.1021/acssuschemeng.8b05369.

  J. C. Garcia-Navarro, M. Schulze, and K. A. Friedrich. "Measuring and modeling mass transport losses in proton exchange membrane water electrolyzers using electrochemical impedance spectroscopy." *J. Power Sources* 431 (2019), pp. 189–204. DOI: 10.1016/j.jpowsour.2019.05.027.

  J. C. Garcia-Navarro, M. Schulze, and K. A. Friedrich. "Detecting and modeling oxygen bubble evolution and detachment in proton exchange membrane water electrolyzers." *Int. J. Hydrogen Energy* 44 (2019), pp. 27190–27203. DOI: 10.1016/j.ijhydene.2019.08.253.

Stuttgart, 2020

Julio César García Navarro

ACKNOWLEDGEMENTS

First and foremost, I would like to express my gratitude to the Institute of Engineering Thermodynamics of the German Aerospace Center, in particular to Prof. K. Andreas Friedrich for supervising my work during these past years. My thanks go to Dr. Mathias Schulze, who helped shape my work with his guidance and recommendations; to Dr. Indro Biswas for his continued support regarding administrative matters. Thank you to the Graduate Program of the German Aerospace Center for facilitating my attendance to graduate seminars and continued education symposia. Thank you to Prof. Pierre Millet for being my second supervisor, and to the National Council of Science and Technology (CONACYT) as well as the Secretariat of Public Education (SEP) for helping me finance my living expenses during my PhD studies.

I would also like to thank the technicians at the Institute of Engineering Thermodynamics for their technical support during the construction of the testing station, as well as the interns who assisted me with parts of the Matlab modeling and the experimental work. Special acknowledgements go to the part-time students for their support regarding the construction of the testing station and their further assistance in the laboratory. Special thanks to the users of Stack Exchange and the MathWorks forums for their continued (in)direct support regarding Matlab, Python and LaTeX. To my beloved wife Brenda for her moral support during my time as a doctoral student, for the interesting scientific discussions and for her continued support with programming matters. Many thanks to my family and friends for their emotional support.

CONTENTS

Declaration v

Acknowledgements vii

Symbols and abbreviations xii

Abstract xxi

Zusammenfassung xxiii

I INTRODUCTION AND EXPERIMENTAL SETUP

1 INTRODUCTION 3

1.1 PEM electrolysis . . . 3

1.2 Literature survey . . . 8

1.3 Outline of this thesis . . . 15

2 EXPERIMENTAL SETUP AND METHODS 19

2.1 Construction of testing station . . . 19

2.2 Materials used . . . 23

2.3 Experimental methods used . . . 24

2.3.1 Bubble evolution and detachment . . . 24

2.3.2 Gas permeation through porous transport layers . . . 27

2.3.3 Impedance spectroscopy of mass transport phenomena . . . 28

II RESULTS AND DISCUSSION

3 BUBBLE EVOLUTION AND DETACHMENT 35

3.1 Introduction . . . 35

3.2 Modeling . . . 36

3.2.1 Bubble force balance . . . 36

3.2.2 Sensitivity analysis . . . 40

3.3 Results and discussion . . . 41

3.3.1 Bubble motion through the flow field . . . 41

3.3.2 Bubble evolution on the electrode . . . 44
3.3.3 Bubble detection and counting . . . 46
3.3.4 Bubble force balance and sensitivity analysis . . . 51
3.4 Conclusion . . . 56
4 GAS PERMEATION THROUGH POROUS TRANSPORT LAYERS 59
4.1 Introduction . . . 59
4.2 Modeling . . . 61
4.2.1 Energy balance . . . 61
4.2.2 Two-phase pressure drop . . . 63
4.2.3 Permeability . . . 65
4.2.4 Permeability and tortuosity . . . 66
4.2.5 Confidence intervals and error propagation . . . 70
4.3 Results and discussion . . . 70
4.4 Conclusion . . . 83
5 IMPEDANCE SPECTROSCOPY OF MASS TRANSPORT PHENOMENA 85
5.1 Introduction . . . 85
5.2 Modeling . . . 86
5.2.1 EIS model . . . 86
5.2.2 Mass transport model . . . 90
5.2.3 Mass transport overpotential . . . 93
5.3 Results and discussion . . . 95
5.3.1 V(I) curves and EIS spectra . . . 95
5.3.2 Tortuosity and mass transport overpotential . . . 103
5.3.3 Sensitivity analysis . . . 109
5.4 Conclusion . . . 111

III FINAL REMARKS

6 FINAL REMARKS 115
6.1 General conclusions . . . 115
6.2 Further work . . . 118

IV BIBLIOGRAPHY

BIBLIOGRAPHY 123

V APPENDIX

A APPENDIX 137

A.1 Impedance spectroscopy of mass transport phenomena 137

A.1.1 Typical fit of the equivalent circuit 137

A.1.2 Fitted EIS data 138

About the author 139

SYMBOLS AND ABBREVIATIONS

ABBREVIATIONS

BOP	balance of plant
CCM	catalyst-coated membrane
$CI_{0.05}$	confidence interval with 0.05 significance
CPE	constant-phase electrode
EIS	electrochemical impedance spectroscopy
GUI	guest user interface
HER	hydrogen evolution reaction
HFR	high-frequency resistance
MEA	membrane electrode assembly
N115	Nafion™ 115
N117	Nafion™ 117
OER	oxygen evolution reaction
PEM	proton exchange membrane
PFD	process flow diagram
PTL	porous transport layer
VPS	vacuum plasma spraying

ROMAN SYMBOLS

A	electrode coated surface / m^2
A_{PTL}	PTL cross-sectional area / m^2

A_e	double layer surface / m²
B	channel width / m
C	Chisholm parameter / –
C_D	drag force coefficient / –
C_{dl}	double layer capacitance / F
C_g	gas concentration / mol m^{-3}
$C_{g,sat}$	saturated gas concentration / mol m^{-3}
C_{L1}	lift force 1 coefficient / –
C_{L2}	lift force 2 coefficient / –
C_σ	surface tension force coefficient / –
D_{eff}	effective gas diffusivity / m² s^{-1}
D_h	channel hydraulic diameter / m
D_h^{ff}	flow field channel hydraulic diameter / m
D_h^p	pipe hydraulic diameter / m
D_h^{pore}	PTL pore hydraulic diameter / m
$D_{particle}$	sintered particle diameter / m
D_{pore}	Pore diameter / m
D_0	gas diffusivity in a free medium / m² s^{-1}
d_b	bubble detachment diameter / m
$d_{b,0}$	bubble detachment radius with no current / m
d_w	diameter of a water molecule / m
dL_{ff}	differential flow field channel length / m
dL_{PTL}	differential PTL thickness / m
dL_p	differential pipe length / m
dP_g	differential gas pressure / Pa
dP_w	differential water pressure / Pa
dR_b	differential bubble radius / m

dV_g	differential gas velocity / m s^{-1}
dV_w	water vorticity / m s^{-2}
dz_w	differential height increase of water / m
E_{tn}	thermo-neutral potential / V
F	Faraday's constant / 96485 C mol^{-1}
F_{Bx}	corrected buoyancy force / N
F_{By}	buoyancy force (on the y-direction) / N
F_D	drag force / N
F_{L1}	lift force 1 / N
F_{L2}	lift force 2 / N
F_σ	surface tension force / N
f_D^g	Darcy friction factor for gas / –
f_D^{lg}	Darcy friction factor for the two-phase flow / –
f_D^w	Darcy friction factor for water / –
f_g	gas evolution efficiency (fraction of evolved gas in gas phase) / –
$\dot{g}$	terrestrial gravity acceleration / 9.81 m s^{-2}
H	head losses / J kg^{-1}
H_T	Henry coefficient at temperature T / mol m^{-3} Pa^{-1}
H_{other}	other head losses / J kg^{-1}
$H_{other,water}$	other head losses for water (permeability head) / J kg^{-1}
H_{PTL}	permeation through PTL head losses / J kg^{-1}
H_{perm}	permeation head losses / J kg^{-1}
H_{total}	total head losses / J kg^{-1}
H_{water}	water flow head losses / J kg^{-1}
H_{298K}	Henry coefficient at 298 K / mol m^{-3} Pa^{-1}
i	imaginary number / –

J	material flux / mol m^{-2} s^{-1}
j	current density / A cm^{-2}
j_{lim}	limiting current density / A cm^{-2}
K_g	total gas permeability / m^2
k	time constant of mass transport / s^{-1}
k_g	gas permeability in a free medium / m^2
k_w	water permeability in a free medium / m^2
$k_{g,r}$	relative gas permeability / –
k_τ^{ex}	excess tortuosity parameter / –
k^*	excess permeability / m^2
L	channel thickness / m
L_{ff}	flow field channel length / m
L_{PTL}	PTL thickness / m
L_p	pipe channel length / m
L_{pore}	calculated PTL pore length / m
L_1	inductance / H
l_{dl}	double layer thickness / m
l_e	electrode thickness / m
$l_{e,eff}$	effective electrode thickness / m
M_g	gas molar mass / kg mol^{-1}
M_w	water molar mass / kg mol^{-1}
m	van Genuchten–Mualem parameter / –
$\bar{m}$	measurement average / units of the measurement
$\dot{m}_g$	gas mass flow / kg s^{-1}
n	van Genuchten–Mualem parameter / –
n_{chan}	number of channels in the flow field / –
$n_{data\ points}$	number of data points / –

n_w	number of water molecules / –
P	pressure / bar
P_w	water vapor pressure / bar
P_c	capillary pressure / Pa
P_g	gas pressure / Pa
P_1	gas inlet pressure / Pa
P_2	water inlet pressure / Pa
P_3	outlet pressure / Pa
R	universal gas constant / 8.314 J mol^{-1} K^{-1}
R_b	bubble radius / m
R_{ct}	charge transfer resistance / Ω
R_h^{pore}	PTL pore hydraulic diameter / m
R_m	universal mass gas constant / J kg^{-1} K^{-1}
R_{mt}	mass transport resistance / Ω
R_p	pore radius / m
R_s	electrolyte resistance / Ω
Re	Reynolds number / –
Re_g	Reynolds number of the gas / –
S^*	pore water saturation / –
Sc	Schmidt number / –
Sh_1	Sherwood number of mass transfer from active sites to water / –
Sh_2	Sherwood number of mass transfer from water to bubble / –
T	temperature / K or °C
$t_{Student}$	inverse Student t coefficient / –
V_g	gas velocity / m s^{-1}

V_w	water velocity / m s^{-1}
$V_{w,mean}$	mean water velocity / m s^{-1}
$V_{w,mean,lim}$	limiting mean water velocity / m s^{-1}
v_g	molal volume of gas at normal boiling point / m^3 mol^{-1}
x	flow quality / –
Z_{Nern}	Nernst impedance / $\Omega\,cm^{-2}$
Z_{im}	imaginary impedance / $\Omega\,cm^{-2}$
Z_{re}	real impedance / $\Omega\,cm^{-2}$
z	number of electrons transferred / –

GREEK SYMBOLS

α	Carman–Kozeny coefficient / m^2
α_{vgm}	van Genuchten–Mualem coefficient / Pa^{-1}
β	contact angle between water and electrode / °
β_{lim}	parameter of the limiting current density / cm^2 A^{-1}
ΔH	enthalpy of dissolution / J mol^{-1}
Δz_w	total height increase of water / m
∂J	partial differential material flux / mol m^{-2} s^{-1}
∂P	partial differential pressure loss / Pa
∂P_g	partial differential gas pressure loss / Pa
∂P_{lg}	partial differential two-phase pressure loss / Pa
∂P_w	partial differential water pressure loss / Pa
∂t	partial differential time / s
$\partial \dot{x}$	partial differential position / m
ϵ	porosity / –
ϵ_{ap}	apparent porosity / –

$\varepsilon_r{}^{perm}$	relative electric permittivity / –
$\varepsilon_0{}^{perm}$	vacuum electric permittivity / F m^{-1}
η_{ac}	activation overpotential / V
η_{mt}	mass transport overpotential / V
η_{ohm}	ohmic overpotential / V
θ	bubble detachment angle / °
θ_{elec}	electrode coverage fraction / –
λ	gas mean-free path / m
μ_g	gas viscosity / Pa s
μ_w	water viscosity / Pa s
ν_w	water kinematic viscosity / m^2 s^{-1}
ρ	density / kg m^{-3}
ρ_g	gas density / kg m^{-3}
ρ_w	water density / kg m^{-3}
σ	surface tension between water and air / N m^{-1}
σ_{sd}	standard deviation of a measurement / units of the measurement
$\sigma_{sd,x}$	standard deviation of an independent variable x / units of x
$\sigma_{sd,y}$	standard deviation of a dependent variable y / units of y
σ_W	Warburg coefficient / $\Omega\,s^{-0.5}$
τ_{ap}	apparent tortuosity / –
$\tau_{ap,1phase}$	apparent tortuosity of a one-phase gas flow / –
τ_{int}	intrinsic tortuosity / –
ϕ_g	gas flow / m^3 s^{-1}, Nml min^{-1}, or l h^{-1}
ϕ_w	water flow / m^3 s^{-1} or l h^{-1}
$\phi_{w,max}$	maximum water flow / m^3 s^{-1} or l h^{-1}

$\phi_{w,min}$	minimum water flow / $m^3\ s^{-1}$ or $l\ h^{-1}$
φ	Lockhart–Martinelli parameter / –
φ_w	association parameter for water / –
ρ_g	gas density / $kg\ m^{-3}$
ρ_w	water density / $kg\ m^{-3}$
χ	Lockhart–Martinelli parameter / –
ω	frequency / Hz

ABSTRACT

Proton exchange membrane (PEM) water electrolysis is a technology designed to produce H_2 using only water and electricity as inputs; it has gained increased attention in industry and academia due to its advantages over incumbent H_2 generation processes (of which the most widely used are steam reforming and coal gasification) namely, low temperature, carbon-neutral and intermittent operation. PEM electrolysis can be instrumental for creating a hydrogen economy, although still much research needs to be carried out before widespread industrial adoption is achieved. PEM water electrolyzers suffer energy losses associated with the chemical reactions and the transport of charge and mass; of these phenomena, mass transport in PEM electrolyzers is the least understood subject, given the complex nature of the interaction of multiphase flows (mainly consisting of liquid water and evolved gases) through micrometric pores.

The subject of multiphase flow in water electrolysis and its relationship with the mass transport phenomena in PEM water electrolysis has been a prevalent subject in the literature. Despite numerous attempts at pinpointing the relationship between mass transport overpotential and the operating parameters, there is no clear consensus about which transport mechanisms dominate, nor about how the component design of PEM electrolyzers affects the mass transport. While the effect of temperature and current density on mass transport losses has been extensively studied and is well understood, there are significantly fewer studies that focus on the effect of water flow and pressure. Both water flow and pressure have a direct effect on mechanisms such as bubble nucleation and two-phase flows that occur in the porous structures within a PEM electrolyzer (electrodes and porous transport layers, PTLs).

In this work, I studied the effect of water flow and pressure on the mass transport phenomena in PEM electrolyzers. Chapters 1 and 2 provide an introduction to the topic as well as a description of the materials and experimental setups used. Chapter 3 of this thesis depicts the visualization and modeling of bubble nucleation in an operating PEM electrolyzer. I discovered that bubble detachment radii are largely independent of water flow and I identified two types of bubbles: bubbles that detach after reaching a critical size, and bubbles that fill up the pores of a PTL before detaching. Chapter 3 consists of the measurements I carried out regarding the transport of evolved gas through the water-filled pores of a PTL, where I observed that water flow severely impedes the gas transport through the pores and that such impediment is related to a shear stress exerted by the water flow on the pores. Chapter 5 shows the measuring of mass transport losses using electrochemical impedance spectroscopy (EIS) on an operating PEM electrolyzer; the results indicate that pressure and water flow affect the diffusion of gas in the electrode and that the mass transport overpotential depends on design parameters of the PEM electrolyzer, such as electrode thickness and hydrophobicity.

Overall, I derived a theoretical framework based on the assumption that the evolved gas in a PEM electrolyzer permeates through the PTL after diffusing from the active sites to the bubble nucleation sites. Such framework, constructed on the basis of the models regarding gas transport in porous media, can be used to explain the mass transport loses in a PEM electrolyzer that arise from operating with increased water flows and pressures. The model I derived can be used in future work as a guideline to optimize the components of a PEM electrolyzer, in particular regarding the hydrophobicity and pore size distribution of PTLs as well as the composition of the catalyst ink to produce the electrodes. Moreover, this work can also be used to further understand the mass transport losses and optimize the operation of PEM electrolyzers to decrease the energy consumption of H_2 generation.

ZUSAMMENFASSUNG

Protonenaustauschmembran (PEM)-basierte Wasserelektrolyse (PEM-Elektrolyse) ist eine Technologie zur Erzeugung von H_2 mit lediglich Wasser und Elektrizität als Input. PEM-Elektrolyse hat Aufmerksamkeit in Industrie und Wissenschaft aufgeregt aufgrund seiner Vorteile wie Niedrigtemperatur-, klimaneutraler und intermittierender Betrieb gegenüber der am häufigsten verwendeten Verfahren zur Erzeugung von H_2 (insbesondere Dampfreformierung und Kohlevergasung). PEM-Elektrolyse kann für die Etablierung einer Wasserstoffwirtschaft von entscheidender Bedeutung sein, obwohl noch viel Forschungsarbeit geleistet werden muss, bevor eine breite industrielle Akzeptanz erreicht werden kann. PEM-Wasserelektrolyseure erleiden Energieverluste im Zusammenhang mit den chemischen Reaktionen sowie dem Ionen- und Massentransport. Von diesen Phänomenen ist der Massentransport in PEM-Elektrolyseuren das bisher am wenigsten verstandene Thema, da die Interaktion von Mehrphasenströmungen (hauptsächlich bestehend aus flüssigem Wasser und entwickelten Gasen) durch mikrometrische Poren komplex ist.

Das Thema der Mehrphasenströmung und seine Beziehung zu den Massentransportphänomenen bei PEM-Wasserelektrolyseuren ist seit Jahren ein vorherrschendes Thema in der Literatur. Trotz zahlreicher Versuche, den Zusammenhang zwischen dem Überpotential des Stofftransports und den Betriebsparametern zu bestimmen, besteht jedoch kein eindeutiger Konsens darüber, welche Transportmechanismen dominieren und welche Rolle das Komponentendesign von PEM-Elektrolyseuren auf den Stofftransport spielt. Während die Auswirkung von Temperatur und Stromdichte auf Stofftransportverluste ausführlich untersucht wurde und allgemein bekannt ist, gibt es bedeutend weniger Studien, die sich auf die Auswirkung von Wasserfluss und Druck konzentrieren. Sowohl der Wasserfluss als auch der Wasserdruck wirken sich direkt

auf Mechanismen wie die Keimbildung von Blasen und Zweiphasenströmungen aus, die in den porösen Strukturen eines PEM-Elektrolyseurs (Elektroden und poröse Transportschichten, PTL) auftreten.

In dieser Arbeit wird der Einfluss von Wasserfluss und Druck auf die Massentransportphänomene in PEM-Elektrolyseuren untersucht. Kapitel 1 und 2 enthalten eine Einführung in das Thema sowie eine Beschreibung der verwendeten Materialien und Versuchsmethoden. Kapitel 3 beschreibt die Visualisierung und Modellierung der Blasennukleation in einem laufenden PEM-Elektrolyseur. Es konnte die weitgehende Unabhängigkeit der Blasenablösungsradien vom Wasserfluss gezeigt sowie zwei Arten von Blasen identifiziert werden: Blasen, die sich nach Erreichen einer kritischen Größe ablösen, und Blasen, die die Poren einer PTL vor dem Ablösen auffüllen. Kapitel 4 besteht aus den Messungen zur Untersuchung des Transports von entwickeltem Gas durch die wassergefüllten Poren einer PTL. Dabei konnte eine starke Behinderung des Gastransports durch die Poren aufgrund des Wasserflusses beobachtet sowie ein Zusammenhang mit einer ausgeübten Scherspannung vom Wasserfluss auf die Poren nachgewiesen werden. Kapitel 5 zeigt die Messung von Stofftransportverlusten mittels elektrochemischer Impedanzspektroskopie (EIS) an einem sich im Betrieb befindenden PEM-Elektrolyseur. Die Ergebnisse zeigen eine Beeinflussung der Gasdiffusion durch Druck und Wasserfluss sowie eine Abhängigkeit des Massentransport-Überpotentials von Konstruktionsparametern des PEM-Elektrolyseurs wie Elektrodendicke und Hydrophobizität.

Insgesamt konnte ein theoretisches Gerüst abgeleitet werden, das auf der Annahme basiert, dass das entwickelte Gas in einem PEM-Elektrolyseur die PTL durchdringt, nachdem es von den aktiven Stellen zu den Blasen-Keimbildungsstellen diffundiert ist. Ein solches Gerüst, das auf der Grundlage der Modelle für den Gastransport in porösen Medien aufgebaut wurde, kann verwendet werden, um die Stofftransportverluste in einem PEM-Elektrolyseur zu erklären, die durch den Betrieb mit erhöhten Wasserströmen und Drücken entstehen. Das Modell kann in zukünftigen Arbeiten als Richtlinie zur Optimierung der Komponenten eines PEM-Elektrolyseurs verwendet werden, insbesondere

hinsichtlich der Hydrophobizität und Porengrößenverteilung von PTLs sowie der Zusammensetzung der Katalysatortinte zur Herstellung der Elektroden. Darüber hinaus kann diese Arbeit auch verwendet werden, um die Massentransportverluste besser zu verstehen und den Betrieb von PEM-Elektrolyseuren zu optimieren, um den Energieverbrauch bei der Erzeugung von H_2 zu senken.

Part I

INTRODUCTION AND EXPERIMENTAL SETUP

General introduction to the topic of two-phase transport phenomena in PEM electrolyzers; experimental setup used for the preparation of this thesis.

1

INTRODUCTION

1.1 PEM ELECTROLYSIS

Proton exchange membrane (PEM) water electrolysis is a technology that has gained a lot of attention in recent decades following the achievements made with the proton exchange membrane fuel cells. PEM electrolysis is regarded as a promising technology for energy storage in conjunction with renewable energy production, such as wind or solar energy ([8][17]). PEM electrolyzers allow for a fast dynamic response to grid fluctuations (including surplusses of electricity on high solar or wind power production) and a simplified system design in comparison with alkaline electrolysis. To achieve the target of distributed hydrogen from water electrolysis with a production cost of $4 per gallon of gasoline equivalent by 2020 [22], significant improvements regarding electric efficiency are required. Therefore, it is necessary to gain a full understanding about the underlying causes of system overpotentials so that effective optimization strategies can be derived.

A PEM water electrolyzer is an electrochemical device that uses water and electricity to produce H_2 and O_2. The main components of a PEM water electrolyzer are:

- Anode. In this electrode the oxygen evolution reaction (OER) takes place:

  $$H_2O \xrightleftharpoons{\text{Ru, Ir or } IrO_2} 2H^+ + \frac{1}{2}O_2$$

The anode's catalyst is typically made of ruthenium, iridium or a mixture thereof, sometimes using the metallic form or as an oxide.

- Cathode. In this electrode the hydrogen evolution reaction (HER) takes place:

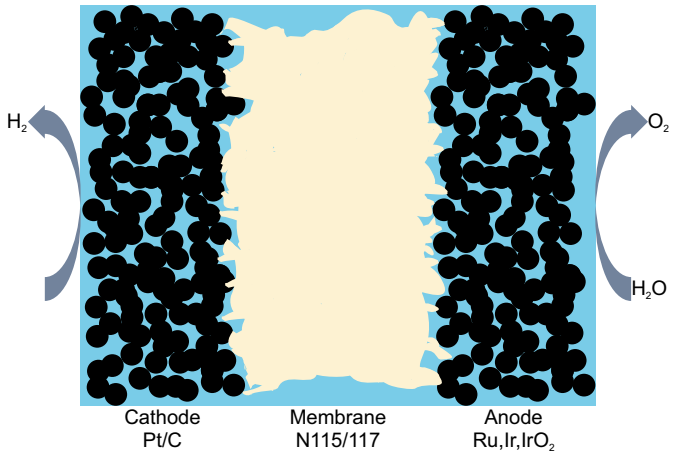

Figure 1.1: Diagram of an MEA of a PEM water electrolyzer, showcasing the anode, cathode and membrane. An electric current needs to be applied between anode and cathode to drive the splitting of water into H_2 and O_2; the minimum cell potential required by the electrochemical reaction is 1.23 V.

$$2H^+ \overset{\text{Pt/C}}{\rightleftharpoons} H_2$$

The cathode's catalyst is typically made of carbon-supported platinum.

- Membrane. It is made of a proton-conducting membrane (Nafion™) and it is used as an electrolyte i.e., to facilitate the transport of H^+ between anode and cathode.

During manufacture, the anode, cathode and membrane are typically bound together to ensure a good electric contact between the membrane and each of the electrodes; one manufacturing method consists of fabricating each electrode by coating the membrane with a mixture of the respective catalyst (Ru, Ir, or Pt) and ionomer (which is typically comprised of solubilized membrane material). This manufacturing method (called catalyst-coated membrane, or CCM) produces a membrane-electrode assembly (MEA). Figure 1.1 shows a diagram of a MEA of a PEM water electrolyzer.

Aside from the MEA, a typical PEM water electrolyzer includes the following elements:

- Porous transport layers (PTL). The porous transport layers provide electric contact between the electrodes and the flow fields while also offering a pathway for water and gases to flow through. Typical PTL materials include titanium-based porous structures (for the anode, used for its corrosion resistance) and porous carbon substrates such as carbon paper or cloth (only usable for the cathode); the design variables of a PTL, such as porosity, pore size and thickness, affect both the mass transport and the electric resistance of a PEM electrolyzer.

- Flow fields. They are used to distribute the water flow as evenly as possible and to allow the evolved gases to exit the electrodes. The design of the flow fields depends on the type of MEA used (and the type of electrochemical cell); parallel flow fields (such as the ones depicted in Figure 1.2) minimize the friction losses of the water flow and spread the water flow evenly across the electrode, while single-channel flow fields (used in PEM fuel cells) maximize the residence time of the reactants.

- Gaskets. These components seal off the cell from the environment; they stop water and gases from exiting the system and prevent the reactants on each electrode from coming in contact. Gaskets are typically made from fluorinated natural rubber (Viton®), teflon or copolymers, either carbon-based (EPDM) or silicon-based (MVQ); the choice of gasket material responds to the design of the flow fields and end plates, as well as the operating temperature and pressure.

- End plates. They are used to hold the rest of the elements together by tightening both plates using screws mounted with a specific torque to guarantee an even electric contact between all the elements as well as allowing the gaskets to seal off the PEM electrolyzer from the environment.

Figure 1.2 shows an exploded cell view of a complete PEM water electrolyzer, including MEA, PTLs, flow fields, gaskets and end plates.

PEM electrolysis represents significant advantages as a process for producing H_2 (e.g. for fuel and chemical applications) over incumbent methods of

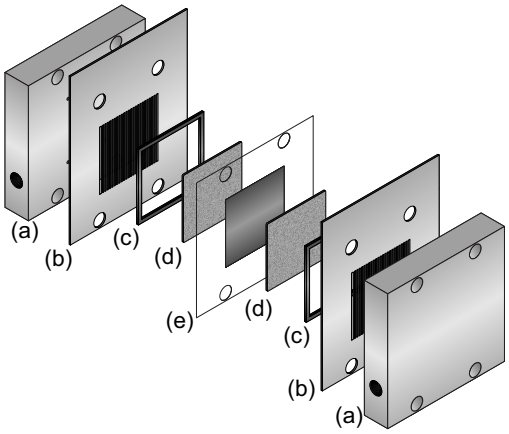

Figure 1.2: Exploded cell view of a PEM electrolysis cell. a) SS316 end plates, b) Ti flow fields, c) Viton® gaskets, d) sintered Ti PTLs, and e) MEA.

H_2 production (the most popular being steam reforming and coal gasification): the operation of PEM water electrolyzers can be carbon-neutral (depending on the source of the electricity), is carried out at low temperatures (< 100°C) and can be intermittent, allowing certain level of synergy with renewable energy sources namely, by mitigating their curtailment from the electric grid by grid operators. PEM electrolyzers are not without limitations; there are different sources of energy losses namely, ohmic losses (caused by the relatively large electric resistance of the membrane), kinetic losses (caused by the nature of the catalyst and the availability of active sites in an electrode) and mass transport losses (caused by the interaction of water and gas streams in the PTLs and the electrodes).

Understanding the performance of a PEM water electrolyzer, more specifically how the operating conditions affect it, is a crucial step toward optimizing the components of an electrolyzer stack [7] by e.g. lowering the production costs and allowing a wider integration of H_2 storage technologies in the renewable energy landscape. There are four main operating parameters of a PEM electrolyzer: temperature, pressure, current density, and water flow. Whereas the choice of current density and temperature obey higher-order constraints (stack design and materials choice, respectively, see [7]), water flow and pres-

sure are parameters that are decided upon during the system design phase. Operation at high H_2 pressure leads to lower costs of pressurizing (to store H_2 and use it in e.g. fuel cell vehicles), and the choice of water flow is directly related to the cooling design and capacity to demineralize the water stream to prevent premature degradation of the stack. There are three recognizable operation modes in a PEM electrolysis stack, dictated by the current density: kinetic control, ohmic control and mass transport control. During kinetic control (at current densities below 0.3 A cm^{-2}), the main overpotential is related to the HER and OER. Between 0.3 and 1.5 A cm^{-2}, the performance of the stack is strongly determined by cell electric resistance. At current densities above 1.5 A cm^{-2}, mass transport effects can be important; all three operation modes generally overlap [17]. It is favorable that a PEM electrolyzer be operated at high current densities to decrease stack size, therefore reducing the capital costs associated with its manufacture [7].

One of the greatest challenges in the subject of PEM electrolysis is the characterization and understanding of the mass transport losses, mainly caused by the interaction between water and the evolved gases (with O_2 in the anode and with H_2 in the cathode). Water is present in each site of the electrode surface due to either being a reactant (anode) or being dragged electro-osmotically through the ion-conducting membrane (cathode); consequently, an active site will be the converging point of two material flows in two different phases. Furthermore, water is typically used as a coolant as well as a reactant: a PEM electrolyzer will generate waste heat and using the same flow channels for cooling as well as reactant supply greatly simplifies cell design. The (volumetric) water flow that is circulated in a PEM electrolysis cell is therefore much larger than the stoichiometrically required amount. The encounter of water and gas streams in a PEM electrolyzer can occur in three different sections: around the electrodes, inside the pores of the PTLs and in the flow field. The interaction of gas and water will cause friction between both phases, and such friction will be reflected in an energy loss that needs to be compensated to keep a constant operation. It is therefore paramount that we focus our attention on how mass

transport affects the performance of a PEM electrolysis stack at high current densities and what role the operating conditions (temperature, pressure, water flow) and stack design play.

1.2 LITERATURE SURVEY

The subject of multiphase flow in water electrolysis, as well as the implications in the efficiency of water electrolysis, has been a prevalent subject in the literature. Roy et al. measure an overpotential caused by bubbles adhering to the electrodes in an alkaline water electrolyzer [77]; they presented an equation to calculate a "bubble voltage loss". This bubble voltage loss increasses polynomically with current density. Roy et al. base their work on the publication by Nagai, who introduces the study of bubble formation as a result of electrode spacing [66]. Nagai proposed a model for electrode void space as a function of current, but does not go deep into detail regarding bubble evolution. Aldas et al. developed a model for bubble formation and show experimental results [3], although the model and experimental results are not really correlated to one another. Mat and Aldas presented a similar approach to Aldas et al.; they argue that determination of flow regimes leading to lesser residence time of bubbles on the electrode is crucial to enhance the performance of the system. Aldas and colleagues [3] and [61] assumed there is slip between gas and liquid, meaning that both phases flow at different velocities, which is not true when the pores are sufficiently small (see [97]). A major challenge of measuring bubble-related voltage losses is the actual visualization of both phases; several authors have used different setups consisting of either acryllic [98][106][107][105] or polycarbonate [89] end plates. A major drawback of such approaches is the infeasibility to operate at high pressures.

Multiphase fluid dynamics is a topic that has been intensively pursued for the last half century; understanding how a two-phase flow affects the flow's transport properties can lead to improvements of design in a wide range of processes, ranging from nuclear reactor engineering [19] to electrochemistry

[43][46]. One of the earliest attempts at including two-phase phenomena in modeling was that of Lockhart and Martinelli [58]: they proposed an empirical correlation to predict pressure drops of two-phase flows based on the pressure drops of the individual phases. Subsequent works aimed at correcting Lockhart and Martinelli's correlation to take into account the flow regime of each phase [18]. Among the earliest works studying two-phase flows, the article of Bretherton is perhaps the most influential [16]; this work is one of the first to develop a model of bubble motion in tubes. The work of Nicklin is also influential in the subject of two-phase flows in tubes; Nicklin predicted originally that a two-phase flow can show a negative pressure drop due to shear stresses on the liquid [67]. This negative pressure drop is caused by a slip between the gas and liquid phases that causes liquid to flow in a direction opposite to the gas stream, causing shear stresses that act opposed to what normally is expected [55]. Some articles report a counter-current flow of liquid and gas in a vertical tube [55][56], confirming the theory by Nicklin. However, in both articles the vertical tube had a diameter between 0.91 and 3 mm [55] and 40 mm [56] and, according to the latter, the negative pressure drop is offset by buoyancy in the gas-phase; therefore, the behavior of two-phase flow in tubes with diamters smaller than 900 µm is still unclear.

Scientists typically use one main graphical representation of how gas and liquid interact namely, the flow regime map. Gas and liquid adopt different flow morphologies, which depend on the relative velocity of each phase: bubbly phase (where gas bubbles are smaller than the flow channel), slug phase (where gas bubbles are larger than the flow channel), churn flow (where bubble slugs break off due to the gas being turbulent), and annular flow (where gas flows as a continuous phase in the middle of the flow channel and liquid flows as a thin film along the walls), see [43]. Ishii published one of the first and most widely used two-phase flow models [42], which was later used to draw a flow-regime map that predicts the flow regime as a function of the individual gas and liquid velocities. Mishima and Hibiki subsequently added corrections to the model by Ishii [64], and later extended further the theory to horizon-

tal channels and concluded that there is a substantial difference between the regime maps for circular and rectangular channels, and that the coalescence of bubbles increases when the channel size is smaller than 4 times the bubble radius [40]. The flow-regime map has been used to calculate the pressure loss in the flow field of a PEM electrolyzer (see [43][24][23]). Further works have continuously improved the understanding of the flow regime map, and how each two-phase flow regime can have different transport properties; see [97][95][81][55][108].

One of the main parameters that affects the multiphase rheology is the surface tension. Lubetkin discusses the Marangoni effect, which is the appearance of forces due to surface tension gradients (thermophoresis, thermocapillary effects) [59]; he also stated that simple gases (H_2, O_2) exhibit surfactant behavior in solution. Fukano and Kariyasaki stated that surface tension has a larger effect on the flow pattern than gravity when the channel diameter is less than 5 mm [29]. Regular two-phase literature and models (such as the ones discussed in the previous paragraph) do not apply to capillaries, where surface tension is predominant and there is a reduction in the slip velocity, making the two-phase flow chacteristics independent of gravity. Bretherton developed a theory stating that a gas that flows into a capillary full of liquid will establish an annular flow [16]; he derived a model to calculate the thickness of the liquid film. Schwartz et al., and Aul and Olbricht further discussed the theory of Bretherton [81][6]. Further literature exists that discuss the subject in more detail (see for example [53][39][21]).

As I mentioned earlier, the appearance of gas bubbles can reduce the efficiency of water electrolyzers; there are several theories that predict the departure diameter of bubbles, useful to predict the efficiency loss of a gas evolving electrode. Oguz et al. concluded, from the Young-Laplace equation, that large bubbles grow due to addition of mass rather than pressure difference [70]; they derived a model to predict detachment radii as a function of pore sizes (see also [13]). Van Helden et al. derived a bubble force balance to predict the detachment radii from vertical surfaces [109]; they argue that the driving force of

detacment is the force balance orthogonal to the surface in a liquid flow field parallel to the gas evolving surface (i.e., lift exerted by the liquid); therefore, liquid drag does not play a role in determining the detachment radii, only in determining the trajectory of the detached bubble. Enríquez et al. stated that a bubble that evolves on an horizontal surface, grows from the pit until buoyancy overcomes the surface tension [25]. Vogt mentioned an intrinsic relationship between gas departure and the shielding of an electrode by the bubble (reactant deprivation of an electrode caued by blockage of the bubble) [99]; the shielding is a function of current density and the surface properties of the electrode. Vogt conducted a litersture survey and discovered that the average bubble diameters across different gas evolving electrodes lies between 50 and 100 µm [99]. Vogt et al. developed a model to explain the mass transport in gas evolving electrodes [101][100][102]. Vogt and colleagues divide the mass transport of a gas evolving electrode in two steps: mass transfer from the active site to the surrounding liquid, and mass transfer from the liquid to a bubble [100]. According to Vogt and Stephan, two main transport processes exist in gas evolving electrodes: non-steady diffusion following bubble departure and convective mass transfer induced by bubble growth [102].

Several publications have asserted the presence of mass transport overpotential in PEM electrolysis and the role of multiphase flows during operation. Ito et al. based their work off the works of Ishii [42], and Mishima and Hibiki [64][40], and measured a flow regime map of a PEM electrolyzer, where they assessed the effect of different flow fields (mono serpentine, multi serpentine and parallel) on the pressure drop [43]. Ito and colleagues suggested a relation between flow velocity and overvoltages, but this overvoltage cannot be solely explained by flow velocity. They show a method to calculate the pressure drop caused by two-phase flow using correlations, based on the work by Lockhart and Martinelli [58]. Ito et al. argue that mass transport overpotentials only appear in the anode (the O_2-evolving electrode) thus water circulation in the cathode does not significantly affect cell operation [43], albeit this is later refuted by a later publication of the same research group [46]. Dedigama et

al. visualized bubbles in a transparent PEM electrolyzer [24], using a similar design to the ones already portrayed in the literature [98][106][107][105]; they observe that the energy consumption of electrolysis increases with increasing electric current and increasing water flow. Ito et al. stated that larger bubbles hinder more the supply of water to the catalyst than small bubbles, that larger pores imply larger bubbles, and that larger pores lead to larger activation overpotentials [45]. Ito and colleagues find a source of overpotential that cannot be explained by either activation or ohmic overpotential; this overpotential scales with pore size [45], and appears analogous to the bubble overpotential measured by Roy and colleagues [77]. Nie and Chen modeled the two-phase laminar flow through the anode of a PEM electrolyzer using a CFD-based model [68]. Ito et al. presented an equation that calculates the critical bubble diameter as a function of buoyancy and surface tension (similar to the one by Bi and Zhao [13]) [44]. Lafmejani et al. derived an equation to estimate the thickness of the water film in a Taylor (slug) flow [47], similar to the previously derived equations by Bretherton [16] and Triplett et al. [97]. Ojong et al. derived the mass transport overpotential equation from the Butler-Volmer equation [71]. Fritz et al. derived a mass transport model, based on the results by Chun et al. [19], to model mass transport losses in PEM electrolyzers [28]; this model takes into account water flow and gas evolution.

The causes of mass transport losses in PEM electrolyzers, as well as the effect of the cell design, have also been discussed in the literature. Aubras et al. stated that the two-phase regime affects ohmic resistance [5]; according to Aubras and colleagues, there are two flow regimes namely, non-coalesced bubbles and coalesced bubbles. Aubras and colleagues proposed the theory that the Nafion™ membrane is not saturated with water at all times but rather that the water in the Nafion™ membrane is in equilibrium with the water in the electrode [5] and that this equilibrium is affected by the presence of gas bubbles. Lee et al. carried out experiments where they simulated the pores in a PTL and conclude that the mass transport through pores is single-phase [49][50], not two-phased as it is commonly hypothesized (see for example [47]). Lee and colleagues

mentioned that the performance of a PTL depends on the throat distribution (thus the openings of the pores) rather than on the pore distribution; the capillary pressure in the throats govern gas movement [50]. Han et al. modeled the two-phase transport in a PEM electrolyzer; they find that the PTL should be as thin as possible, as porous as possible and hydrophilic [38]. Regarding the PTL design in PEM electrolysis, Arbabi et al. created an experimental representation of an operating Ti PTL (similar to the setup of Lee and colleagues [49][50]) and measured air flowing through water-filled pores [4]. Arbabi and colleagues distinguished three main substrates usable as PTL material for PEM electrolysis: Ti felt, sintered Ti and Ti foam, and they conclude that liquid flow does not affect air transport and that Ti felt offers the least flow resistance in an operating PEM electrolysis environment [4]. Arbabi and colleagues observed that the two-phase flow is capillary-dominated: surface tension plays a vital role in two-phase transport [4]. Grigoriev et al. reviewed the effect of the PTL properties on the PEM electrolyzer operation [35]; they hypothesized that large pores are inhabited by gas and small pores are inhabited by liquid; mass transport limitations are found to depend on small pores. According to Grigoriev and colleagues [35], pore size has two effects: large pores are required for good mass transport, small pores are required for good conductivity, and neither the gas permeability nor the porosity affect the performance.

Despite the plethora of available literature on the subject of multiphase flow in PEM electrolyzers and how it affects the mass transport overpotential, there does not seem to be a consensus about how to tackle the subject, contrary to what Carmo et al. mentioned on their review article [17]. A relatively recent review on mass transport in PEM electrolysis argues that very few dedicated mass transport studies are actually available [1]. Measurements carried out by Arbabi and colleagues, and Lee and colleagues, showed the mass transport through pores to be dominated by gas permeation through water-filled pores [4][50]; this idea is contrary to the common assumption that an annular flow is established in the pores of a PTL [28][47], which leads to the mass transport overpotential to be related to bubble sizes [5]. Moreover, little attention

has been put to modeling the mass transport at electrode level, with most of the literature adopting a simpler approach of parametrizing either Fick's law or Darcy–Weisbach's equation (the so-called diffusion-driven and momentum-driven approaches, respectively, mentioned by the review by Carmo et al. [17]) and adapting it to a mass transport overpotential equation derived from the Butler-Volmer equation (e.g. [71]).

Furthermore, several authors have investigated the effect of other operating parameters than temperature or current density (mainly pressure) on the total system overpotential and have reported mixed results; Table 1.1 (top) summarizes the surveyed publications. There does not seem to be a clear consensus regarding the effect of pressure on the performance: 8 out of the 15 surveyed publications found a negative effect of pressure, most of them testing up to 2 A cm^{-2} and between 20 and 100 bar. 5 out of the 18 publications depicted in Table 1.1 found a performance improvement due to pressure (4 of which come from the same research group), operating at current densities higher than 2 A cm^{-2} and at up to 50 bar. Shapiro and colleagues found no discernible trend between pressure and current [85], and Suermann et al. found the performance of their PEM electrolysis stack to be independent from pressure at up to 5 A cm^{-2} and 100 bar [94]. These results indicate that there is no universally dominating effect of pressure on the performance of PEM electrolyzers, and that testing conditions of each experiment (for example cell configuration) seem to play an important role.

There has been considerably less attention paid to the role of water flow on the performance of PEM electrolysis systems; Table 1.1 (bottom) summarizes the findings of the respective literature survey. The only publications that discuss the role of water flow on the mass transport losses are the ones following the modeling approach suggested by Carmo and colleagues [17], in particular the mass transport model by Fritz et al. [28]. Some studies argue that water flow is an operating parameter that affects the mass transport losses [5], either by removing the bubbles and therefore decreasing the mass transport losses [71][46][52], or by increasing the mass transport losses by other mechanisms

[82]. Other researchers, such as Medina and Santarelli, have suggested water flow not to have any effect on performance whatsoever [63]. From the literature surveyed a clear conclusion is that the dependence of the total system overpotential on pressure and water flow is unclear and largely based on testing conditions; therefore, there is much to be yet understood.

Detecting the effect of operating parameters on mass transport losses requires the use of *operando* measuring techniques. Out of the available *operando* tools for measuring and differentiating the different sources of overpotential, electrochemical impedance spectroscopy (EIS) is one of the most useful, given that its use is fairly simple and that there is an extensive theoretical framework that relates the measurements to physical phenomena such as mass transport [48][9]. Despite this, EIS has been rather underutilized in the PEM electrolysis community as a tool to measure mass transport losses, where most of the results are rather qualitative rather than quantitative [86][76][92][78]. Typical uses of EIS include characterizing electrodes in rotating disk electrodes (RDE) tests or to characterize MEAs, although the EIS spectra are rarely analyzed to find the physical significance of the parameters obtained after fitting the data to an equivalent circuit.

1.3 OUTLINE OF THIS THESIS

This work focuses on the multiphase flow phenomena that occur in PEM electrolyzers. Chapter 1 shows the literature survey conducted regarding mass transport, multiphase flows and the role of water flow and pressure on the performance of PEM electrolyzers, and has provided a detailed insight into the problem. Chapter 2 showcases the utilized materials, equipment, and measuring methods throughout this thesis. I divided the work carried out in three further chapters. Chapter 3 focuses on the detection of gas bubbles in an operating PEM electrolyzer; different optical setups were used to photograph different two-phase flows that occur in a PEM electrolyzer (in flow field channels, in a PTL and around electrode) and the results were modeled using the

bubble force balance presented by van Helden and colleagues [109] to validate the measured bubble departure diameters. Chapter 4 depicts the results of different gas permeation measurements carried out in a sintered Ti PTL. The derivation of an energy balance model is shown, which accounts for the pressure drop measured and explains the effect of water flow on the pressure drop of an evolved gas flow. The results show the relationship between the measured gas permeability and the pore characteristics of the sintered Ti using the van Genuchten–Mualem model ([41]). Chapter 5 shows the measurement of mass transport overpotentials in a PEM electrolyzer using EIS; the results are validated with help of a derived model that combines the mass transport model developed by Vogt and colleagues [100][102] with the EIS model for finite-length mass transport [48]. Throughout this work I discuss the literature relevant for each topic, which includes both literature I have discussed in this introduction and more specific literature for each one of the chapters. Chapter 6 rounds off this thesis by presenting the overall conclusions as well as some insights regarding future work.

Pressure				
Authors	Maximum tested pressure / bar	Maximum tested current density / A cm^{-2}	Pressure effect on current density	Reference
Espinosa-López et al.	35	1.4	Negative	[26]
Frensch et al.	34	2.0	Positive	[27]
Grigoriev et al.	25	2.5	Positive	[34]
	25	2.5	Positive	[37]
	50	2.0	Positive	[35]
	8	0.6	Positive	[36]
Li et al.	2	1.5	Negative	[52]
Marangio et al.	70	1.3	Negative	[60]
Olesen et al.	70	1.0	Negative	[72]
Santarelli et al.	70	1.3	Negative	[80]
Selamet et al.	50	1.0	Negative	[82]
Shapiro et al.	14	1.0	Independent	[85]
Smolinka et al.	20	2.0	Negative	[91]
Suermann et al.	100	5.0	Independent	[94]
	100	4.0	Negative	[92]
Water flow				
Authors	Maximum tested water flow / l h^{-1}	Maximum tested current density / A cm^{-2}	Water flow effect on current density	Reference
Dedigama et al.	0.5	0.5	Unclear	[24]
Ito et al.	3.0	1.0	Negative	[43]
Selamet et al.	90	1.0	Negative	[83]

Table 1.1: Surveyed literature that focused or featured studies on the effect of pressure and water flow on the performance of PEM electrolyzers.

2

EXPERIMENTAL SETUP AND METHODS

2.1 CONSTRUCTION OF TESTING STATION

To carry out the required measurements for this work, I designed and constructed a PEM electrolysis testing station. The need for the test station arose from a necessity for automation, which greatly improved the safety of the experiments as well as the repeatibility of each measurement. The design guidelines of the testing station were the following:

- Compatible for 25 cm^2 cells. This is the most common cell size performed at the low temperature fuel cell and electrolysis research group and the Institute of Engineering Thermodynamics of the German Aerospace Center. Nevertheless, the testing station should be flexible enough to handle other cell dimensions.
- Pressurization up to 15 barg. Research at a medium pressure range appears rarely in the literature (pressures are either atmospheric or 100+ bar), which is the focus of this research.
- Temperature handling up to 80°C. Beyond this temperature there are two main problems: the vapor pressure of water is relatively high (thus a large amount of deionized water is lost to evaporation) and the rubber sealing in the electrolysis cell (made of Viton®) starts to weaken, thereby leaking unsafe amounts of H_2 and O_2 to the laboratory.
- Water flows up to 7.5 l h^{-1}. Common water flows reported in the literature are in the range 60-120 l h^{-1} and there are scarce articles that deal with the effect of water flow, especially at near stoichiometric flows; therefore, my research was aimed at covering that flow range.

- Electric current and voltage up to 150 A and 5 V, respectively. This current amounts to 6 A cm^{-2}, which is larger than the maximum typical current densities employed in PEM electrolysis research (typical is 1.5-2 A cm^{-2} for single cells and up to 4 A cm^{-2} for stacks). The operating cell voltages lie between 1.4 and 2.5 V, thus the choice of 5 V is only to safely handle the typical operating voltages. Large electric current and voltage capabilities mean that the testing station can handle cells with a wide variety of active areas, as well as short stacks (2-3 cells).

- Redundant safety features. There are three types of safety features in the testing station: software-activated, hardware-activated, and manually activated. The testing station measures the concentration of H_2 and O_2 and any upward deviations from the safety explosion limit of H_2 (4% in air) automatically trigger the safety protocol that shuts down the electric current from the power supply and pumps water at the pumps' maximum capacity to mitigate any possibility of explosion. The testing station is connected to the N_2 supply line in case a fire needs to be suffocated.

- Controllable by a user-friendly interface. I designed the user interface based on LabVIEW™. The controls are properly labeled and are intuitive.

- Standalone operation. This feature was an innovation among the testing capabilities of the research group: the testing station's control software contains an algorithm that reads the values of all input variables from a table, and can implement them in a user-specificed time period. I also designed a water refilling algorithm that is triggered automatically, whether overnight or during weekends and holidays, thereby allowing continuous operation that can span months at a time.

- Dynamic temperature behavior. The common approach to controlling the temperature of a PEM electrolyzer is to heat up a large reservoir of water, thereby introducing a large thermal inertia to the process. My approach consisted of heating the water pipes that are next to the electrolyzer as

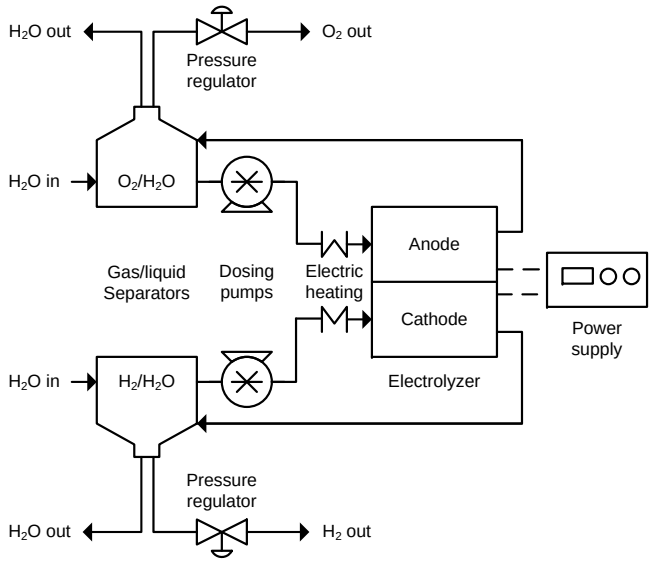

Figure 2.1: Process flow diagram of the testing station.

well as the electrolyzer itself, which allows for starting-up times of 20-30 min; the dissipated heat from the electrolysis reaction helps the fast heating up of the water that enters the PEM electrolyzer.

Figure 2.1 shows the process flow diagram (PFD) of the testing station. The PFD features two main water loops, one for each electrode in the MEA; the main difference between my design and the conventional testing stations is the dedicated cathode water loop. Similarly to carrying out research on the effects of near stoichiometric water flow, I surveyed the existing PEM electrolysis literature and discovered that very little attention was being put on the effect of circulating water through the cathode of a PEM electrolyzer instead of the common practice of flooding the cathode with water. I decided that it was best to circulate water through the cathode side symmetrically to the anode side. Moreover, I wanted to maintain flexibility should I require to make minor modifications of the setup to allow for different types of experiments.

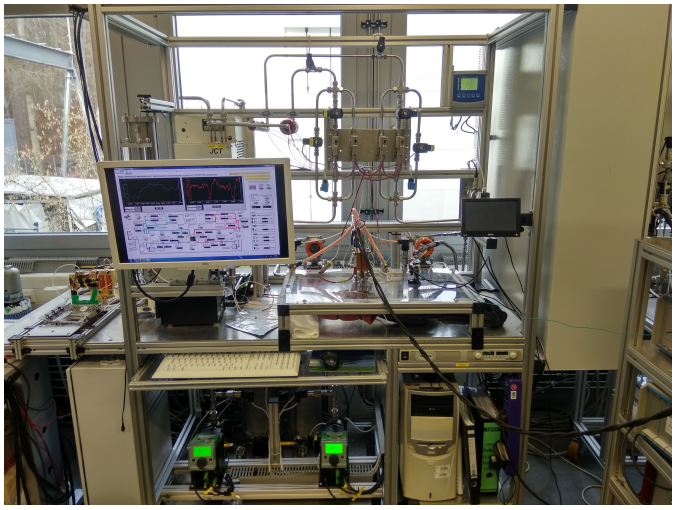

Figure 2.2: Picture of the testing station.

The main components of the water loop are the gas-liquid separator, the dosing pump, the heating, and the back-pressure regulators; Figure 2.2 shows the constructed testing station. The testing station consists of:

- Instrumentation: includes pressure sensors, temperature sensors, water level sensors, flow sensors, concentration sensors, conductivity sensors, a voltage sensor, a current sensor, and differential pressure sensors.
- Actuators: includes solenoid valves and electric heaters.
- Control units: includes back-pressure regulators, dosing pumps, and a controllable power supply.
- Auxiliary and safety equipment: includes relief valves, check valves, ball valves, gas-liquid separators, and gas dryers.

Figure 2.3 shows pictures of some of the components and instruments installed in the testing station.

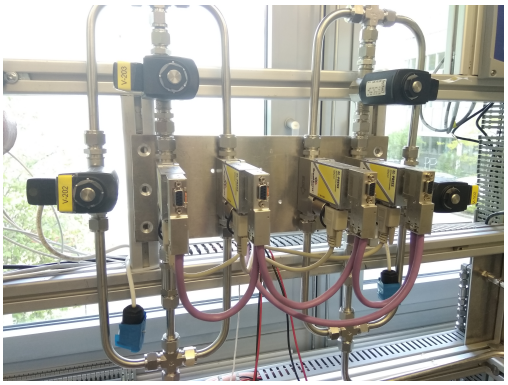

(a) Back-pressure regulator

(b) Dosing pumps

(c) Gas flow meter

(d) Gas dryer

Figure 2.3: Picture of some of the instruments and components of the testing station. The back-pressure regulators and gas flow meters were manufactured by Bronkhorst, the dosing pumps were manufactured by Fink ct, and the gas dryer was manufactured by JCT Analysentechnik.

2.2 MATERIALS USED

The materials I used for testing (except if otherwise stated in the following sections) are the following:

- MEA. Consisted of Nafion™ 115 (electrolyte), 2 mg cm^{-2} Ir-black loading for the anode, and 1.3 mg cm^{-2} Pt/C loading for the cathode. All MEAs used in this work were provided by balticFuelCells and consist of 25 cm^2 MEA; the active area (where the electrodes are deposited) measures 50 x 50 mm while the membrane measured 100 x 100 mm to allow for better gas sealing.
- PTLs. Consisted of sintered Ti (GKN, 50 x 50 x 1 mm, 14 µm average pore size and 40% porosity); I used the same PTL for both sides in the majority of experiments to highlight the mass transport on both electrodes under the same circumstances.
- Flow fields. Consisted of 50 x 1 x 1 mm channels machined into a Ti plate (70 x 50 x 1 mm, 25 channels in parallel).
- Gaskets. Consisted of Viton® and were shaped to fit the perimeter of the PTLs and to account for mechanical expansion caused by compression (52.5 x 1.5 x 1 mm).
- End plates. Consisted of stainless steel (SS316) plates with holes for the water and gas streams where the flow fields are mounted on.

Figure 2.4 shows a picture of the actual testing cell used for the experimental work in this thesis.

2.3 EXPERIMENTAL METHODS USED

2.3.1 *Bubble evolution and detachment*

I tested the MEAs using the testing cell depicted in Figure 2.5; the cell layout is essentially similar to the cell I used for the rest of the experiments (Figure 1.2), save for the use of an end plate with an inlaid sapphire glass window on the anode side instead of a closed end plate. The use of a sapphire glass window ensured optical accessibility to observe the evolved O_2 bubbles. I used three

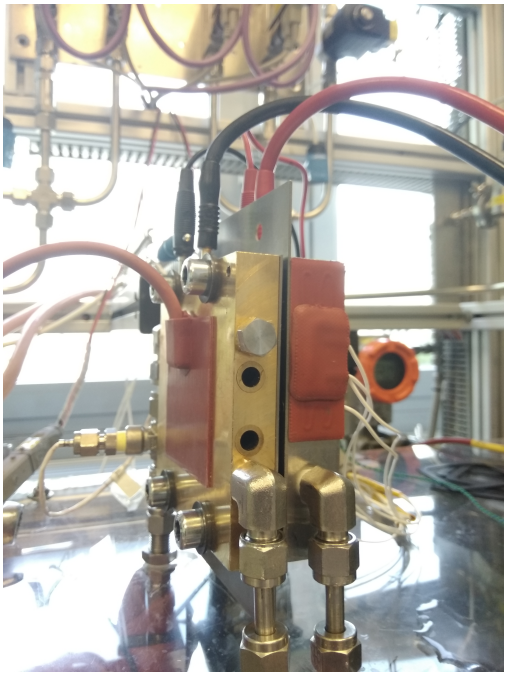

Figure 2.4: Picture of the assembled 25 cm² PEM electrolysis cell where all the tests described in the following sections were carried out. On the image the cell is showcased along with electric heaters attached to the end plates (red patches), and the mechanical and electric connections to the testing station.

different PTLs on the anode side: sintered Ti to capture bubbles flowing in a flow field channel (Figure 3.2), Ti mesh (Sorst Streckmetall, 50 x 50 x 1 mm, 1 x 0.75 mm pattern size) to capture bubbles evolving on macro pores (Figures 3.3 and 3.4), and a Ti mesh coated using Vacuum Plasma Spraying (VPS) (in-house made, Ti coating, 50 x 50 x 1 mm, 0.75 x 0.3 mm pattern size) to observe bubbles evolving directly on top of the electrode (Figure 3.6). I used a slightly modified testing setup (Figure 2.6), which is essentially similar to the one depicted in Figure 2.1 with the addition of a stand for the cameras and the illumination.

The camera setup consisted of a camera and LED illumination; I used different cameras and LED lamps to take the different kinds of images, capturing the different stages of bubble evolution (detachment and motion) with more precision. For the pictures of bubbles in a flow field (Figure 3.2), I used a Hero4

Black camera (GoPro) with a removed low-pass filter. I fitted the GoPro camera with a macro lens filter (Polar Pro) and I illuminated the cell using 720 nm LEDs (Roithner Lasertechnik). I chose the 720 nm wavelength to be able to differentiate O_2 from water: at this wavelength, O_2 partialy absorbs the IR radiation while water fully transmits it. The images displayed in Figure 3.2 are actually frames of a 240 fps video.

For the images with the Ti mesh (Figure 3.3), I used a D7200 camera (Nikon) without low-pass filter, fitted with an AF-S VR Micro-Nikkor macro lens (Nikon); I used the same 720 nm LEDs to distinguish O_2 from water. The rest of the images (close-up of the Ti mesh, Figure 3.4 and close-up of the VPS-modified Ti mesh, Figure 3.6) were taken with the same D7200 camera, fitted instead with a QM 100 long-distance microscopic lens (Questar) and cool-white LEDs. Whereas the images in Figures 3.3 and 3.4 were images taken with a shutter speed of 1/2000 s, Figure 3.6 displays frames from a video shot at 30 fps.

I tested the effect of the water flow on the bubble detachment sizes on all tests; for this purpose I used two different pumps. I used a gear pump (ISMATEC) to finely control the water flow on the anode side (the water flow I used was between 0.07 and 4.65 l h^{-1}); additionally, I used a diaphragm pump (Fink ct, Figure 2.3, top right) to record the images with the flow field (Figure 2.5, top). To promote gas evolution, I applied a current to the cell; given the poor through-plane conductivity of the Ti-mesh (even after VPS coating) and the poor in-plane conductivity of the Ir-black, the current density I applied on all tests except the ones with a flow field and sintered Ti as PTL (Figure 3.2, top) was 0.04 A cm^{-2}. I used a current density of 1 A cm^{-2} for the tests with flow field and sintered Ti. The cell temperature at all times was 65°C.

Along with qualitative analysis of the bubble evolution, detachment and motion inside a PEM electrolysis cell, I carried out quantitative tests namely, the detection, measuring and counting of the evolved bubbles. I was primarily interested in the effect of water flow on the bubble detachment radius; therefore, I detected the bubbles only on the microscope images of the Ti mesh (Figure 3.4). To detect the bubbles, I wrote a MATLAB script based on the Image

Processing Toolbox (MathWorks). The script consisted of the following steps: converting the image to grayscale, thresholding the dark areas, binarizing the image, removing small pixels, closing large pixel clusters, and measuring the pixel clusters that show the highest contrast with the background. To remove digitally the Ti mesh from the images with a Ti mesh and the macro lens (Figure 3.3, right), I wrote another MATLAB script that performs image registration with a picture where there are no visible bubbles.

2.3.2 *Gas permeation through porous transport layers*

For these tests, I did not use an MEA but rather I tested only the sintered Ti PTLs on a modified setup where gas and water were allowed to cross over freely; the testing cell I used is depicted in Figure 2.7.

In Figure 2.7 there are two end plates, and each end plate has two flow connections: one inlet and one outlet. I carried out two kinds of tests namely, water permeation tests (to measure the water permeation of the tested PTL) and gas permeation tests. During the water permeation tests, I sealed off the outlet of one end plate and the inlet of the second plate (see Figure 2.8, top), thereby forcing water to flow through the PTL. During the gas permeation tests, I left open both flow connectors on one end plate and only the inlet of the second end plate. I bubbled gas through the end plate with the sealed exit, while water flowed through the end plate that had both flow connectors open (see Figure 2.8, bottom); the gas flow was forced to flow through the PTL, which in turn had water flowing through one of its sides, causing the PTL pores to saturate with water. The gas and water streams were collected in a gas-liquid separator, where the water was recirculated and the gases were dried (stripped from any humidity) using the gas dryer (Figure 2.3, bottom right). I measured the pressures P_1, P_2, and P_3 (Figure 2.8) using digital pressure sensors (Siemens) and the gas flows using thermal conductivity flow sensors (Figure 2.3, bottom left); I controlled the gas pressure drop using the back-pressure regulators (Figure 2.3, top left).

I used two different gases for the gas permeation tests: H_2 and N_2, which are representative of the gases produced in a PEM electrolyzer. I chose to work with N_2 instead of O_2 due to safety concerns regarding handling dry, pure O_2 in equipment that also handles dry H_2. Nevertheless, the results obtain with N_2 can be representative of the results that would be obtained with O_2 due to the similar physical and transport properties of both gases. For each gas, I carried out a test consisting of three experimental runs (to calculate the error bars of all tests); each experimental run consisted of increasing the water flow rate between 1 and 6 l h^{-1} and recording the flow rates and pressures in the system. Each set point was kept for periods of 1 h; therefore, each experimental run lasted 6 h, and a full test of a single gas lasted 18 h. I logged the measurements every 5 s; the data presented is the average of 720 data points.

2.3.3 *Impedance spectroscopy of mass transport phenomena*

I tested the MEAs using the unmodified testing cell (Figure 1.2); the tested MEAs were manufactured in different batches. The PTLs with an average pore size of 14 µm were chosen because a previous study on sintered PTLs for PEM electrolysis concluded that 14 µm is the optimal pore size for PTLs [35]; therefore, I did not expect the PTL to have a significant role in the mass transport losses as compared with the porous electrodes. Common practice involves using Sigracet layers (porous carbon paper) on the H_2 side since there is no chemical restriction to use carbon on the low voltage side; I wanted to capture the effect of the operating parameters (pressure and water flow) on both sides under similar circumstances, hence I used the exact same PTL for both sides.

I designed a simple testing protocol that each MEA would undergo; each protocol consisted of the linear variation of either water flow (between 1 and 6 l h^{-1}) or pressure (between 1 and 6 bar), in unitary steps, while the other parameter was set to either 1 l h^{-1} or 1 bar. A total of four testing protocols were measured (anode water flow change, cathode water flow change, anode

pressure change and cathode pressure change). The temperature of the system was kept at all times at 65°C.

During each testing protocol, I measured both a galvanostatic V(I) curve and an impedance spectrum; the V(I) curve was measured between 0.004 and 1.5 A cm^{-2}, using a current ramp of 0.63 A s^{-1}, while the impedance spectrum was measured at 1.5 A cm^{-2}, using a frequency range of 10 mHz-10 kHz. I measured both the V(I) curve and the impedance spectrum on each unitary change of either water flow or pressure, resulting in a total of 6 impedance spectra and V(I) curves per testing protocol (that varied a single operating condition) with a total of 24 different measurements for all four varied operating conditions. Both measurements were carried out using an EIS potentiostat (Zahner–Elektrik). I carried ou each testing protocol a total of three times, each time using a different MEA to account for manufacture variations; all data showcased are the average values of three different measurements.

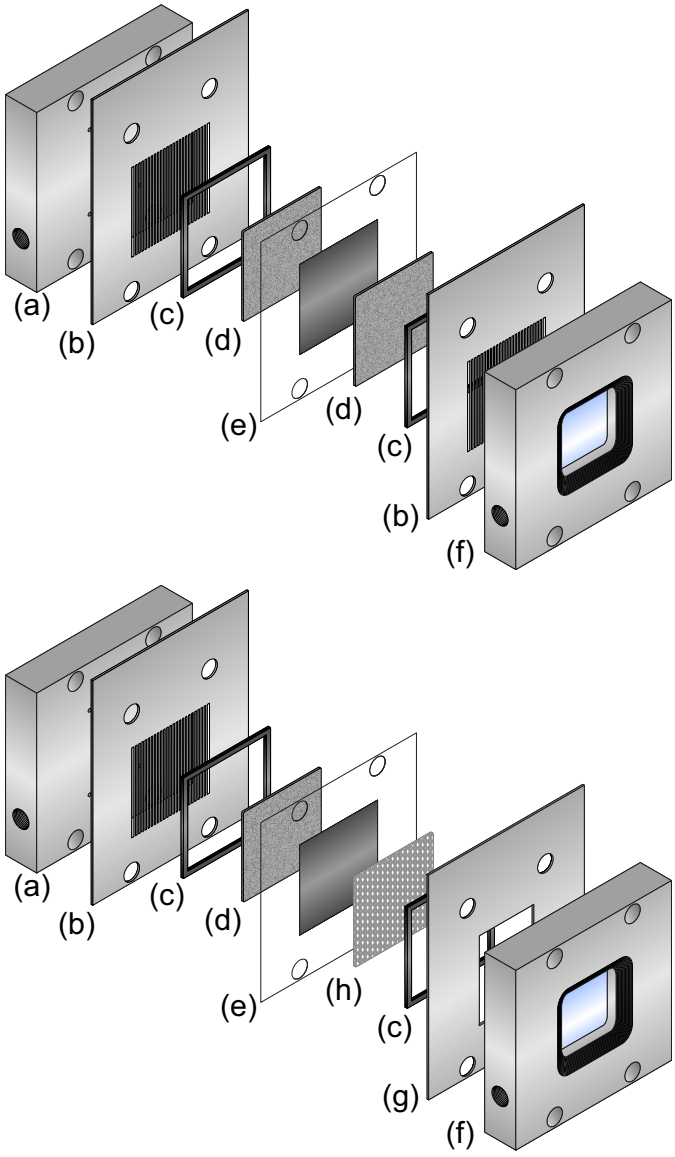

Figure 2.5: (Top) Exploded cell view of the assembled MEA with anode flow field. a) Stainless steel (SS316) cathode end plate, b) Ti parallel flow fields, c) Viton® gaskets, d) sintered Ti PTLs, e) MEA, f) SS316 anode end plate with sapphire glass window. (Bottom) Exploded cell view of the assembled MEA with no anode flow field. a) Stainless steel (SS316) cathode end plate, b) cathode Ti parallel flow field, c) Viton® gaskets, d) cathode sintered Ti PTL, e) MEA, f) stainless steel (SS316) anode end plate with sapphire glass window, g) anode Ti plate with window, h) anode Ti mesh for electrode visualization.

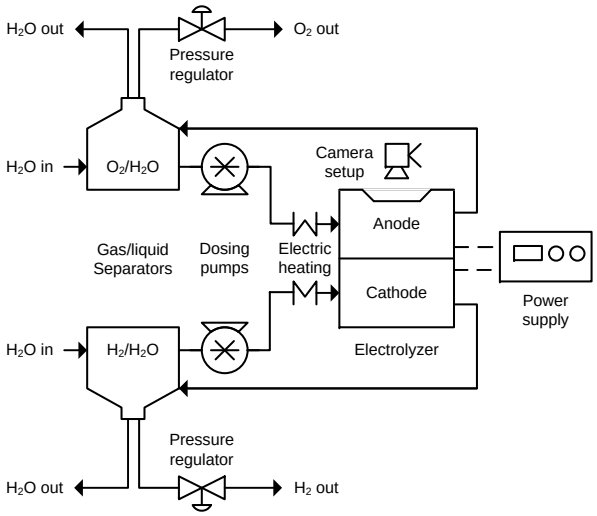

Figure 2.6: Process flow diagram of the slightly modified testing station where the bubble evolution was visualized.

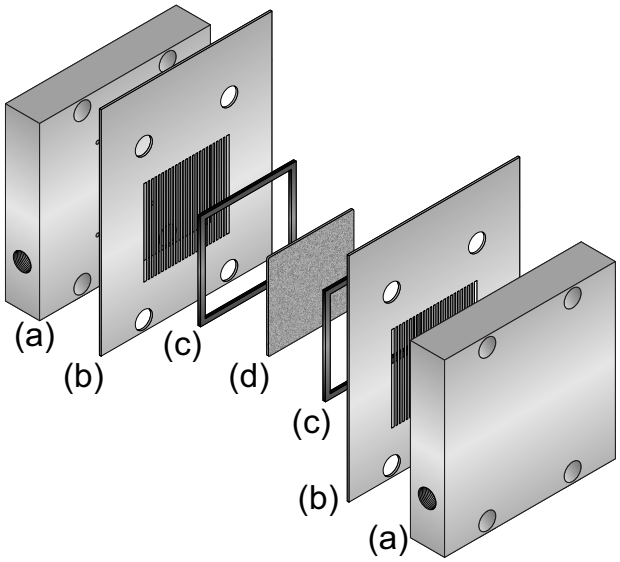

Figure 2.7: Exploded cell view of the cell where the permeation tests were carried out. (a) SS316 end plates, (b) Ti flow fields, (c) Viton® gaskets, and (d) sintered Ti filter.

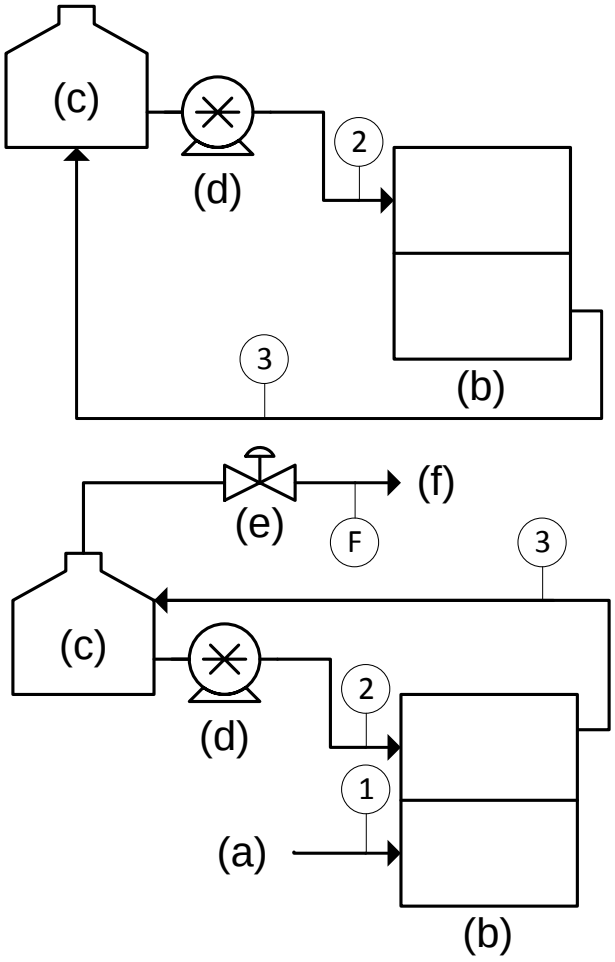

Figure 2.8: (Top) Process flow diagram of the water permeation experiments. (Bottom) Process flow digram of the gas permeation tests. In both images (a) gas inlet, (b) test cell (see Figure 2.7), (c) gas–liquid separator, (d) dosing pump, (e) back-pressure regulator, and (f) gas outlet. Circles labeled as 1, 2, and 3 represent the measurement points for the homologous pressures (P_1, P_2, and P_3). Circle labeled as F represents the measurement point for the gas flow (water flow was a set point in the dosing pump).

Part II

RESULTS AND DISCUSSION

Experimental results, mathematical modeling and discussion of the tests; each chapter contains a specific introduction and a conclusion.

3

BUBBLE EVOLUTION AND DETACHMENT

3.1 INTRODUCTION

An important phenomenon related to the multiphase flow dynamics is how the bubble departure size on gas evolving electrodes is determined. The typical measured diameters of detached bubbles have been reported to be between 50 and 100 µm [99][54] and as high as 300 µm [46]. The effect of two-phase flows and bubble evolution on the efficiency of PEM electrolyzers has been widely studied, albeit there does not seem to be a clear understanding of how two-phase flows behave under the operating conditions of PEM electrolyzers, nor up to what extent the size of bubbles affects the mass transport overpotential. Some works propose the existence of a two-phase flow inside the porous transport layer (PTL) pores [69]; other works propose optimal PTL pore sizes [84][45][65] without diving into details regarding rheology inside porous substrates. Some articles have been devoted to studying the effect of material properties and operating conditions on bubble detachment (see [59][62]), while others have visualized gas motion through PTLs and concluded that gas flows as a single phase through capillary pores [4][49]. The experimental work depicted in this chapter is aimed at contributing to the discussion of how gas and water interact in PEM electrolyzers, both on the electrode sufaces and within the pores of a PTL. I combined imaging, image processing and a mathematical model based on a bubble force balance to predict the bubble departure sizes at the anode and how they are affected by water flow; the results presented here lead to design considerations for both the electrode and the PTL.

3.2 MODELING

3.2.1 *Bubble force balance*

I modeled the bubble detachment radii using the bubble force balance model proposed by van Helden et al. [109]. The first assumption is that the evolved gas nucleates into bubbles on the pores of the electrode surface. It is likely that the pores where bubbles grow are spots with a local surface tension maximum, where bubble growth is more energetically favorable than contact between water and solid. On these pores the evolving bubble experiences two kinds of forces: forces acting parallel to the direction of water flow, and forces orthogonal to the electrode surface. Bubble detachment occurs when the forces normal to the electrode are at equilibrium; thus, a minor disturbance or a force acting on a different direction can cause the bubble to experience an acceleration and therefore get displaced.

The surface tension force (F_σ) acts against detachment of the bubble; it is equal to

$$F_\sigma = 2\pi R_p \left[-C_\sigma \sigma \sin\left(\beta\right)\right] \tag{3.1}$$

where R_p represents the pore radius, σ is the surface tension, and β is the contact angle between the water and electrode. The coefficient C_σ in equation 3.1 takes into account that β is not constant but rather varies along the pore throat, and this relationship is not linear [109].

The corrected buoyancy force on the x-direction, also named volume force (F_{Bx}) is a combination of two forces: gravity on the surrounding water, which acts against detachment (in the x-axis), and the Young-Laplace force, which acts in favor of bubble detachment. The corrected buoyancy force is displayed in equation 3.2

$$F_{Bx} = \pi R_p^2 \left[\left(\rho_g - \rho_w\right) g R_b + \frac{2\sigma}{R_b}\right] \tag{3.2}$$

where ρ_g and ρ_w are the gas and water densities, respectively, g is the terrestrial gravity acceleration, and R_b is the bubble radius at the moment of detachment.

There are two lift forces caused by a stream of water flowing parallel to the electrode surface: one lift force (F_{L1}) caused by the suction of a uniform flow (water) on an adhering body (bubble), and a second lift force (F_{L2}) caused by the vorticity of the water stream near the wall of the bubble. Both lift force equations are expressed as

$$F_{L1} = \pi R_b^2 \left[\frac{1}{2} C_{L1} \rho_w V_w^2\right] \tag{3.3}$$

$$F_{L2} = \frac{4}{3} \pi R_b^3 \left[C_{L2} \rho_w V_w dV_w\right] \tag{3.4}$$

where V_w is the water velocity (along the y-axis). Coefficients C_{L1} and C_{L2} contain the dependence of the force on parameters such as the shape of the bubble and the flow regime of water.

The bubble will grow until it reaches a detachment radius, which will cause the aforementioned forces to reach an equilibrium, calculated as

$$\exists\, R_b \mid F_\sigma + F_{Bx} + F_{L1} + F_{L2} = 0 \tag{3.5}$$

Any disturbance to the bubble (after detachment) in the y-direction will determine its detachment angle. There are two main forces that will determine the bubble detachment angle: the buoyancy (F_{By}) and the drag (F_D) forces, caused by the incoming water flow; both forces are illustrated in equations 3.6 and 3.7

$$F_{By} = \frac{4}{3} \pi R_b^3 \left[\left(\rho_w - \rho_g\right) g\right] \tag{3.6}$$

$$F_D = \pi R_b^2 \left[\frac{1}{2} C_D \rho_w V_w^2\right] \tag{3.7}$$

where C_D is the drag coefficient of the bubble.

I define the detachment angle as a function of the forces acting on the y-direction (F_y) and the forces acting on the x-direction (F_x) minus the surface tension force. The reason for not including the surface tension in calculating F_x

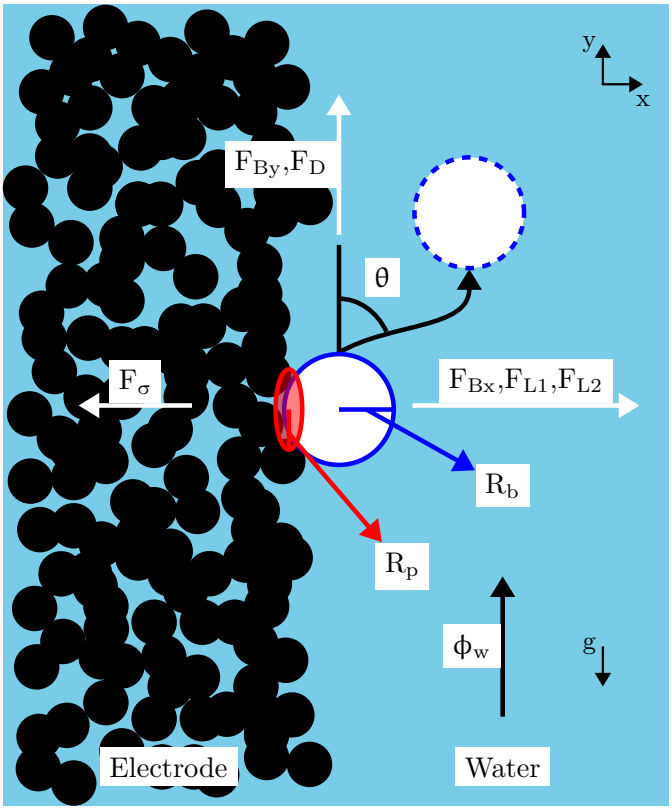

Figure 3.1: Visual representation of the bubble force balance. (White arrows) Forces acting on the bubble. (Black arrows) Trajectory of the water flow (bottom) and the detaching bubble (middle). (Blue circles) Bubble evolving (solid) and detached (dashed). (Red ellipse) Pore on whose throat the bubble evolves.

is that, after detachment, the surface tension force no longer acts on the bubble. The bubble detachment angle (θ) is therefore defined as (see Figure 3.1)

$$\begin{aligned} \theta &= \operatorname{atan}\left(\frac{F_y}{F_x}\right) \\ &= \operatorname{atan}\left(\frac{F_{By} + F_D}{F_{L1} + F_{L2}}\right) \end{aligned} \tag{3.8}$$

A diagram illustrating the model is shown in Figure 3.1.

To calculate the water velocity and acceleration (the latter is needed to calculate F_{L2}), I incorporated the flow regime (laminar or turbulent) into the model.

The velocity and acceleration profiles of water flowing in the laminar regime, as a function of bubble radius (in a rectangular channel), are expressed as

$$V_w = 6V_{w,mean}\left(\frac{R_b}{L} - \frac{R_b^2}{L^2}\right) \tag{3.9}$$

$$\frac{dV_w}{dR_b} = 6V_{w,mean}\left(\frac{1}{L} - \frac{2R_b}{L^2}\right) \tag{3.10}$$

where $V_{w,mean}$ is the mean water velocity and L is the channel thickness. I derived the velocity and acceleration profiles of water in a turbulent regime (in a rectangular channel) using the 1/7-power expression [14] (equations 3.11 and 3.12)

$$V_w = 1.322V_{w,mean}\left(\frac{R_b}{L} - \frac{R_b^2}{L^2}\right)^{1/7} \tag{3.11}$$

$$dV_w = 1.322V_{w,mean}\left\{\frac{L - 2R_b}{7L^2\left[\frac{R_b(L-R_b)}{L^2}\right]^{6/7}}\right\} \tag{3.12}$$

I set the threshold between the laminar and turbulent regimes at $Re = 2100$. The hydraulic diameter of a rectangular channel (D_h) and the threshold water velocity ($V_{w,mean,lim}$) between laminar and turbulent flows are defined as

$$D_h = \frac{4LB}{2\,(L + B)} \tag{3.13}$$

$$V_{w,mean,lim} = 2100\frac{\mu_w}{\rho_w D_h} \tag{3.14}$$

where B is the width of the flow field channels and μ_w is the water viscosity.

I simulated the effect of the number of channels on the bubble force balance (see Figures 3.7 and 3.8). The width of the flow field channels is a function of the number of channels, n_{chan}; the relationship is shown in equation 3.15

$$B = \frac{0.05}{2n_{chan} - 1} \tag{3.15}$$

The value 0.05 m represents the width of the used MEAs, which is the same width as the PTLs, flow fields and end plates (see Figure 2.5). I calculated the mean water velocity, $V_{w,mean}$, as a function of the water flow according to

$$V_{w,mean} = \frac{\phi_w}{LB} \tag{3.16}$$

where ϕ_w is the water flow.

3.2.2 *Sensitivity analysis*

The bubble force balance is a rather simple model with only a few coefficients that need to be adjusted namely, C_σ, C_{L1}, C_{L2}, and C_D. According to van Helden and colleagues [109], $C\sigma$ is a coefficient that accounts for the nonlinearity of the contact angle along the perimeter of the pore; from their simulation results they obtained a value of $C\sigma = 0.6$. Moreover, van Helden et al. derived the value of $C_{L1} = 11/8 = 1.38$ and found that both lift forces, F_{L1} and F_{L2}, are correlated (after all, they are both forces exerted by the same fluid, the only difference being the flow geometry) [109]. Using the C_{L1} value of 11/8, van Helden and colleagues obtained $C_{L2} = 0.1$. I analyzed the effects of both C_{L1} and C_{L2} on the bubble force balance using a second set of parameters obtained by van Helden et al. [109] (1.83 and 0 for C_{L1} and C_{L2}, respectively). Finally, I used a drag coefficient (C_D) of 1.22 that was derived by AlHayes and Winterton [2], which corresponds to a drag coefficient of a bubble at low Re values ($20 < Re < 400$). I tested the effect of using a drag coefficient (C_D) of 0.47, which corresponds to the drag coefficient of a sphere inside a flow with $Re = 10^4$.

Table 3.1 shows the parameters that I used for modeling the bubble force balance, including the parameters that were used for the sensitivity analysis.

Parameter		Value	Unit
General parameters			
T		65	°C
L		1	mm
ρ_g		1.09	kg m^{-3}
ρ_w		1000	kg m^{-3}
μ_w		0.00043	Pa s
σ		0.0626	N m^{-1}
β		76	°
Simulation parameters			
ϕ_w	$\phi_{w,min}$	0	l h^{-1}
	$\phi_{w,max}$	90	l h^{-1}
Force coefficients			
	Reference	Sensitivity analysis	
C_σ	0.6	1	-
C_{L1}	1.38	1.83	-
C_{L2}	0.1	0	-
C_D	1.22	0.47	-

Table 3.1: Parameters used for the bubble force balance.

3.3 RESULTS AND DISCUSSION

3.3.1 *Bubble motion through the flow field*

Figure 3.2 shows the motion of a stream of O_2 and water within a parallel flow field (see Figure 2.5, top). I recorded the images operating at 1 A cm^{-2} and 1 l h^{-1}. Gas bubbles appear darker than their surroundings due to the type of illumination used; at 720 nm, O_2 partially absorbs the incoming radiation, while water transmits it completely. The original photographs were predominantly red; what is depicted in Figure 3.2 are the photographs after stripping

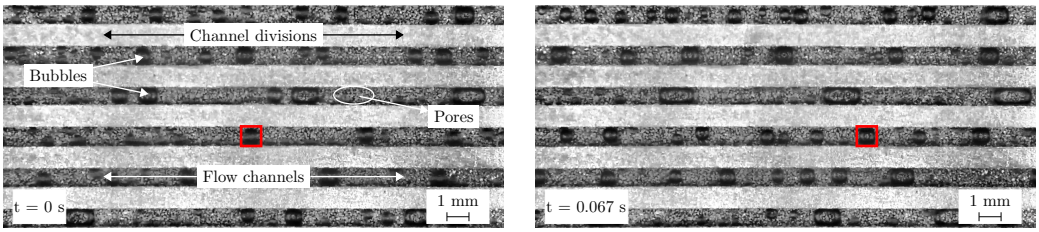

(a) Bubbles flow continuously.

(b) Bubbles stop and the larger ones flow slightly backwards, caused by the suction step of the reciprocating pump.

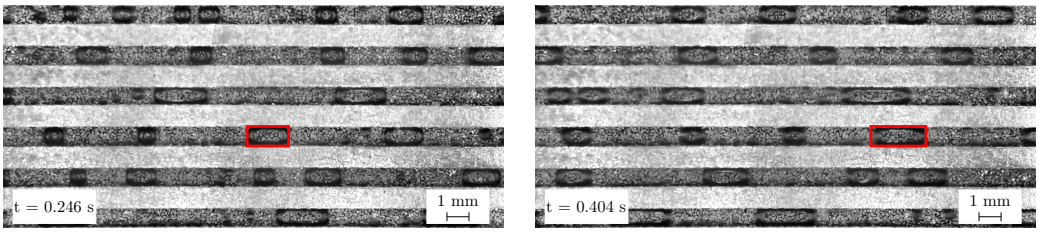

(c) Smaller bubbles with high inertia coalesce with the larger ones, producing bubble slugs.

(d) Bubbles resume the flow as slugs.

Figure 3.2: Photographs showing the motion, coalescence and flow regime change of bubbles in the flow field during operation; one bubble (red rectangle) was highlighted as reference.

the green and blue components from them and performing a histogram adaptation. The brightest objects depicted are the strips of the metal plate that make up the flow field (see Figure 2.5, top). The flow field channels appear slightly darker due to the PTL that stands behind the flowing gas and liquid; randomly intercalated pores and solid Ti yield an overall dark gray color.

In Figure 3.2, I depict a cycle that lasts approximately 0.5 s (induced by the operation of the water pump), where we observe a stream of bubbles that are smaller than the channel width (characteristic of a bubbly flow, see [43][64]); this flow is transitioning to slug flow, characterized by a flow of bubbles larger than the channel width. The cycle of images in Figure 3.2 follows the operating cycle of the diaphragm (positive displacement) pump. At t=0 s, bubbles are in motion following the pump discharge. At t=0.067 s, the larger bubbles stop after the discharge ends, while the smaller bubbles continue their motion with

their remaining inertia. At t=0.246 s, we observe that the smaller bubbles have coalesced with the larger bubbles (creating slugs), following the suction at the pump. At t=0.404 s, the diaphragm pump discharges liquid and the bubbles resume their motion, restarting the cycle.

The two-phase flow inside the flow field has an effect on the overall pressure drop, which will consequently reduce the efficiency of a PEM electrolysis system (including the balance of plant, BOP, components), although this pressure drop is not as significant as it would be if I had used a mono-serpentine flow field [43]. There are two main sources of pressure loss: wall friction between the fluid phases and the channel walls and slip i.e., interfacial friction between the fluid phases [67]. According to the Lockhart–Martinelli [58] model and the subsequent Chisholm–Laird correction [18], the two-phase pressure loss is a function of the ratio between the gas and the liquid fractions [43]. The total pressure loss will therefore be a function of the two-phase flow regime and the pressure drop of the liquid phase. A bubbly flow regime might therefore be recommended to minimize the total pressure loss (due to minimal friction between gas and liquid), although to reach this flow regime at current densities above 1 A cm^{-2} either wider flow field channels or a high water flow is needed, causing the wall friction to increase. Ito and colleagues calculated that the two-phase pressure loss heavily depends on the channel length [43]; therefore, it is advisable to minimize the residence time of the evolved gas within the flow field.

An effective way to minimize the total pressure loss may consist of operating a PEM electrolysis stack with a minimal amount of water. Operation with an annular flow regime (where gas bubbles span the entire channel, relegating liquid to flow only near the channel walls) can maximize the slip between gas and liquid while minimizing the wall friction. Metal is undoubtedly coarser than water; therefore, a gas stream that is in contact with water will experience a reduced friction compared with flowing directly next to a metallic channel wall. Combining this with the fact that water is 10^3 times denser than gas, leads to an effective minimization of the total pressure loss in an annular flow regime.

The stoichiometric water flow required to sustain electrolysis at 1 A cm^{-2} in a MEA with an electrode surface of 25 cm^2 is 8 ml h^{-1}. Considering a stoichiometric electro-osmotic drag coefficient of 5 [43][63], the total stoichiometric water flow required is 48 ml h^{-1}. Other factors to take into account for selecting an optimal water flow include the flow field and PTL design as well as the stack design.

3.3.2 *Bubble evolution on the electrode*

Figure 3.3 shows bubbles evolving on the anode of a PEM electrolyzer; to record these images, I used a macro lens on a modified conventional camera. Figure 3.3 (left) shows the original image that was originally red due to using 720 nm LEDs for illumination, with histogram adaptation and stripping of the green and blue components. I used the Ti mesh to keep the MEA straightened; otherwise, it would crumple when it becomes wet. The main component of the image is the Ti mesh, which reflects light so intensely that it makes it difficult to distinguish the evolving bubbles. To solve this problem, I took another photograph of the MEA with the Ti mesh and no bubbles, and then I performed an intensity-based image registration with both images (with and without bubbles) to produce the image shown in Figure 3.3 (right).

There are two distinguishable types of bubble depicted in Figure 3.3 (right): small bubbles that detached (with a radius of approximately 30 µm), most likely removed by the force of water acting on them, and bubbles that could not be removed but rather coalesced with neighboring bubbles and eventually end up blocking the crevices of the PTL. We can observe a significant amount of bubbles that are large enough to block their respective crevices; thus, it may be more energetically favorable for a bubble to nest in a PTL pore until it is large enough to detach. This observation is consistent with those of Lee and colleagues, who photographed gas flowing through a PTL and determined that gas actually forms a front that pushes water from the pores of a hydrophilic PTL [49][50]. The common understanding of how two-phase flows occur in

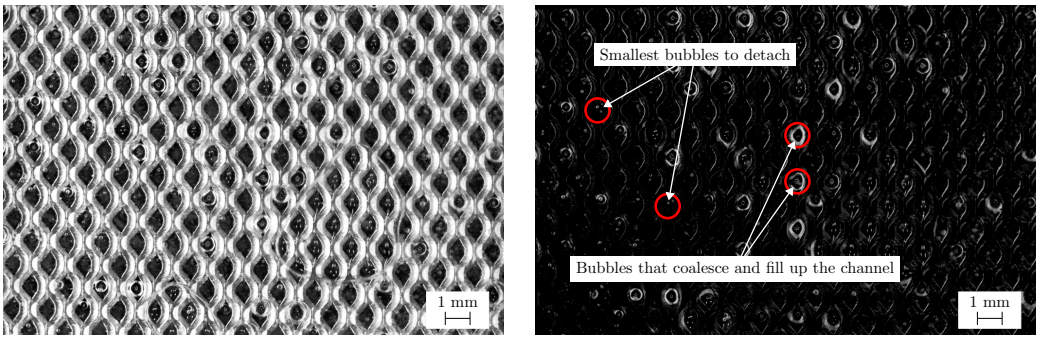

(a) Raw image.

(b) Image after digitally removing the Ti mesh using MATLAB.

Figure 3.3: Photographs of the anode of a PEM electrolyzer, without flow field, and using a Ti mesh rather than the sintered Ti PTL; the photographs were taken using the macro lens. The current density was 0.004 A cm^{-2}, and the water flow was 0.04 l h^{-1}. The images show two types of bubbles (red circles): small bubbles that detach after reaching their critical detachment radius, and bubbles that coalesce with other bubbles and fill up the gaps in the mesh. In both images, water is flowing upward, entering from the bottom of the image.

PTL pores is that an annular flow is established, with gas flowing outwards from the electrode and water flowing in counter-current [69]. Theoretically, it is possible to observe such a flow [67], although I suspect that the pore sizes where such a flow can be encountered need to be much larger for the wall friction to be negative (a pore with a diameter larger than 3 mm can probably experience counter-flowing fluid phases, see [55][56]).

Understanding how gas evolves on the electrode is crucial for the optimization of both PTL and electrode fabrication. To maximize the gas evolution efficiency, the gas bubbles should be as small as possible to minimize "bubble shading" i.e., bubbles that prevent any mass transfer between the active sites and the surrounding water [100][102]. To promote small bubbles, we need to prevent the coalescence and nesting of bubbles on the electrode needs to be prevented, and this does not occur using a Ti mesh. Figure 3.3 shows why meshes are not ideal for use as PTLs despite their cost effectiveness. Another issue to consider is the amount of gas that dissolves in water; according to Vogt and

Stephan, the practical efficiency of a gas-evolving system lies in the percentage of gases that exit an electrolyzer in the gas phase, since gases that exit dissolved in water require an extra energy expenditure to be released [101][102]. Vogt and colleagues propose an empirical relationship between the gas evolution efficiency (f_g, defined as fraction of the total gas flow that exits the cell in the gas phase) and the electrode coverage (θ_{elec}) [102][101]

$$f_g = 0.55\theta_{elec}^{0.1} + 0.45\theta_{elec}^{8} \tag{3.17}$$

$$\theta_{elec} = 0.023 \left(\frac{j}{Am^{-2}} \right)^{0.3} \tag{3.18}$$

where j is the electric current density.

According to equation 3.18, the gas evolution efficiency will be approximately 50% for current densities between 1 and 4 A cm^{-2}, meaning that an electrolysis system needs to recover 50% of the evolved gas that leaves in solution (which would also depend on the water flow, as was mentioned previously). I believe that equations 3.17 and 3.18 are a strong function of the electrode properties (hydrophobicity, particle size), of the PTL (pore size, hydrophobicity) and of the operating conditions (water flow, temperature). Nevertheless, I can conclude that the design of a PEM electrolysis anode and a PTL needs to respond to a need for increasing the gas evolution efficiency as well as a minimal bubble shading of the electrode, and images such as Figure 3.3 can serve as starting points for the design of newly developed materials and operation strategies.

3.3.3 *Bubble detection and counting*

Figure 3.4 shows images similar to Figure 3.3, with the only differences being that I used a microscopic lens to take pictures of an area of approximately 1.6 x 0.9 mm and that I used a regular cool white LED illumination system rather than the 720 nm infrared illumination that I used for Figures 3.2 and 3.3. I used white lighting simply because it was brighter than the in-house-made infrared

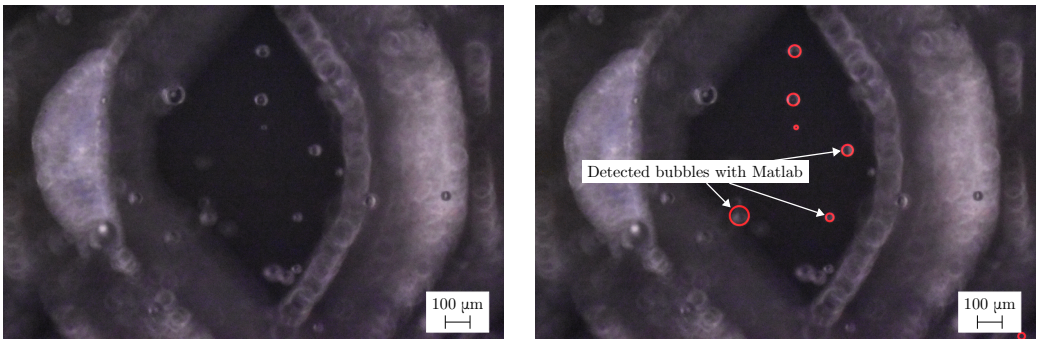

(a) Raw image.

(b) Representative image after bubble detection using MATLAB.

Figure 3.4: Photographs taken under the same conditions as Figure 3.3 using the microscopic lens rather than the macro lens. The detected bubbles (red circles) were automatically pinpointed by the detection algorithm.

illumination system. Figure 3.4 (left) shows a raw image obtained directly from the camera; I processed these images in MATLAB to detect the bubbles that are floating directly in front of the electrode (shown as the black surface on the background). The bubble detection algorithm that I used consisted basically of highlighting the small pixel clusters that show a high contrast with the neighboring areas; therefore, the algorithm did not detect bubbles in front of the metallic Ti mesh. Additionally, the bubble detection algorithm did produce some false positives, particularly at the borders of the image where the shaded areas show a contrast difference similar to the electrode.

Figure 3.4 (right) shows an image after being processed with the bubble detection algorithm. We can observe that not all bubbles in front of the electrode were detected and that there is a false positive in the lower right corner. I fine-tuned the bubble detection algorithm to ensure that most of the detected bubbles were actually bubbles rather than maximizing the amount of detections, for which there can be many false positives. The main difference between Figures 3.3 and 3.4 is that I do not show a coalesced bubble that blocks the crevice of the Ti mesh; rather, the only bubbles shown are the ones that are freely floating, which I assumed would be the smallest bubbles to detach. I did observe, during the course of the experiments that the photographed crevice became

from time to time blocked by a coalescing bubble; I simply waited for the large bubble to detach before continuing the photographing.

I photographed a total of 2956 images of the same crevice and the same current density as Figure 3.4; the only parameter that I varied was the water flow, between 0.07 and 4.65 l h^{-1}. I performed the test using a gear pump instead of a diaphragm pump to have a continuous water flow, thus avoiding the suction-discharge cycles (which have been discussed previously). The detected bubble detachment radii as a function of water flow are plotted on a boxplot diagram (Figure 3.5). We can observe that the median bubble detachment radius in Figure 3.5 does not display a trend but is rather a constant value. This result is at a first glance counter-intuitive since my initial hypothesis was that a higher water flow should yield smaller bubbles due to the drag force water would exert on the bubbles. The bubble detection algorithm often detected bubbles larger than the median but in general it consistently detected the same range of values (the interquartile range in all boxplots is relatively similar). The fact that the third quartile is generally larger than the first quartile in all boxplots can be the result of the algorithm detecting bubbles that either already coalesced with other bubbles when photographed or absorbed O_2 from the neighboring water. I calculated the average bubble detachment radius (the average of all medians of each boxplot, see Figure 3.5) to be 22.47 µm; this value is similar to the ones reported by other sources [99][54][65].

Thus far, I have displayed images of bubbles that are already detached from the electrode or large enough to occlude observing the electrode where they evolve, but the question of how bubbles evolve at the electrode level remains unanswered. To obtain insights into how bubbles evolve, I recorded images of the electrode using the same setup and conditions as the pictures in Figure 3.4, only this time I used a VPS-coated Ti-mesh as the PTL. The reasoning behind the choice of PTL is that the Ti-mesh that I used has wide crevices, which display a large portion of the electrode and prevent us from clearly distinguishing the bubbles still attached to the electrode in the background. The two main factors that helped me record images of bubbles attached to

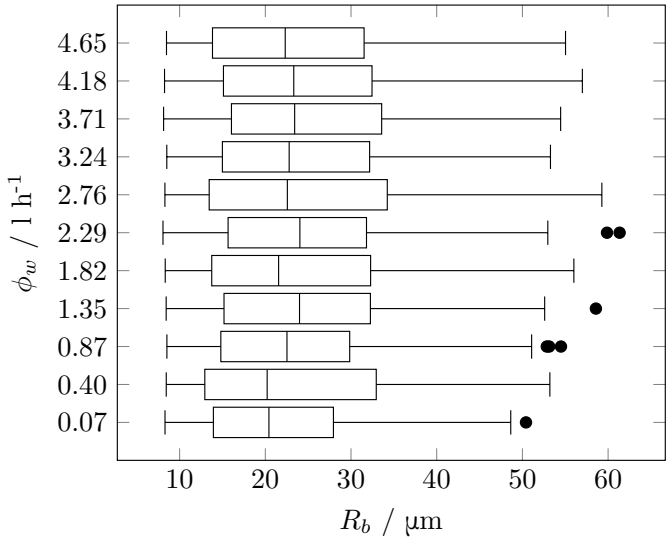

Figure 3.5: Box plots of the bubble detection performed (using MATLAB) as a function of water flow. I used photographs similar to Figure 3.4; a total of 2956 images were processed. The average of the medians of all box plots is 22.47 µm. The dots located outside the upper error bars correspond to outliers.

the electrode were the modest in-plane electric conductivity of Ir-black (which allows gas evolution on active sites relatively far from where PTL and electrode are in contact) and the matte finish obtained with the VPS treatment (which prevented excessive light reflection by the PTL, instead allowing the bubbles to reflect light and therefore be more clearly distinguishable).

Figure 3.6 shows a time lapse of bubbles evolving on the electrode with the VPS-modified Ti-mesh. At t=0 s, the electrode is evolving new bubbles. At t=0.97 s, bubbles with a radius of approximately 10 µm are visible on the electrode surface. At t=1.24 s, some bubbles have reached a radius of 25 µm (similar to what I measured as the median bubble detachment radius in Figure 3.5). At t=1.34 s, some bubbles are absorbed by a larger, already detached bubble, and the cycle starts anew. An important finding is that I identified hotspots at which bubbles always evolve. At t=12.00 s and t=34.38 s, bubbles are evolving on the same spots as at t=1.24 s. The presence of hotspots is relevant for the design of PEM electrolysis components; a PTL can be designed to maximize the amount of pores positioned atop the electrode hotspots, or an electrode

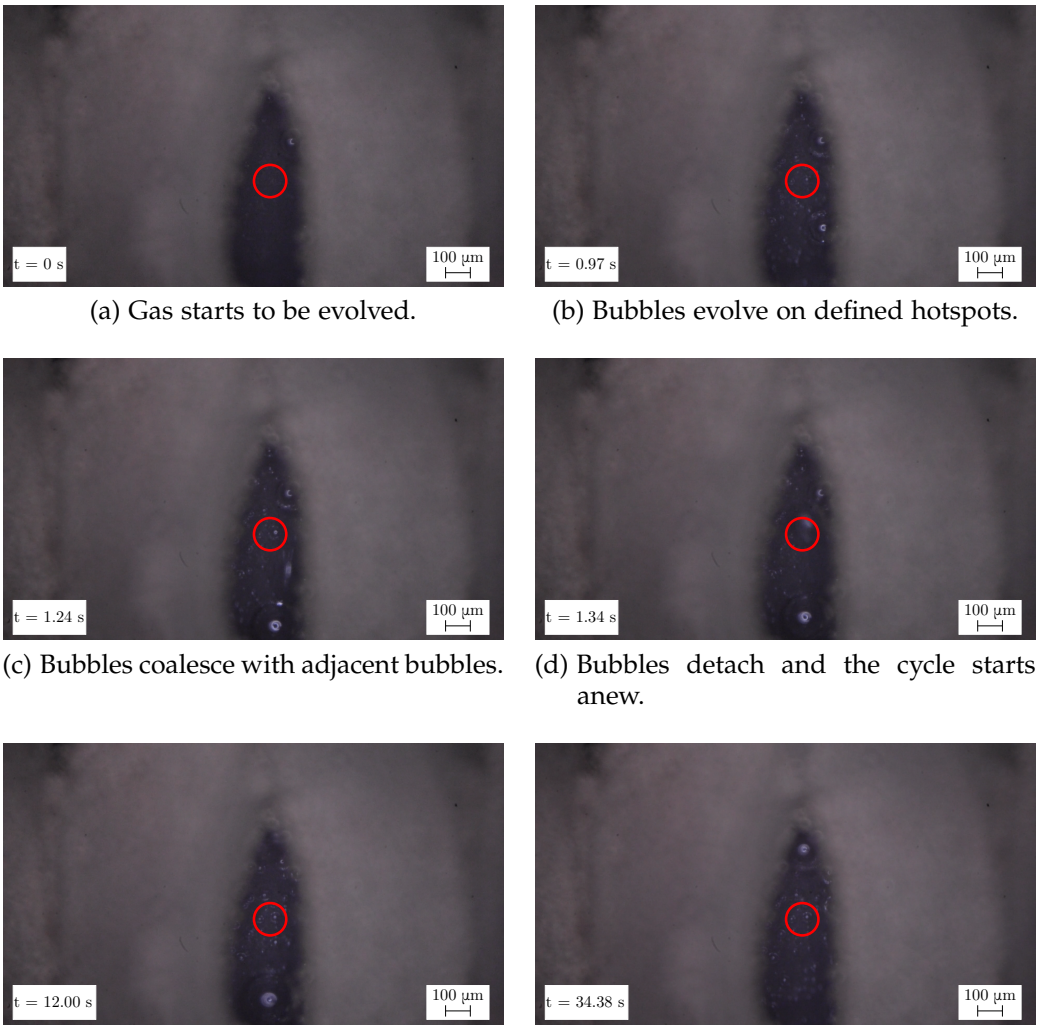

(a) Gas starts to be evolved.

(b) Bubbles evolve on defined hotspots.

(c) Bubbles coalesce with adjacent bubbles.

(d) Bubbles detach and the cycle starts anew.

(e) Bubbles evolve at the same hotspots at 12 s.

(f) Bubbles evolve at the same hotspots at 34.38 s.

Figure 3.6: Photographs taken under the same conditions as Figures 3.3 and 3.4 but using a VPS-coated Ti mesh; I highlighted a section of the exposed electrode (red circles) as a reference.

can be designed to align its hotspots with a certain PTL. Moreover, I believe that the visual identification of hotspots and how they vary with ink composition, coating technique or drying method can be crucial for the development of MEA manufacturing techniques in PEM electrolysis.

3.3.4 *Bubble force balance and sensitivity analysis*

To model the detachment radii measured with the bubble detection algorithm (Figure 3.4), I used the bubble force balance developed by van Helden et al. [109]. Previous works have focused on bubbles exiting the PTL, but thus far, none of the published studies have reported modeling of bubble evolution at the electrode level [69]. According to van Helden and colleagues, bubbles become detached whenever the forces that act on the bubbles at the electrode surface reach equilibrium [109]. This implies that it is not the drag exerted on the bubble that causes it to detach but rather the sum of buoyancy, surface tension and lift forces exerted by water (which is orthogonal to the drag) that govern bubble detachment (see Figure 3.1).

Figure 3.7 shows the simulated bubble detachment radii as a function of water flow rate using the bubble force balance. Each of the colored lines of both figures represent a pore diameter. Bubbles evolve on top of the electrode pores where there is a local interfacial tension maximum (between electrode and water); hence, it is more energetically favorable for a bubble to evolve on that particular pore. The presence of pores on the electrode surface refers to the channels that connect the PTL with the membrane, although a pore in this sense can also be a concave crevice on a catalyst particle; therefore, rugged electrodes could potentially offer more active sites for bubble nucleation. I found that an electrode pore radius (R_p) of 26.2 µm can reproduce the average bubble detachment radius of 22.47 µm observed in Figure 3.5. I modeled two cases: a flow field with 1 channel (such as in the portrayed experiments) and a flow field with 25 channels, where water would be 25 times faster and therefore exert larger drag and lift forces. The behavior of the detachment radius with water flow follows what I measured with the bubble detection experiments namely, at low water flows, the detachment radius remains constant, and it increases slightly with increasing water flow (more observable in the simulation with 25 channels in Figure 3.7).

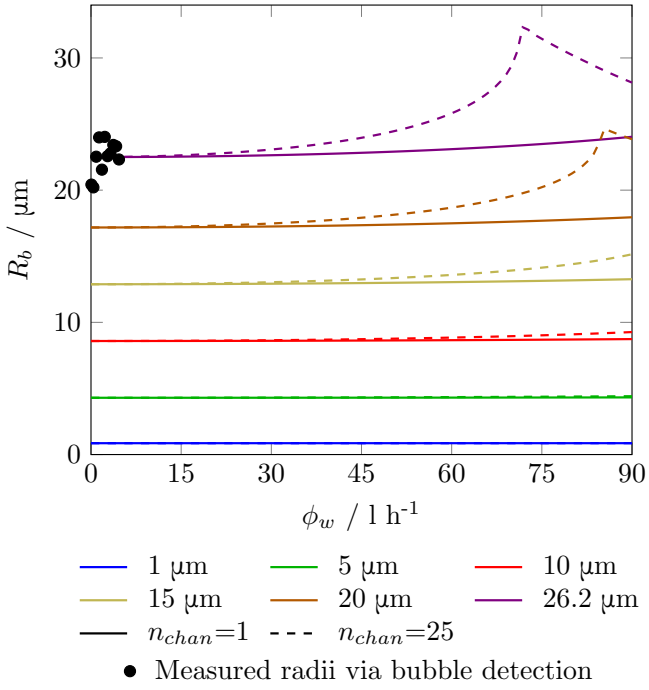

Figure 3.7: Bubble detachment radii as a function of water flow, modeled with the bubble force balance. Each colored line represents the diameter of a theoretical pore on whose throat a bubble evolves. (Solid lines) Simulations with a flow field containing 1 channel (Figure 3.3). (Dashed lines) Simulations with a flow field containing 25 channels (Figure 2.5). (Dots) Median bubble detachment radii measured via bubble detection (see Figure 3.5).

The role of the acting forces on the bubble diameter is depicted in Figure 3.8. The surface tension force (F_σ) is considerably larger than any of the other forces; therefore, it appears to be the force that governs the detachment radius. The corrected buoyancy force (F_{Bx}) is the second largest force in magnitude, while both lift forces (F_{L1} and F_{L2}) are much smaller than the surface tension and the corrected buoyancy forces, particularly at low water flows (which is to be expected). At higher water flows, the increase in the lift force causes a decrease in the corrected buoyancy force; the augmented lift force will cause larger bubbles. Moreover, Figure 3.8 shows the effect of the number of flow field channels on the force balance. A flow field with 25 channels has a larger per-channel water velocity that would cause a higher lift than a flow field with a single, wide channel; this effect causes the increase in the lift force 1 (F_{L1}) at

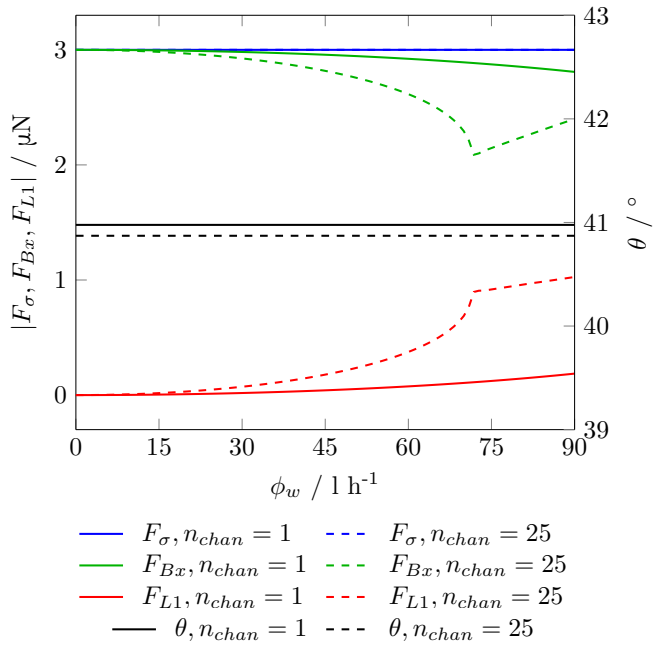

Figure 3.8: Forces acting on an evolving bubble as a function of water flow, modeled with the bubble force balance using R_p = 26.2 µm. (Solid lines, red, green and blue) Simulations with a flow field containing 1 channel (Figure 3.3). (Dashed lines, red, green and blue) Simulations with a flow field containing 25 channels (Figure 2.5). (Black lines, right axis) Bubble detachment angle as a function of water flow.

water flows larger than 60 l h^{-1}. The steep increase in the lift force causes the corrected buoyancy force (F_{Bx}, see equation 3.2) to decrease (to maintain the force balance), subsequently increasing the bubble detachment radius compared to the 1-channel flow field scenario, as can be seen in Figure 3.7. The increased detachment radius caused by the lift force at higher water flows can cause mass transport losses in an operating PEM electrolysis, due to larger bubbles blocking water from reaching the catalytically active sites (bubble shading).

Figure 3.8 shows the effect of water flow on the detachment angle. A detachment angle close to zero means that the bubble detaches parallel to the electrode, whereas an angle close to 90°means that the bubble detaches orthogonal to the electrode. I calculated a detachment angle of 41° for the 1 channel simulation and a slightly smaller angle for the 25 channel simulation. An angle

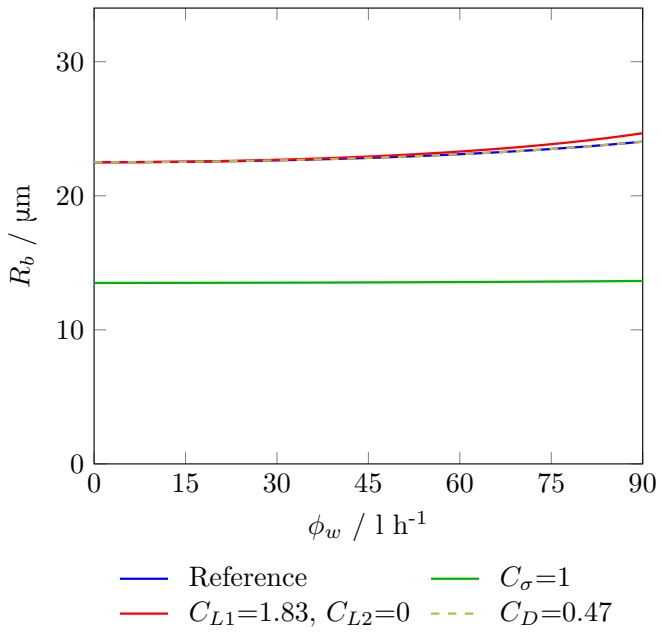

Figure 3.9: Sensitivity of the bubble detachment radius to the force coefficients (using R_p = 26.2 µm) according to table 3.1, as a function of water flow.

close to 45°means that the forces in the x- and y-directions (minus the surface tension force) have equal magnitude, which is the case in the depicted simulations considering that the lift force (F_{L1}) and the drag (F_D) are the largest forces that the bubble experiences after detaching from the electrode. According to equations 3.3 and 3.7, the only difference between drag and lift is the magnitude of the respective coefficient; with 25 channels, lift and drag on the bubble increase by an almost equal amount, with drag increasing ever slightly. In Figures 3.7 and 3.8, we observe an increase in the bubble radius and lift force until they reach a maximum and then proceed to start decaying. This result comes from the dependence of the lift force on the square of both the bubble radius and the water velocity, which causes the bubble radius to exhibit a bubble-controlled lift force region (until 70 l h^{-1}), as well as a flow-controlled lift force region (upward of 70 l h^{-1}).

As already discussed in the modeling section, I performed a sensitivity analysis of the bubble force balance with varying force coefficients [109]. Figure 3.9 shows the sensitivity of the detachment radii; as expected, the surface ten-

sion force coefficient dominates the detachment radii. A high sensitivity to the surface tension force means that measurements regarding contact angle and surface tension need to be carried out with considerable precision, but the most important consequence is the role of the electrode hydrophobicity on the bubble radii. Doubling the surface tension force (via an increase in the force coefficient, C_σ) halved the detachment radius for the same value of R_p (primarily due to the corrected buoyancy force F_{Bx}, see equation 3.2). At low values of the bubble detachment radius ($R_b < 1000$ µm), the second term of the right-hand side of equation 3.2 (the Young-Laplace equation) dominates the total force, while the first term of the right hand side (the weight of the surrounding water) dominates at larger detachment radii. Since F_{Bx} is the main force that counteracts the surface tension force, a smaller bubble will break free from a more hydrophobic electrode (equation 3.1). This result can serve as a guideline for future electrode designs.

Figure 3.10 depicts the sensitivity of the forces and the detachment angles with the changes in the force coefficients C_σ, C_{L1}, C_{L2}, and C_D. F_σ and F_{Bx} are the forces that are most sensitive to changes in the surface tension force coefficient, C_σ. For the lift coefficients, we can observe a small change when I used the second pair of lift coefficients proposed by van Helden et al. [109], confirming that the lift exerted by water has little say in determining the bubble detachment radius. In general, water flow does not affect the detachment radius up to 60 l h^{-1}. The bubble detachment angle (Figure 3.10, right) is insensitive to the surface tension force coefficient because the surface tension force no longer acts on the bubble after it has detached. We observe a slight decrease in the angle with an increased lift coefficient, C_{L1}, but the most impactful change is the decrease in the drag coefficient, C_D. A reduction in the drag coefficient would cause the lift force to dominate the detachment angle (equation 3.8), thereby causing the bubble to flow further away from the electrode after it detaches. From the observed behavior in Figure 3.6, bubbles tend to detach almost parallel to the electrode surface (at least at an angle significantly lower than 90°). During the course of the experiments, I did not observe any bubble

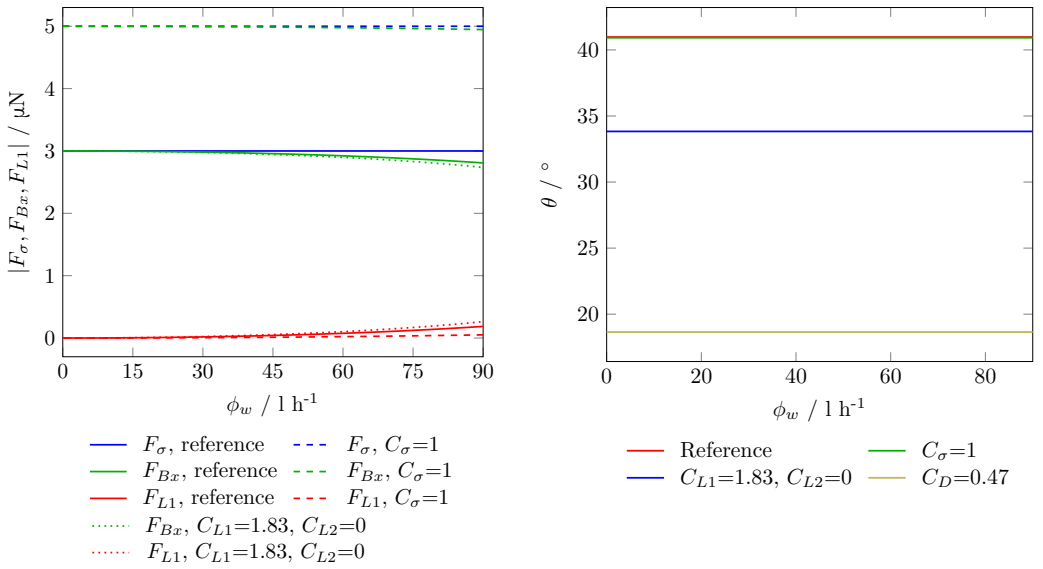

(a) Sensitivity of the forces.

(b) Sensitivity of the detachment angle.

Figure 3.10: Sensitivity of forces acting on an evolving bubble and the bubble detachment angle to the force coefficients (using R_p = 26.2 µm) according to table 3.1, as a function of water flow.

that detached perpendicularly, thus confirming that the drag coefficient must have a significantly larger value than the one proposed by AlHayes and Winterton [2] or that the lift coefficient is much smaller than the value proposed by van Helden and colleagues [109] (which would be the case with water being an axisymmetric flow).

3.4 CONCLUSION

In this chapter, I explored the dynamics and evolution of O_2 bubbles on the anode side of a PEM electrolyzer. I showed images of bubbles flowing in a flow field, where I discussed how the two-phase flow regime affects both the fluid-to-fluid friction and the wall fraction. The results suggest that the main role of water flow in gas evolution lies in the pressure drop it causes the system, originated from an increase in the wall friction; water flow should be kept at a minimum to optimize the pressure losses, although the optimal water flow

will necessarily be a function of the flow field design. Moreover, I showed images portraying bubble growth through the pores of a PTL. I identified two types of bubbles: bubbles that reach a detachment radius and freely float on the surrounding water, and bubbles that coalesce with the neighboring bubbles and absorb the dissolved gas in water, growing as large as the pores that contain them. I discussed the importance of promoting only the evolution of small bubbles to avoid bubble shading and how parameters such as hydrophobicity and pore/particle size can have a role in determining bubble sizes.

I presented microscopic images of detached bubbles from the electrode, which I subsequently processed with an image processing algorithm to find a dependence between the bubble detachment radius and water flow. I found that the bubble detachment radius is constant for a wide span of water flows. I modeled these results with a bubble force balance that takes into account the effects of surface tension, contact angle and water velocity, among other parameters. The bubble detachment radius was found to be largely determined by the surface tension force, which is in turn a function of the contact angle between the electrode and the surrounding water, as well as the surface tension between water and O_2. The model also revealed that the detachment radius does not depend on the drag force induced by the water flow nor on any force orthogonal to the bubble growth. The detachment radius is determined solely by a force balance on the growth axis of the bubble.

4

GAS PERMEATION THROUGH POROUS TRANSPORT LAYERS

4.1 INTRODUCTION

There is no real consensus on what is meant by mass transport losses in a PEM electrolyzer. Abdol Rahim et al. mention three discernible transport mechanisms: water transport to the anode, diffusion transport of the evolved gases, and electro-osmotic transport of water across the ionomer [1]. Of the three mechanisms, the combination of the water and gas transport within the PTL is considered the source of the mass transport limitations [28][1][93][47]. The common interpretation of the mass transport in a PTL is that there exists a two-phase flow [38][84][45][5], where water flows toward the electrode and the gas flows away from it [69]. Traditional modeling of mass transport losses includes the effect of this two-phase flow (sometimes referred to a momentum-driven approach, see [17]), and it is often combined with the use of Fick's first law to relate the concentration gradient of both evolved gases (H_2 and O_2) to the mass transport overpotential [28][71][96] (also known as diffusion-driven approach, see [17]).

I have reason to believe that the common interpretation of mass transport in a PEM electrolyzer does not fully reflect the transport mechanisms in a PEM electrolyzer. According to Vogt and Stephan, the mass transport of gas in a gas-evolving electrode is largely determined by gas agglomerating and exiting the cell through the PTL, rather than driven by a concentration gradient while still dissolved in water, where its behavior can be modeled using Fick's law [100][102]. Moreover, it is controversial that the flow through the PTL occurs in two phases: according measurements conducted by Lee and colleagues, gas

travels through the PTL as a single phase, where it displaces the water contained in the pores, thus as a permeating flow rather than a two-phase flow [49][50]. These results have lead me to propose an alternative set of experiments that can bring more insight into the problem of mass transport losses in a PEM electrolyzer.

In this chapter, I present the results of a simulated gas evolution test I carried out: I propose an experimental setup that intends to recreate the mass transport phenomena occuring in the PTL of a PEM electrolyzer. I measured the effect of water flow on the gas transport across the PTL, and I compared the energy expenditure of the gas flowing through the pore network of the PTL (measured as pressure loss) of two different scenarios namely, assuming that gas flows as a one-phase flow and assuming that gas permeates through the PTL. The one-phase flow scenario is meant to represent a limiting case of the more general two-phase flow that has been discussed previously: a two-phase flow will exhibit friction losses caused by the wall-fluid interaction of the water flowing in the annulus of each pore, as well as friction losses in the gas-water interface. A one-phase flow would only exhibit wall-fluid friction losses, and such losses will be approximately three orders of magnitude lower for a gas than for a liquid (given that the friction losses are proportional to the fluid density, according to the Darcy–Weisbach equation). Therefore, the friction losses of a one-phase flow are the lowest possible losses a more general two-phase flow would exhibit.

4.2 MODELING

4.2.1 *Energy balance*

The differential energy balance (ignoring the changes in liquid kinetic energy and gas potential energy) on the experimental setup is described in equation 4.1 [15]

$$V_g dV_g + \frac{dP_g}{\rho_g} + \frac{dP_w}{\rho_w} + \dot{g} dz_w + H_{total} = 0 \tag{4.1}$$

where V_g is the gas velocity, dV_g is the differential gas velocity, dP_g is the gas differential pressure drop, ρ_g is the gas density, dP_w is the water differential pressure drop, ρ_w is the water density, $\dot{g}$ is the terrestrial gravity acceleration, and dz_w is the differential height increase in the flowing water.

The term H_{total} in equation 4.1 represents the sum of the friction head loss of the water from the pump outlet to the cell inlet, and of the two-phase flow along the channels of the cell flow field, as shown in equation 4.2

$$H_{total} = f_D^w \frac{1}{2} \frac{V_w^2}{D_h^p} dL_p + f_D^{lg} \frac{1}{2} \frac{V_{lg}^2}{D_h^{ff}} dL_{ff} + H_{other} \tag{4.2}$$

where f_D^w is the Darcy friction factor of water flowing, V_w is the water velocity, D_h^p is the hydraulic diameter of the pipe where water flows, dL_p is the differential pipe length, f_D^{lg} is the Darcy friction factor of the two-phase flow (water and gas in the flow field of the test cell, see Figure 2.7), V_{lg} is the two-phase flow velocity, D_h^{ff} is the hydraulic diameter of a flow field channel, and dL_{ff} is the differential flow field channel length. The term H_{other} represents the leftover head loss caused by the gas crossing the PTL.

I consider two cases regarding the friction head loss of the gas crossing through the PTL:

1. Head loss as if gas were a one-phase flow through the PTL (head loss modeled with the Darcy–Weisbach equation).

2. Head loss as gas permeating through the PTL (head loss modeled with Darcy's permeability law).

As I mentioned in the introduction of this chapter, I consider the one-phase flow through PTL to be a special case of a more general two-phase flow through pores. As we will see further on, a two-phase flow shows higher friction losses due to the friction between phases; in light of this, the losses of a one-phase flow would be smaller than a two-phase flow that might happen in the PTL pores. Equation 4.3 shows the respective equations for each case (one-phase and permeation)

$$H_{other} = \begin{cases} \text{One-phase flow} & f_D^g \frac{1}{2} \frac{V_g^2}{D_h^{pore}} dL_{PTL} \\ \text{Permeation} & \frac{\mu_g V_g}{\rho_g K_g} dL_{PTL} \end{cases} \tag{4.3}$$

where D_h^{pore} is the hydraulic diameter of the PTL pores, dL_{PTL} is the differential PTL thickness, μ_g is the gas viscosity, and K_g is the gas permeability through the PTL.

I define the continuity equation for the gas flow in the PTL as

$$\dot{m}_g = \rho_g A_{PTL} V_g \tag{4.4}$$

and the ideal gas law as

$$\rho_g = \frac{P_g}{R_m T} \tag{4.5}$$

where $\dot{m}_g$ is the gas mass flow rate, A_{PTL} is the cross-sectional area of the PTL, P_g is the pressure in the PTL pores, R_m is the universal mass gas constant, and T is the temperature of the system.

I calculated the universal mass gas constant for each gas as

$$R_m = \frac{R}{M_g} \tag{4.6}$$

where M_g is the gas molar mass.

Inserting equations 4.2, 4.3, 4.4, and 4.5 into equation 4.1, using the pressures from the experimental setup (see Figure 2.8), rearranging and integrating, yields

$$2ln\frac{P_1}{P_2} + \frac{A_{PTL}^2}{\dot{m}_g^2 R_m T}(P_2^2 - P_1^2) + \frac{f_D^{lg}}{D_h^{ff}}L_{ff} + \left[\frac{P_3 - P_2}{\rho_w} + \frac{f_D^w V_w^2}{D_h^p}L_p + \dot{g}\Delta z_w + H_{other}\right]\left(\frac{\rho_g A_{PTL}}{\dot{m}_g}\right)^2 = 0 \tag{4.7}$$

where L_{ff} is the flow field channel length, L_p is the pipe length, and Δz_w is the total height increase in the flowing water. I solved equation 4.7 for each experiment, obtaining in each case the value of H_{other}.

The Darcy friction factor of either water or gas can be calculated using the relationship depicted on equation 4.8; this equation can be derived from the Hagen–Poiseuille equation, which calculates the pressure drop of a laminar flow in a channel with a circular cross-section

$$f_D = \frac{64}{Re} \tag{4.8}$$

4.2.2 *Two-phase pressure drop*

I modeled the pressure drop along the flow field channels according to the Lockhart–Martinelli model [58][43][55]

$$\chi^2 = \frac{\partial P_w}{\partial P_g} \tag{4.9}$$

$$\varphi^2 = \frac{\partial P_{lg}}{\partial P_w} \tag{4.10}$$

where ∂P_w, ∂P_g, and ∂P_{lg} represent the pressure drop (caused by friction) of the water, the gas and the two-phase flow, respectively. Equations 4.9 and 4.10 depict the interdependence of the pressure drops for all three flows, and they can be combined to express the two-phase pressure drop as a sole function of the gas pressure drop.

The relationship between both Lockhart–Martinelli parameters χ and φ is [18][43]

$$\varphi^2 = 1 + \frac{C}{\chi} + \frac{1}{\chi^2} \tag{4.11}$$

where C, also known as the Chisholm parameter, depends on the flow regime of each phase (water and gas); in this case, the Re number of neither phase exceeded the transient threshold ($Re < 2100$) during the gas permeation measurements; therefore, $C = 5$.

The χ parameter in equation 4.11 is related to the flow quality and the viscosity ratio between gas and liquid, according to equation 4.12

$$\chi^2 = \frac{1 - x}{x} \frac{\mu_w}{\mu_g} \tag{4.12}$$

where x is the flow quality of the two-phase stream, defined as

$$x = \frac{\phi_g}{\phi_g + \phi_w} \tag{4.13}$$

where ϕ_g and ϕ_w are the volumetric flows of gas and water, respectively. According to equation 4.13 a flow quality of 0 means that the flow is 100% water, while a value of 1 means that the flow is 100% gas.

To insert directly the value of ∂P_{lg} from equation 4.10 to the energy balance (equation 4.7), I combined equations 4.9 and 4.10 with the definition of friction head (equation 4.14) to give equation 4.15

$$H = \frac{\partial P}{\rho} \tag{4.14}$$

$$f_{lg} = \frac{\chi^2 \varphi^2}{(1 - x)} \frac{\rho_g}{\rho_w} \frac{56.91}{Re} \tag{4.15}$$

The value 56.91 in equation 4.15 corresponds to a coefficient derived by Berker to calculate the Darcy friction factor of laminar flow in a channel with a square cross-section [12]; compare it to the value of 64 in equation 4.8. This coefficient takes into account the contact between fluid and channel walls; there

appears to be less contact in a square channel than in a circular channel, considering that a prismatic channel has more wall area per channel length than a cylindrical channel.

The calculation of the gas head loss assuming a one-phase pressure loss allows us to set a limiting case i.e., a minimum head loss that can be compared with the head loss calculated as if the gas flow were permeating through the PTL.

4.2.3 *Permeability*

The Darcy–Weisbach equation for permeability (shown as head loss using equation 4.14) is depicted as

$$H_{perm} = \frac{\mu_g V_g L_{PTL}}{\rho_g K_g} \tag{4.16}$$

where H_{perm} is the head loss caused by permeation, L_{PTL} is the PTL thickness, and K_g is the total gas permeability.

The total gas permeability is defined as

$$K_g = k_g k_{g,r} \tag{4.17}$$

The term k_g in equation 4.17 corresponds to the gas permeability in a free medium (without taking into account the morphology of the porous medium or, in this case, the effect of water in the PTL), whereas the term $k_{g,r}$ is known as the relative gas permeability, which I will discuss later.

The gas permeability is related to the water permeability through Klinkenberg's equation [21][41]

$$k_g = k_w \left(1 + \frac{4\lambda}{R_h^{pore}} \right) \tag{4.18}$$

where k_w is the water permeability in a free medium, λ is the mean-free path of the gas, and R_h^{pore} is the hydraulic radius of the pore.

I calculated the mean-free path of gases according to equation 4.19 [21].

$$\lambda = \frac{\mu_g}{P_g}\sqrt{\frac{\pi R_m T}{2}} \tag{4.19}$$

The $k_{g,r}$ term in equation 4.17 is defined as the relative gas permeability, which is a function of the water saturation in the pores (and in this case can contain the effect of water flowing in front of the pores) [41]. The dependence of $k_{g,r}$ with the pore properties can be modeled using an equation derived from the van Genuchten–Mualem model [41]

$$k_{g,r} = (1 - S^*)^{1/2}\left(1 - S^{*1/m}\right)^{2m} \tag{4.20}$$

where S^* is the pore water saturation, and m and n are parameters from the van Genuchten–Mualem model. Parameter m from equation 4.20 can be calculated by different techniques, including simulations based on 3D imaging [51] and direct capillary pressure measurements [41].

The dependence of capillary pressure with pore water saturation is given by the van Genuchten–Mualem model

$$P_c = \frac{1}{\alpha_{vgm}}\left[S^{*-1/m} - 1\right]^{1/n} \tag{4.21}$$

where P_c is the capillary pressure, and α_{vgm} is a third van Genuchten-Mualem parameter (with units Pa^{-1}).

4.2.4 *Permeability and tortuosity*

I identify two main water flows occurring in the experiment. One water flow is the one pumped by the dosing pump, which flows in-plane with respect to the PTL (see Figure 2.7); this is the water flow that is depicted in the main axis of all graphs in this chapter. I call this water flow the "orthogonal" or the "in-plane" water flow since its flow direction is orthogonal to the pores and flows parallel to the surface of the PTL. The second water flow is the water that would flow from one side of the PTL to the other (therefore in the through-plane direction of Figure 2.7), and I refer to this water flow as "normal" or

"through-plane" water flow since it flows in the direction of the pores and across the PTL. Due to the experimental setup, I did not measure the through-plane water flow. Most of the in-plane water stream will flow in and out of the testing cell without entering a pore, and only a small fraction of the in-plane water flow will become through-plane water flow by entering the pores and reaching the other side of the PTL.

My initial hypothesis was that the permeating gas undergoes two pressure drops: one caused by the porous medium (the PTL) and another one caused by the presence of the in-plane water flow. The porous medium will fill with water, impeding the passage of gas; while the in-plane water flow will block the pore exits, thereby exerting a force to the oncoming gas through the PTL. Mathematically, I assume that the pressure drops (or head losses, as I have been using this nomenclature throughout this chapter) occur in series

$$H_{perm} = H_{perm,fric} + H_{PTL} + H_{water} \tag{4.22}$$

where $H_{perm,fric}$ is the head loss caused by the friction of the permeating gas, H_{PTL} is the head loss of gas permeation, and H_{water} is the head loss caused by the flow of water at the other side of the PTL.

$H_{perm,fric}$ is calculated as a one-phase flow through pores with a length equal to the PTL thickness

$$H_{perm,fric} = f_D^g \frac{1}{2} \frac{V_g^2}{D_h^{pore}} L_{PTL} \tag{4.23}$$

All H values from equation 4.22, except for $H_{perm,fric}$, are calculated by Darcy's law (equation 4.16) and they share the same parameters (see equation 4.16) save for the permeability coefficients.

After subtracting $H_{perm,fric}$ and using equation 4.16 on each H in equation 4.22, and subsequently using equation 4.17, equation 4.22 reduces to

$$\frac{1}{k_g k_{g,r}} = \frac{1}{k_g} + \frac{1}{k^*} \tag{4.24}$$

The parameter k^* from equation 4.24 is a permeability coefficient that is a function only of the water in the pores and the in-plane water flow. Solving equation 4.24 for k^* leads to equation 4.25

$$k^* = k_g \left(\frac{1}{k_{g,r}} - 1 \right)^{-1} \tag{4.25}$$

According to the Carman–Kozeny equation [41], a similar form known as the Blake–Kozeny equation [14], the permeability of a fluid in a porous medium is a function of the porous medium properties

$$k^* = \alpha \frac{{D_{particle}}^2 {\epsilon_{ap}}^3}{(1 - \epsilon_{ap})^2} \tag{4.26}$$

where α is a Carman–Kozeny parameter, $D_{particle}$ is the diameter of the particle that was sintered to form the sintered porous medium, and ϵ_{ap} is an apparent porosity of the PTL pores. It is important to mention that the parameter ϵ_{ap} in equation 4.26 refers to an apparent change in the PTL's porosity, which means that the PTL is not undergoing changes of its pore structure during operation but rather that the permeating gas is losing energy as a result of the water blocking its path. I am accounting for the energy loss with the term ϵ_{ap} by assuming that the gas flows through a PTL with a lower porosity. As I will discuss later, this behavior can be understood as a source of the mass transport losses in a PEM electrolyzer.

The term $D_{particle}$ (the particle size of the PTL) is not a parameter typically reported during production of PTLs. I calculated the dependence of the particle size on the PTL pore size using data measured by Grigoriev et al., who characterized different PTLs produced by sintering Ti particles of different sizes [35]; from their results I obtained

$$D_{particle} = \frac{D_{pore}}{0.2133} \tag{4.27}$$

Finally, I calculated an apparent tortuosity as a function of the apparent porosity from equation 4.26 using Bruggeman's equation [20][74] (equation 4.28)

$$\tau_{ap} = \frac{1}{\epsilon_{ap}^{1/2}} \tag{4.28}$$

The concept of apparent tortuosity helps me explain the results in a clearer manner. A PTL will have pores whose minimum length is L_{PTL}, the PTL thickness. Since the PTL pores are hydrophilic, they will fill with water as soon as water comes in contact with the PTL, as is the case in the experimental setup. As I discussed earlier, gas will permeate through the pores, displacing water on its path until it exits the PTL. Since water represents an obstacle to the gas flow, the energy expenditure from the gas flow can be understood as an increase in the relative length of the PTL pores, which is represented by τ_{ap}.

A second route to calculate the head loss (see equation 4.3) is to treat the gas flow as a one-phase flow through the PTL pores (which in turn is a limiting case of a more general two-phase flow). I calculated an apparent tortuosity of the one-phase flow using the definition of friction head loss and tortuosity (equations 4.29 and 4.30)

$$L_{pore} = \frac{2H_{other}D_h^{pore}Re_g}{64V_g^2} \tag{4.29}$$

where Re_g is the Reynolds number of the gas flow through the pores. The apparent tortuosity of a one-phase gas flow, $\tau_{ap,1phase}$ is calculated as

$$\tau_{ap,1phase} = \frac{L_{pore}}{L_{PTL}} \tag{4.30}$$

Both apparent tortuosity values (of permeation and one-phase flow) will help me compare the energy requirements for both processes to occur; the process with the lowest tortuosity will be the process that is energetically favored to take place.

The following algorithm summarizes the calculation of the apparent tortuosity from the permeability measurements:

1. I applied the mass balance to the measurements (equation 4.7), to obtain H_{other}.

2. Using equation 4.16, I calculate K_g.

3. Having calculated k_g from the water permeability measurements (the procedure is the same as for the gas permeability), I obtained $k_{g,r}$ using equation 4.17.
4. Subsequently, I calculated k^* using equation 4.25.
5. I solved equation 4.26 for ϵ_{ap}, which I then inserted into equation 4.28 to obtain τ_{ap} .

4.2.5 *Confidence intervals and error propagation*

I calculated the confidence intervals ($CI_{0.05}$) using equation 4.31

$$CI_{0.05} = \bar{m} \pm \frac{t_{Student}\sigma_{sd}}{\sqrt{n_{data\ points}}} \tag{4.31}$$

where $\bar{m}$ is the average of the measurements, $t_{Student}$ is the inverse Student t coefficient (that depends on the number of measurements carried out), σ_{sd} is the standard deviation, and $n_{data\ points}$ is the number of data points averaged. To calculate the propagation of uncertainty of a variable y that depends on a variable x directly measured, I used equation 4.32, which is only valid for one-dimensional equations

$$\sigma_{sd,y} = \left(\frac{dy}{dx}\right)\sigma_{sd,x} \tag{4.32}$$

Table 4.1 summarizes the parameters used to model the results.

4.3 RESULTS AND DISCUSSION

Figure 4.1 shows the result of the water permeation measurements. The slope of the head loss (H_{other} from equation 4.7) is proportional to $1/k_w$, according to equation 4.16 (when applying Darcy's law to water permeation). The dependence of the head loss to water flow is linear with the increase in water flow (since velocity is proportional to the flow); thus, this was a straightforward measurement. I calculated a k_w of $1.34x10^{-13}$ m², in the same order of magnitude

Parameter		Value	Unit
General parameters			
T		295.15	K
A_{PTL}		25	cm^2
Fluid properties			
M_g	N_2	0.028	$kg\ mol^{-1}$
	H_2	0.002	$kg\ mol^{-1}$
μ_g	N_2	$1.74x10^{-5}$	Pa s
	H_2	$8.91x10^{-6}$	Pa s
μ_w		0.001	Pa s
ρ_w		1000	$kg\ m^{-3}$
Flow field properties			
D_h^{ff}		0.001	m
L_{ff}		0.05	m
PTL properties			
$D_{pore} = D_h^{pore}$		$1.6x10^{-5}$	m
L_{PTL}		0.001	m
R_h^{pore}		$8x10^{-6}$	m
Pipe properties			
D_h^p		0.01	m
L_p		2	m
Δz_w		0.6	m
Statistical parameters			
$n_{data\ points}$		720	–
$t_{Student}$		1.97	–

Table 4.1: Parameters used in this chapter.

as impervious rocks such as limestone [10]. I calculated a Carman–Kozeny α coefficient of $1.34x10^{-4}$ m^2, roughly 10^9 larger than k_w.

To estimate the gas permeability of both H_2 and N_2 using the water permeability, I calculated the Knudsen number of each gas (equation 4.33). The

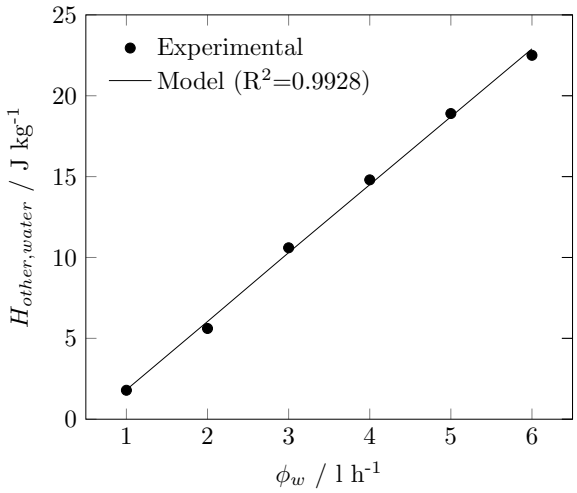

Figure 4.1: (Dots) Permeability head of water as a function of in-plane water flow, obtained from the water permeation tests (dots). (Solid line) Linear regression of the data points; it corresponds to equation 4.16. The calculated water permeability and α (Carman–Kozeny coefficient) are, respectively, $1.34x10^{-13}$ and $1.34x10^{-4}$ m² (see equation 4.26). The error bars are at least three orders of magnitude smaller than the measured data.

Knudsen number is defined as the ratio between the mean-free path of the gas molecules and the hydraulic radius of the PTL pores; a small Knudsen number implies that the gas molecules are less likely to collide with the pore walls, while large Knudsen numbers mean that the gas molecules collide often with the pore walls

$$Kn = \frac{\lambda}{R_h} \tag{4.33}$$

The value of the Knudsen number determines the governing transport phenomenon that gas undergoes in the PTL pores: if $Kn << 1$, (continuum) permeation will dominate the mass transport, whereas if $Kn >> 1$, Knudsen and configurational diffusion become the dominant transport mechanisms [41], which would require a different modeling approach. I found the Knudsen number of both gases in the experiments to be well below 1, therefore validating the assumption that the main transport mechanism through the PTL is permeation rather than Knudsen or configurational diffusion. A small Knudsen number implies that the free-medium gas permeability (that is, the gas permeability

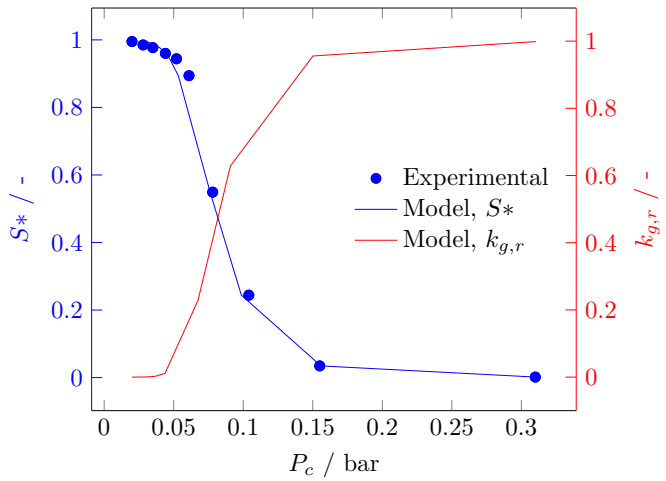

Figure 4.2: (Dots) Capillary pressure of the PTL as a function of the pore water saturation, obtained from the data measured by Lettenmeier et al. [51]. (Blue line) Data modeled with equation 4.21. (Red line) Relative gas permeability as calculated with equation 4.20. Values of the parameters α_{vgm}, m, and n are, respectively, $1.345x10^{-4}$ Pa^{-1}, 0.821, and 5.592.

through water-free pores) is approximately equal to the water permeability (from equation 4.18).

The capillary pressure–pore water saturation curve for the sintered PTL can be found in Figure 4.2. I obtained this graph by adjusting the van Genuchten–Mualem model (equation 4.21) to data obtained by Lettenmeier and colleagues [51], who used tomographic imaging of sintered Ti from the same manufacturer and with similar pore sizes and porosity as the PTLs I used. The zero value of the pore water saturation does not refer to a completely dry PTL but rather to the minimum water content of the PTL, since there will always be a minimum amount of water in the pores that cannot be removed by the non-wetting fluid (the gases), as long as the PTL has access to a source of water [41].

Albeit counterintuitively, Figure 4.2 shows that the relative gas permeability ($k_{g,r}$) increases with the capillary pressure. An increase in the pore water saturation means that the water inside the pores has already reached the maximum pressure head that the capillary pressure can provide i.e., the water level inside the pores is higher than the level it would reach by pure capillarity. With an in-

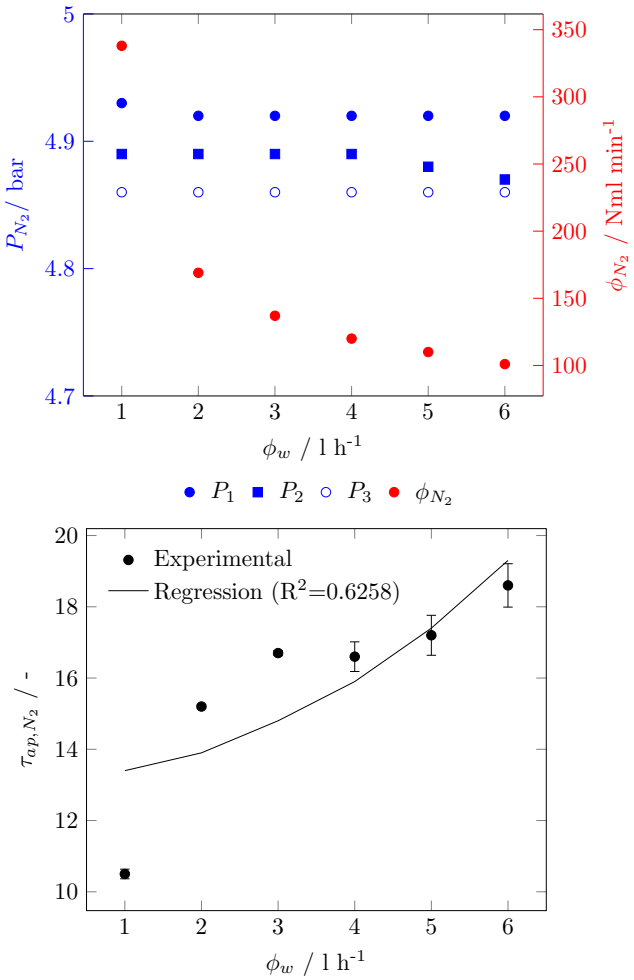

Figure 4.3: (Top) Measured pressures (left axis) and flow (right axis) for N_2 as a function of in-plane water flow, obtained from the N_2 permeation tests. (Bottom) Tortuosity as a function of water flow for the N_2 permeability tests, calculated with equation 4.28; trendline corresponds to equation 4.34.

creased pore water saturation, it is easier for the gas to push through the water because the intrinsic resistance posed by the water in the pores (measured as energy per unit mass, see Figures 4.3 and 4.4) will be lower.

Figures 4.3 (top) and 4.4 (top) show the raw measurements of the gas permeation tests on N_2 and H_2, respectively. From the raw data I calculated the permeation head loss (equation 4.7), and from the permeation head loss I calculated the tortuosity. At first glance we notice that the inlet pressure, P_1,

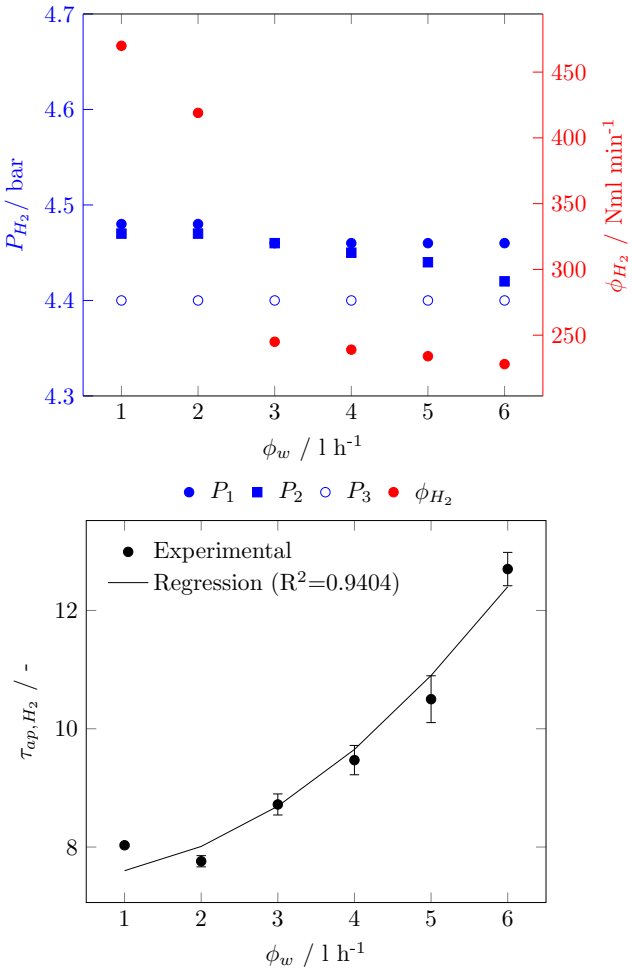

Figure 4.4: (Top) Measured pressures (left axis) and flow (right axis) for H_2 as a function of in-plane water flow, obtained from the H_2 permeation tests. (Bottom) Tortuosity as a function of water flow for the H_2 permeability tests, calculated with equation 4.28; trendline corresponds to equation 4.34.

stayed relatively constant, as did P_3 (the outlet pressure). The only pressure that changed throughout the test was P_2 (the pressure immediately after the PTL), which decreased proportionally to the decrease in gas flow (see the right-hand scale in Figure 4.3). Since I controlled P_3, and P_1 is a pressure externally set by the gas distribution network in our laboratory, the only pressure allowed to change was P_2. The change in gas flow can be explained by the fact that the gas distribution network will have a maximum pressure and flow output

(therefore a maximum head); thus, whenever the downstream pressure drop increases, the gas flow will have to decrease to maintain a constant head. Moreover, we observe in Figures 4.3 (top) and 4.4 (top) that the measured H_2 flow at 2 l h^{-1} water flow is higher than expected when compared to the trend followed by the N_2 flow. Considering that the data depicted in Figures 4.3 and 4.4 is an average of three different measurements and that the anomaly is being consistently detected, I can attribute the anomalous measurement to the H_2 supply system, in particular to the pressure reducer of the H_2 tank. Nonetheless, the trend exhibited by both gases is consistent; therefore, I believe that both datasets are valid.

Figures 4.3 (bottom) and 4.4 (bottom) show the calculated tortuosities for the gas permeation tests on N_2 and H_2, respectively. I calculated the tortuosity using the Carman–Kozeny model (equation 4.26) together with the Bruggeman equation (equation 4.28). We observe an increasing tortuosity on both datasets with an increasing water flow. This increase is most likely related to two main factors: more water being displaced by the gas (thus a lower water saturation in the PTL that causes an increase in the capillary pressure, see equation 4.21) and water flow increasingly blocking the gas path. It is difficult to separate both phenomena given the limited amount of variables measured, so I lumped both effects into a single parameter namely, $k_{g,r}$ (equation 4.20).

I expect that the pore water saturation in the PTL is solely a function of the gas flow and pressure (since the gas flow will displace a proportional amount of water in the pores as long as it has enough energy to do so), whereas the in-plane water flow will influence the permeability independently from both gas flow and pressure. From Figures 4.3 (bottom) and 4.4 (bottom) we observe that the resulting tortuosity of the PTL increases proportionately to the water flow.

Figure 4.5 shows the individual contributions of H_{PTL} and H_{water} to the total permeation losses for both studied gases. According to equation 4.16, the energy losses from the energy balance have three contributions: the friction losses caused by permeation ($H_{perm,fric}$), the energy losses of the permeating

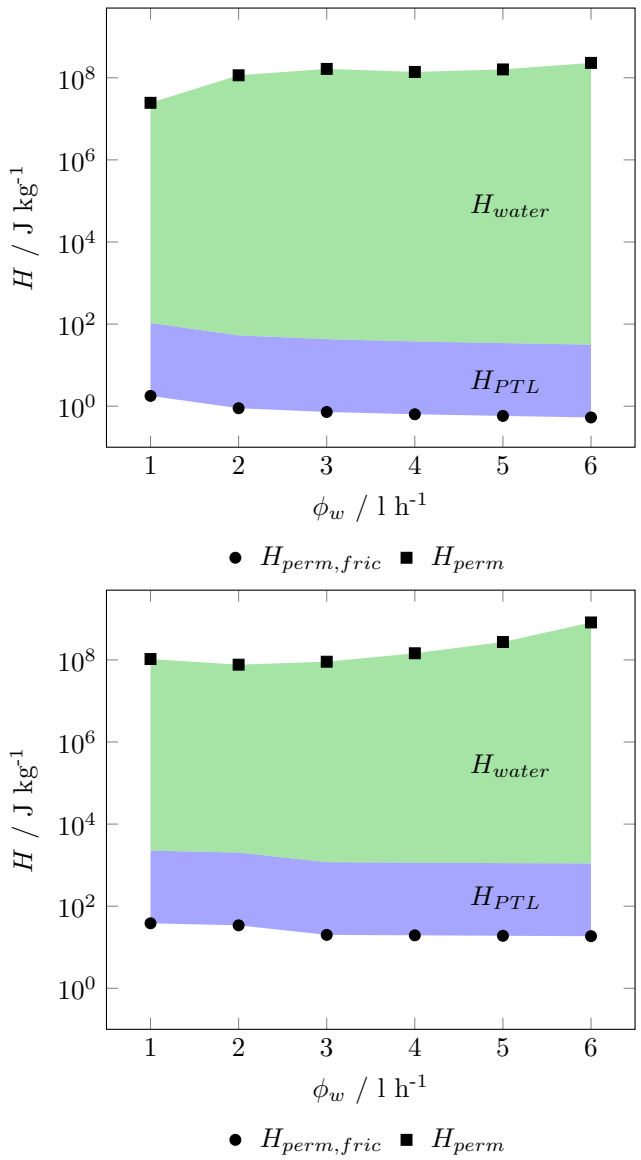

Figure 4.5: (Top) Permeation head losses (H_{perm}) of N_2 as a function of in-plane water flow, with the individual contributions of friction ($H_{perm,fric}$), free-medium permeation (H_{PTL}, blue area), and energy loss caused by the water flow (H_{water}, green area). (Bottom) Permeation head losses (H_{perm}) of H_2 as a function of water flow, with the individual contributions of free-medium permeation (H_{PTL}, blue area) and energy loss caused by the water flow (H_{water}, green area). See equation 4.16.

gas through a water-free PTL (H_{PTL}, see equation 4.24), and the energy losses

of permeating gas through a water-filled PTL (H_{water}). The friction head loss is 2 orders of magnitude larger for H_2 than for N_2 primarily because the friction losses depend on the square of the gas velocity, and H_2 had a higher flow throughout the experiment. We can see in Figure 4.5 that the free-medium permeation losses are similar for both gases, which is to be expected given that the free-medium permeability coefficient is similar for both gases (see equations 4.18 and 4.19). The main difference between the permeation losses of N_2 and H_2 is the effect of water. N_2 appears to be more sensitive to the in-plane water flow. This result appears in line with the change of the measured gas flow rates, where N_2 suffered a flow rate decrease of 70% when the water flow was increased from 1 to 6 l h^{-1}, while H_2 saw a decrease of 50% its initial flow rate.

Alongside the tortuosity as a function of water flow in Figures 4.3 (bottom) and 4.4 (bottom), I used linear regression on the tortuosity data; the equation used is of the form

$$\tau_{ap} = A\varphi_w^2 + B \tag{4.34}$$

There appears to be a strong effect of in-plane water flow that can be understood in terms of kinetic energy. Flowing water has a kinetic energy proportional to the square of its velocity. This kinetic energy could exert a stress orthogonal to the flow direction (shear stress) that the gas flow needs to overcome if it wants to access the flow field channels where water is flowing. The shear stress can be perceived by the gas flow as another impediment for its passage, thereby increasing the pressure drop across the PTL, which is what I measured. The quadratic relationship appears to be more clearly distinguishable for H_2 (with a correlation coefficient of 0.9404) than for N_2 (with a correlation coefficient of 0.6258). The reason behind the worse correlation of N_2 may be the scale of the gas flow measurements. The H_2 flow was between 460 and 480 ml min^{-1}, roughly halfway through the measurement scale of the gas flow meter used, whereas the N_2 flow was between 150 and 180 ml min^{-1}, about 20% of the measurement scale (thus more susceptible to measurement errors). Nevertheless, I identified a quadratic relationship between tortuosity and wa-

ter flow that is attainable to the kinetic energy dependence of the pressure drop in the PTL and that it was somewhat confirmed by the experimental result (in particular for H_2).

The effect of the in-plane water flow is an interesting topic. My hypothesis is that the in-plane water flow causes an additional head loss to the permeating gas because the water flow will exert a shear stress on the pore exit. I did not model this behavior because it was outside of the scope of this work, but I can name the operation of air doors as a similar rheology phenomenon. An air door (or air curtain) in HVAC engineering is a jet of air that is shot vertically at the entrance of a building and its purpose is to minimize the convection between the outside and the inside air [33][88]. The modeling of an air door considers the angle at which the air jet is shot [33], and the model breaks down when the air door is shot orthogonally to the inflow of outside air. Most of the air door modeling is done empirically [33], mainly done for sizing. Another example I can mention regarding the effect of the shear stress of an in-plane water stream is the operation of water-jet cutters. A water-jet cutter is a device that relies on a high-velocity water stream to cut through a variety of materials [103]. There is little information regarding the modeling of water-jet cutters, with the majority dedicated to designing the machine or developing the cutting technique rather than modeling the effect of the water velocity [103]. Nevertheless, water-jet cutters and air doors are examples that confirm the hypothesis that a water stream can exert a shear stress on the PTL pores, causing the gas flow to suffer a further energy loss. Therefore, I can conclude that the head loss of the permeating gas through the PTL is a result of both the pore-water saturation and the in-plane water flow.

Figure 4.6 shows the calculated one-phase tortuosity using the experimental data shown in Figure 4.3 and 4.4 for N_2 and H_2, respectively. We notice that the calculated one-phase tortuosity is up to 8 orders of magnitude larger than the tortuosity calculated using the permeability model; this is an indication that the energy expenditure required by the gas to cross over is extremely large, if the gas were thought of losing energy to friction in the same sense as in

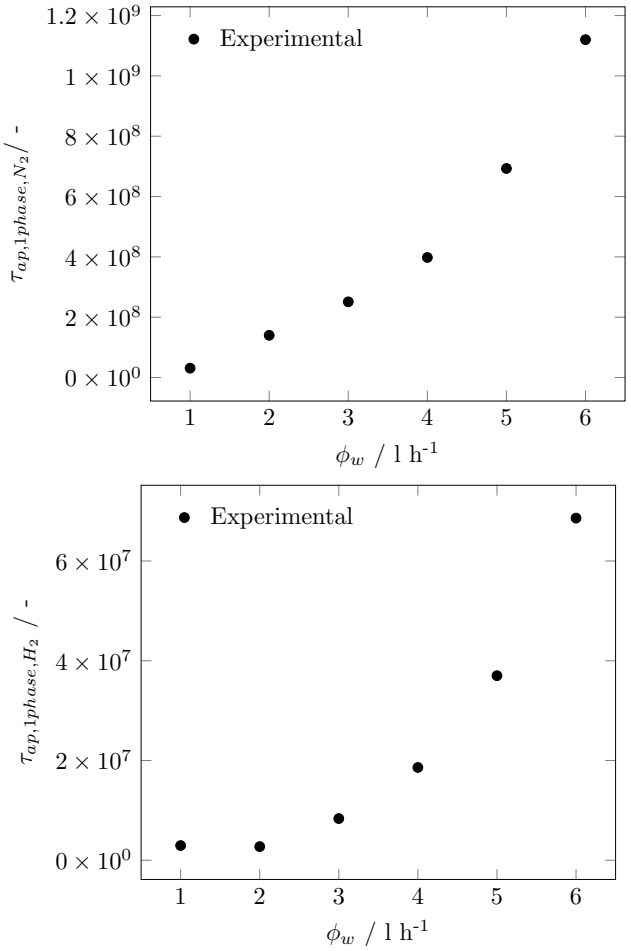

Figure 4.6: (Top) One-phase flow tortuosity as a function of in-plane water flow for the N_2 permeability tests, calculated with equation 4.30. (Bottom) One-phase flow tortuosity as a function of water flow for the H_2 permeability tests, calculated with equation 4.30.

wider channels. We can think of the gas flow through pores as a two-phase phenomenon rather than a one-phase flow: as pointed out by Nicklin, there is a negative wall shear stress when air flows through capillaries [67], which has been interpreted as a counterflow of water with respect to the air [28][69][55]. There is a possibility of water flowing close to the walls of the PTL pores, but I expect that the friction losses of the flowing gas would be nonetheless high (since the two-phase flow will have a larger energy loss than the sum of the

individual losses, due to interfacial stresses between both phases). According to Figure 4.6, this energy loss (interpreted as tortuosity) is significantly higher than the loss caused by a different transport mechanism namely, permeation; therefore, I can conclude that the main transport phenomenon occurring within the PTL is permeation rather than one- or two-phase flow.

If the gases cross the PTL via permeation, the question of how water reaches the electrode of a PEM electrolyzer through the PTL remains unanswered. I come to think that a possible explanation lies within the heterogeneity of pore sizes and lengths within the PTL. It is common for the pore sizes in a PTL not to be homogeneous (especially a PTL that was manufactured by sintering, where the heat distribution and particle size are inhomogeneous by nature); thus, it is highly probable that some PTLs exhibit different pore sizes and, consequently, a different capillary pressure (caused by an asymmetric water saturation). Gas would tend to favor permeating through the pores with the least energy loss (probably the shortest, widest pores), thus leaving the energetically unfavored pores to be full of water, which could naturally flow toward the electrode. Thus, a through-plane water stream will likely flow only via the smallest and coarsest pores in a PTL.

The question that now arises is the connection between the permeation through the PTL and the mass transport losses of a PEM electrolyzer. At a first glance, it seems that the mass transport losses could be a function of the gas flow and the water flow. There is an energy expenditure necessary for the gas to flow through the PTL that needs to come from somewhere, and given that the gas has been evolved inside the electrode (instead of coming from a pressurized source), the only reasonable source of available energy has to be the electric energy feeding the electrolysis cell. Water, on the other hand, acts as a further impediment for the gas flow; thus, I expect that an increased water flow increases the mass transport losses. Another possible source of mass transport losses could be the water that flows from the flow field into the electrode: since the evolved gas flow is constantly draining the PTL pores of water in order to exit the electrolysis cell, the electrodes could be suffering from water

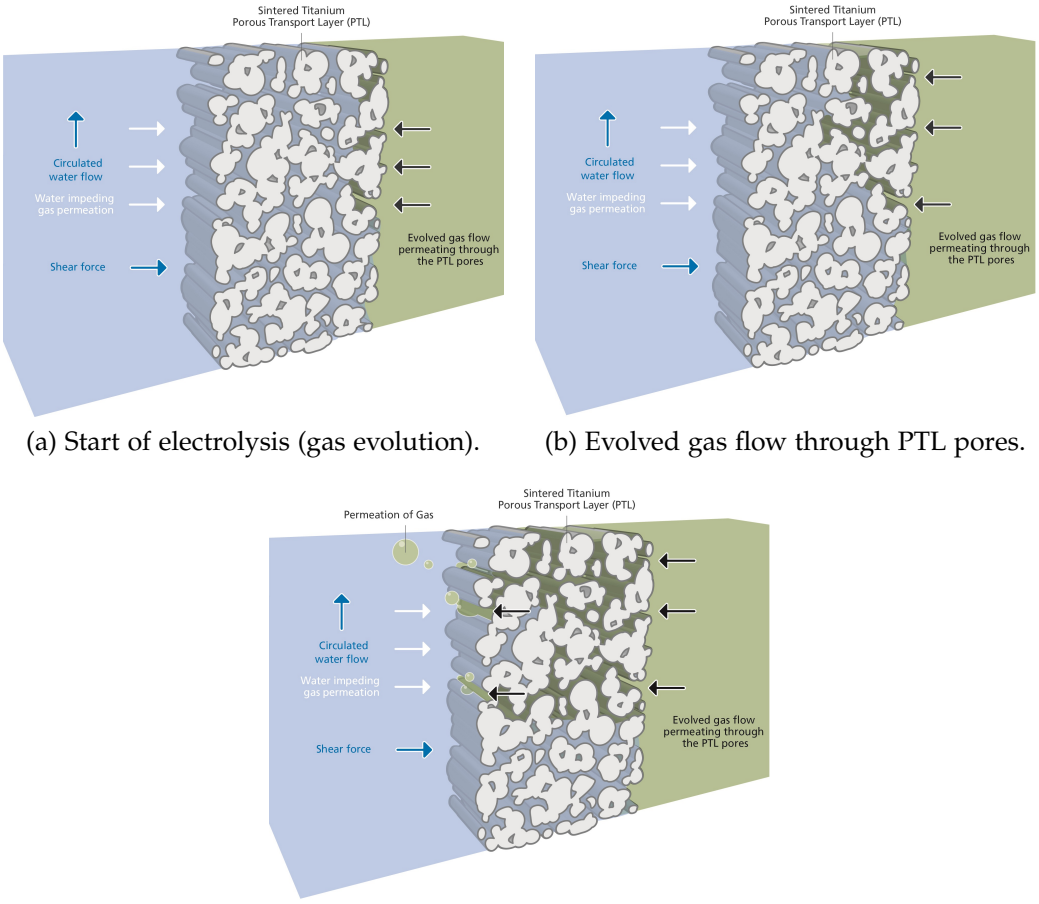

(a) Start of electrolysis (gas evolution).

(b) Evolved gas flow through PTL pores.

(c) Gas breakthrough to the flow channel.

Figure 4.7: Images showing the possible gas permeation mechanism through the PTL in a PEM electrolyzer, showcasing the effect of water flow exerting a shear force on the PTL pores. (Top left) Start of the gas evolution. (Top right) Evolved gas permeating through the PTL, displacing water in the pores. (Bottom) Breakthrough of the gas front flow through the pores that show favorable conditions for gas permeation.

starvation, which could cause an increased mass transport loss. I believe that the latter (water starvation) is less likely to be an important source of transport losses than the former (gas crossing the PTL), since the energy needed for water to flow toward the electrode would have to be delivered by the water pump, not to mention that a hydrophilic PTL would promote the water to flow through its pores. Moreover, the pores where it is energetically unfa-

vorable for the gas to permeate through (i.e., the longest pores) could be the pores delivering water from the flow fields to the electrodes. Figure 4.7 show a series of images conveying the gas permeation process in an operating PEM electrolyzer, based on the results depicted in this chapter.

4.4 CONCLUSION

In this chapter, I carried out gas permeation measurements in a sintered titanium PTL where I evaluated the effect of the in-plane water flow on gas that flows through the PTL pores (thereby simulating the operation of a PEM electrolyzer) to bring insight into the topic of mass transport through a PTL. I proposed that the transport of gases through a PTL does not obey a one- or two-phase flow regime but rather a permeation regime and that the problem of mass transport losses can be understood as a problem of a nonwetting fluid displacing a wetting fluid in a porous, hydrophilic medium. I introduced an energy balance to calculate the energy losses associated with the gas flow through pores and used Darcy's law and the Carman–Kozeny equation to calculate the apparent tortuosity of the PTL as a function of the water flow.

I found out that the pressure loss and the tortuosity are correlated to the in-plane water flow, which can be explained by a shear stress exerted by the water flow on the gas flow. I found a quadratic correlation between tortuosity and water flow, which means that this shear stress is related to the kinetic energy of water. Finally, I calculated the apparent tortuosity of the PTL as a one-phase flow of gas through the pores, and the calculations show that this transport mechanism is more energy demanding than permeability, further confirming that permeability is the main mass transport mechanism of gas through PTLs.

5

IMPEDANCE SPECTROSCOPY OF MASS TRANSPORT PHENOMENA

5.1 INTRODUCTION

As I argued in chapter 1 of this thesis, EIS is one of the most useful in situ tools to measure and differentiate the different sources of overpotential in a PEM electrolyzer, due to its simple operation and the extensive theoretical framework that relates EIS measurements to physical phenomena such as mass transport [9][48]. Nevertheless, EIS has been rather underutilized in the PEM electrolysis community as a tool to measure mass transport losses, where most of the results are rather qualitative rather than quantitative [76][86][92][78]. Building from the results from chapters 3 and 4, the mass transport losses in a PEM electrolyzers are likely to be related to water flow impeding the evolved gases from exiting the pores of the PTLs. Aside from exerting a shear force on the gases, water-related mass transport losses can also promote gas accumulation in the PTL pores that will, in turn, cause bubble shading on the active area. Moreover, according to Table 1.1, there is no clear understanding of how pressure affects the performance of PEM electrolyzers; it is possible that, for example, water with a higher pressure causes a larger energy drop on the evolved gases when they exit the PTL pores. In this chapter, I present measurements regarding the effect of water flow and pressure on the mass transport overpotential, and I show a model I derived to explain the obtained data, based on the theoretical framework of EIS.

5.2 MODELING

5.2.1 *EIS model*

I modeled the measured EIS using the modified Randles equivalent circuit depicted in Figure 5.1. The equivalent circuit used is substantially different from the typical equivalent circuit used to analyze EIS spectra from PEM electrolyzers (see [27][87]). The typical equivalent circuit consists of two Voigt elements (resistor and capacitor in parallel) connected in series, with the capacitor substituted by a constant-phase element (CPE) to account for inhomogeneities in the contact between electrolyte and electrode [48]. The two differences I am introducing to the analysis of the EIS spectra is the use of an ideal capacitor and the use of a finite diffusion element that replaces the second Voigt element. Given the relavitely high current density at which I operated the PEM electrolysis cell (1.5 A cm^{-2}), the dominant overpotentials are ohmic and mass transport losses; therefore, using a CPE instead of an ideal capacitor would not bring much more useful information about the MEA while simply adding an extra parameter to fit the data. Moreover, the estimation of the electrode capacitance is relevant for the mathematical model, and this capacitance follows more naturally from an ideal capacitor than from a CPE.

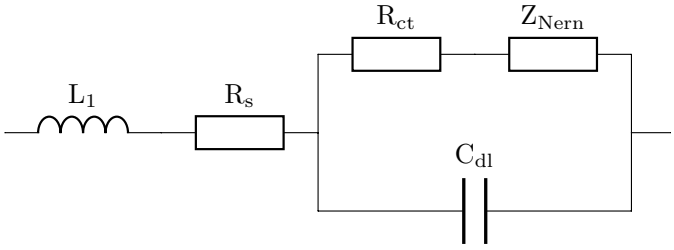

Figure 5.1: Modified Randles circuit used to fit the EIS spectra. I used the Nernst impedance instead of a second Voigt element to relate the low-frequency impedance to mass transport impedance.

The second feature of the equivalent circuit is the finite diffusion element. Voigt elements are typically used to represent charge transfer phenomena oc-

curring in electrodes [9][48], and it is generally understood that the capacitance measured corresponds to the interface between electrode and electrolyte, where the electronic and the ionic conductors come in contact. Kinetic effects are typically detected at relatively high frequencies [48]; therefore, it is unlikely that the low-frequency impedances at current densities larger than 1 A cm^{-2} are in fact kinetic in origin. As for the choice of mass transport impedance, there exist three main models in the EIS theory [48]: the semiinfinite diffusion impedance, which occurs when the reactant is supplied stoichiometrically; the finite diffusion impedance with a reflective boundary, which occurs when the transported species do not penetrate the electrolyte; and the finite diffusion impedance with a transmissive boundary (also known as Nernst impedance), which occurs when the transported species penetrates the electrolyte. The model for all three diffusion impedances is similar (Warburg impedance); the main difference lies in the boundary conditions for each of the three scenarios. Assuming that at low frequencies the measured impedance corresponds to mass transport effects, it follows that the Nernst impedance is a more suitable element to model the EIS spectra than using a second Voigt element. Mathematically, a second Voigt element with a CPE could in fact provide a better fit than the Nernst impedance, but this is attributable to the former having 3 parameters to fit instead of the 2 parameters from the latter model.

The general expression for the finite-length Warburg impedance (Nernst impedance) with a transmissive boundary is [48]

$$Z_{Nern} = \frac{RT}{z^2F^2D_{eff}^{0.5}C_gA_e2^{0.5}\omega^{0.5}} \tanh\left[\left(\frac{i\omega}{D_{eff}}l_e^2\right)^{0.5}\right](1-i) \tag{5.1}$$

where R is the universal gas constant, T is the system temperature, z is the number of moles of electrons transferred during either the HER or the OER reactions, F is Faraday's constant, D_{eff} is the effective gas diffusivity, C_g is the gas concentration in the water surrounding the electrode, A_e is the electrode area, ω is the frequency, i is the imaginary number, and l_e is the electrode thickness.

The apparent tortuosity (which I introduced in chapter 4) is a measurement of the energy losses associated with the mass transport in the PEM electrolysis cell, interpreted as a lengthened diffusion path of the evolved gases. The parameter D_{eff} is related to the tortuosity according to equation 5.2 [74]

$$D_{eff} = D_0 \frac{\epsilon_{ap}}{\tau_{ap}} \tag{5.2}$$

where D_0 is the gas diffusivity in a free medium, τ_{ap} is the apparent tortuosity of the electrode, and ϵ_{ap} is the electrode's apparent porosity. The porosity and the tortuosity are related according to Bruggeman's correlation [20]

$$\epsilon_{ap} = \frac{1}{\tau_{ap}^2} \tag{5.3}$$

The term A_e in equation 5.1 does not necessarily refer to the coated area of the membrane (25 cm²); it could also represent the actual interface between electrode and ionomer. The choice between the two areas in the model is a function of the expected magnitude of the diffusion path. I am assuming that the diffusion length of the evolved gases is equal for all active sites and that it spans beyond the electrode surface. This assumption implies that the term A_e will be equal to the coated electrode surface (25 cm²). Figure 5.10 displays a sensitivity analysis where I explore the aforementioned assumption and calculate the effect of the electrochemical area of the electrode (which carries the assumption that the diffusion length is equal to or shorter than the electrode thickness) on τ_{ap} (Figure 5.10). The electrochemical area can be estimated from the double layer capacitance

$$C_{dl} = {\epsilon_r}^{perm} {\epsilon_0}^{perm} \frac{A_e}{l_{dl}} \tag{5.4}$$

where ${\epsilon_r}^{perm}$ is the relative permittivity of the Nafion membrane, ${\epsilon_0}^{perm}$ is the vacuum electric permittivity, and l_{dl} is the double layer thickness, which can be calculated as

$$l_{dl} = d_w n_w \tag{5.5}$$

where d_w is the Lennard–Jones diameter of a water molecule and n_w is the number of water molecules that separate the double layer (membrane and electrode).

For the parameter ${\epsilon_r}^{perm}$, the relative medium permittivity (also known as the dielectric constant) of Nafion, I used a value of 20, which corresponds to the dielectric constant of Nafion when fully humid [73]. I assumed that the parameter l_{dl}, the distance between the double layer, should acquire a value equal to the number of water molecules that would fit within the outer Helmholtz layer; I assumed that there would be 2 water molecules (on average) that separate the electrode and the ionomer (one water molecule to solvate each plate of the double layer). I used a hard-sphere water diameter of 3.166 Å (calculated with an extended simple point charge model for water, see [11]).

I calculated the parameter D_0 of equation 5.2, the gas bulk (or free-medium) diffussivity in water, using the Wilke–Chang equation (which is an empirical modification of the Stokes–Einstein equation, see [14])

$$\frac{D_0 \mu_w}{T} = 9.32x10^{-6} Nm^{1.8} K^{-1} kg^{-0.5} mol^{-0.1} \frac{\left(\varphi_w M_w\right)^{0.5}}{{v_g}^{0.6}} \tag{5.6}$$

where μ_w is the water viscosity, φ_w is the association parameter of water as a solvent, M_w is the water molar mass, and v_g is the molar volume of each gas.

Fick's first law of diffusion and the mass conservation equations in a porous substrate are depicted as

$$J = -D_{eff} \frac{\partial C_g}{\partial \dot{x}} \tag{5.7}$$

$$\frac{\partial C_g}{\partial t} = -\frac{1}{\epsilon} \frac{\partial J}{\partial \dot{x}} \tag{5.8}$$

where J is the material flux of the evolved gases, $\dot{x}$ is position, and t is time.

Combining equations 5.1, 5.7, and 5.8, and incorporating equations 5.2, 5.3, and 5.6, leads to the following equation

$$Z_{Nern} = \frac{RT\tau_{ap}^{2.5}}{z^2 F^2 D_0^{0.5} C_g A_e 2^{0.5} \omega^{0.5}} \tanh\left[\left(\frac{i\omega\tau_{ap}}{D_0} l_e^2\right)^{0.5}\right](1-i) \tag{5.9}$$

All the parameters in equation 5.9 can be bundled together into two parameters

$$\sigma = \frac{RT\tau_{ap}^{2.5}}{z^2F^2D_0^{0.5}C_gA_e2^{0.5}} \tag{5.10}$$

$$k = \frac{D_0}{\tau_{ap}l_e^2} \tag{5.11}$$

The mass transport resistance, R_{mt}, is depicted in equation 5.12 as a function of the parameters σ and k [48]

$$R_{mt} = \frac{\sigma}{k^{0.5}} \tag{5.12}$$

Deriving an explicit expression for the tortuosity as a function of the EIS parameters σ and k (as well as the electrode properties) by solving equation 5.12 for τ_{ap} leads to

$$\tau_{ap} = \left(\frac{z^2F^2D_0C_gA_e2^{0.5}R_{mt}}{RTl_e}\right)^{0.33} \tag{5.13}$$

Equations 5.10, 5.11, and 5.12 can be combined to show the dependence of the mass transport overpotential, η_{mt}, with the electrode parameters (that can be indirectly measured with EIS)

$$\eta_{mt} = R_{mt}Aj \tag{5.14}$$

where η_{mt} is the mass transport overpotential, j is the current density, and A is the electrode coated surface.

5.2.2 *Mass transport model*

I estimated the gas concentration around their respective electrodes using the model derived by Vogt and Stephan [100][102]. Vogt and Stephan's mass transport model assumes that the mass transport of gas evolving electrodes consists of two main mass fluxes: a mass flux of evolved gas from the active site to the

surrounding water, and a mass flux of dissolved gas from the surrounding water to the bubbles, which then detach (or coalesce and then detach) and leave the electrode.

Equation 5.15 calculates the concentration around the electrode (assuming that the concentration far from the electrode is much lower than the concentration in its vicinity) [100]

$$\frac{C_g}{C_{g,sat}} = 1 - Sh_1 - \frac{2}{3} f_g \left(1 - Sh_1^{1.5}\right) \tag{5.15}$$

where $C_{g,sat}$ is the gas concentration at saturation conditions, Sh_1 is the Sherwood number of mass transport between the catalytically active sites and the bulk of the surrounding liquid (which will be discuss later), and f_g is the gas evolution efficiency (defined as the fraction of evolved gas that exits the cell in gas phase).

The parameter Sh_1 can be estimated using equation 5.16 [102]

$$Sh_1 = \frac{2}{10^{0.5}} Re_g^{0.5} Sc^{0.5} \left(1 - \frac{8^{0.5}}{3} \theta_{elec}^{0.5}\right) \tag{5.16}$$

where Re_g is the Reynolds number of the gas, Sc is the Schmidt number, and θ_{elec} is the electrode coverage fraction by the gas bubbles. It is important to mention that the exponent of the Schmidt number on equation 5.16 was originally set as 0.34; this exponent is relatively ill-defined and typically lies between 0.34 and 0.5 [102]. The choice of exponent will be related to the mechanism that dominates the mass transport, with several models in the literature choosing a value of 0.5 [102]. In this case, I found that a coefficient of the Schmidt number of 0.5 on equation 5.16 better represented the obtained data.

The Reynolds number of the gas phase, Re_g, can be estimated using equation 5.17 [102]

$$Re_g = f_g \frac{j}{zF} \frac{RT}{P} \left(1 - \frac{P_w}{P}\right)^{-1} \frac{d_b}{\nu_w} \tag{5.17}$$

where P is the electrode pressure, P_w is the water vapor pressure, d_b is the bubble diameter, and ν_w is the water kinematic viscosity. I used Antoine's equation to estimate the water vapor pressure, shown in equation 5.18 [75]

$$\log_{10}\left(\frac{P_w}{1bar}\right) = 5.11564 - \frac{1687.537K}{T - 42.98K} \tag{5.18}$$

The parameter f_g, the gas evolution efficiency, calculates the fraction of the evolved gas that leaves the electrode in gas-phase (the rest of the gas would be carried away dissolved in water) [100]. It is a function of θ_{elec}, the fractional electrode coverage by bubbles [100]; both parameters are calculated by equations 3.17 [102] and 3.18 [101], respectively for f_g and θ_{elec}.

The bubble detachment diameter, d_b in equation 5.17, will be lower than the detachment diameter of a bubble with no electric current flowing to the electrode; this phenomenon is caused by a change in the electrode wettability when it is under electric potential [101]. Vogt and Stephan propose the following correlation to calculate the detachment diameter as a function of current density [101][102]

$$d_b = d_{b,0}\left[1 + 0.15\left(\frac{j}{Am^{-2}}\right)\right]^{-0.5} \tag{5.19}$$

where $d_{b,0}$ is the bubble detachment diameter on an electrode with no current density passing through it. Therefore, the bubble detachment diameter is a function of current density; it is, however, a function of the pressure as well, since larger pressures will compress the evolved bubbles. Equation 5.20 shows the correction of the detachment diameter with respect to pressure, according to Boyle's law

$$d_{b,0}(p) = d_{b,0}\left(\frac{1bar}{p}\right)^{0.33} \tag{5.20}$$

The Schmidt number is defined as

$$Sc = \frac{\nu_w}{D_{eff}} \tag{5.21}$$

Combining equation 5.21 with 5.2 and 5.3, the Schmidt number can be expressed as a function of tortuosity

$$Sc = \frac{\nu_w \tau_{ap}^3}{D_0} \tag{5.22}$$

To estimate the saturation gas concentration, I used Henry's law. To estimate Henry's coefficient at a temperature T (H_T), I utilized the correlation and data reported by Sander [79]

$$H_T = H_{298K} \exp\left[\frac{-\Delta H}{R}\left(\frac{1}{T} - \frac{1}{298K}\right)\right] \tag{5.23}$$

where H_{298K} is the Henry's coefficient at 298K and ΔH is the enthalpy of dissolution. Henry's law states the relationship between the saturation gas concentration and the system pressure

$$C_{g,sat} = H_T\,(P - P_w) \tag{5.24}$$

The parameters to calculate the Henry's coefficient (equation 5.23) for O_2 and H_2 are displayed in Table 5.1.

To calculate the tortuosity from the fitted EIS spectra (based on the modified Randles circuit depicted in Figure 5.1), I solved the following system of equations:

$$\tau_{ap} = \left(\frac{z^2 F^2 D_0 C_g A_e R_{mt}}{RTl_e}\right)^{0.33} \text{(eq. 5.13)}$$

$$\frac{C_g}{C_{g,sat}} = 1 - Sh_1 - \frac{2}{3} f_g \left(1 - Sh_1^{1.5}\right) \text{(eq. 5.15)}$$

$$Sh_1 = \frac{2}{10^{0.5}} Re_g^{0.5} Sc^{0.5} \left(1 - \frac{8^{0.5}}{3}\theta_{elec}^{0.5}\right) \text{(eq. 5.16)}$$

$$Sc = \frac{\nu_w \tau_{ap}^3}{D_0} \text{(eq. 5.22)}$$

5.2.3 *Mass transport overpotential*

To show a more tangible result of the model, I am proposing an equation to calculate the mass transport overpotential, η_{mt}, on the lines of what has been

previously proposed [17][60][71][28]. There are three mathematical constraints an equation for η_{mt} should abide by

$$\eta_{mt} \rightarrow \begin{cases} 0 & \text{if } j \ll j_{lim} \\ \nexists & \text{if } j \geq j_{lim} \\ \infty & \text{if } j \approx j_{lim} \end{cases} \tag{5.25}$$

where j_{lim} is the limiting current density, the current density at which the mass transport overpotential approaches infinity and the system is impeded from producing any more gas. The parameter j_{lim} would theoretically be a function of the electrode (and/or PTL) transport properties and possibly thermodynamic properties as well. I propose the following equation to model the mass transport overpotential

$$\eta_{mt} = \frac{RT}{zF} \ln\left(\frac{1}{1 - \frac{j}{j_{lim}}}\right) \tag{5.26}$$

Equation 5.26 complies with the constraints depicted in equation 5.25. Moreover, equation 5.26 is only characterized by a single parameter (j_{lim}), thus overparametrization is avoided; overparametrization can yield good fits to experimental data but little relation to the underlying physical phenomena. I am confident that equation 5.26 can adequately model the mass transport overpotential, from which fruitful conclusions can be drawn. The question that remains is how to calculate j_{lim} as a function of kinetic, thermodynamic of electrode design variables. Combining equations 5.14 and 5.26 and solving for j_{lim}, leads to the following equation

$$j_{lim} = \frac{j}{1 - \exp\left(-\beta_{lim} j\right)} \tag{5.27}$$

where the parameter β_{lim} is defined as

$$\beta_{lim} = \frac{\tau_{ap}^4 l_e A}{zFD_0 C_g A_e} \tag{5.28}$$

Equation 5.27 shows that j_{lim} is a function of both the current density and the electrode properties, namely thickness and double layer surface; j_{lim} appears to

be a function of gas properties namely, diffusivity and concentration near the electrode. An interesting feature of equation 5.27 is that j_{lim} appears to depend on the tortuosity, which can be either related to the porous structure of the electrode (i.e. intrinsic tortuosity), or to the operating conditions.

Table 5.1 shows the parameters used with the model described in this section. The parameters for calcualting the diffusion coefficient were obtained from [14][104][75]; the electrode thickness was obtained from [57].

5.3 RESULTS AND DISCUSSION

5.3.1 *V(I) curves and EIS spectra*

Figures 5.2 and 5.3 show the measured V(I) curves as a function of water flow and pressure, respectively. Whereas the anode pressure tests show an almost complete overlapping of the curves (indicating that there is no discernible trend), the other three tests are considerably different. Both water flow tests show an increase in the overpotential at higher current densities when the flow rate increased, the cathode water flow test showing a clearer trend. There is an overlap of the different V(I) cuves at low current density (where the kinetic overpotential dominates), which is an indication that the water flow increase is affecting asymmetrically the potential at high current densities (where the mass transport overpotential dominates). We do not see a curve distinctive of high mass transport overpotentials [71][28][52] but rather a slight increase that is consistent with the increase in the water flow.

The cathode pressure seems to have the strongest effect on the total overpotential: Figure 5.3 shows that the increase in cathode pressure leads to parallel V(I) curves with an increasing overpotential that is uniform across all current densities. This could be an indication of a change in the thermo-neutral potential of the cell, which should be in principle only a function of the system temperature (due to the change in the thermo-neutral voltage being a function of the change of reaction entropy); this effect is outside of the scope of this chap-

Parameter		Value	Unit
General parameters			
T		65	°C
A		25	cm^2
z	O_2	4	–
	H_2	2	–
ν_w		$4.44x10^{-7}$	$m^2\ s^{-1}$
j		1.5	$A\ cm^{-2}$
Diffusion coefficient calculation			
μ_w		$4.3x10^{-4}$	Pa s
φ_w		2.6	–
M_w		0.018	$kg\ mol^{-1}$
v_g	O_2	$2.56x10^{-5}$	$m^3\ g^{-1}\ mol^{-1}$
	H_2	$1.43x10^{-5}$	$m^3\ g^{-1}\ mol^{-1}$
Henry coefficient			
H_{298K}	O_2	$1.2x10^{-5}$	$mol\ m^{-3}\ Pa^{-1}$
	H_2	$7.8x10^{-6}$	$mol\ m^{-3}\ Pa^{-1}$
$\frac{\Delta H}{R}$	O_2	1700	K
	H_2	530	K
Double layer thickness			
d_w		$3.166x10^{-10}$	m
${\epsilon_r}^{perm}$		20	–
Model-specific parameters			
$d_{b,0}$		50	µm
l_e		7	µm
n_w		2	–

Table 5.1: Parameters used in this chapter.

ter. Besides the apparent change in the thermo-neutral potential, the cathode pressure seems to have an effect on the overpotential at high current density; thus, the cathode pressure is increasing the mass transport losses. Neither V(I)

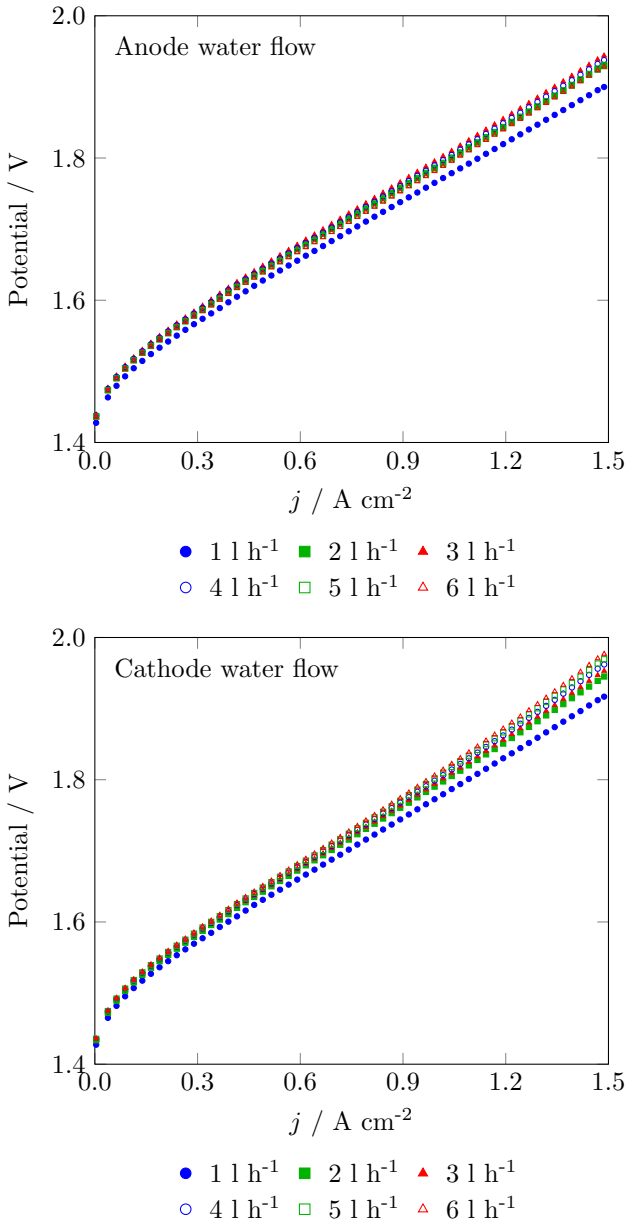

Figure 5.2: V(I) curves as a function of water flow for anode (top) and cathode (bottom).

curve shows a change in the low current density or the mid current density regions, indicating that neither parameter affects the kinetics of the system or the ionic resistance (which dominates the electric resistance) of the cell.

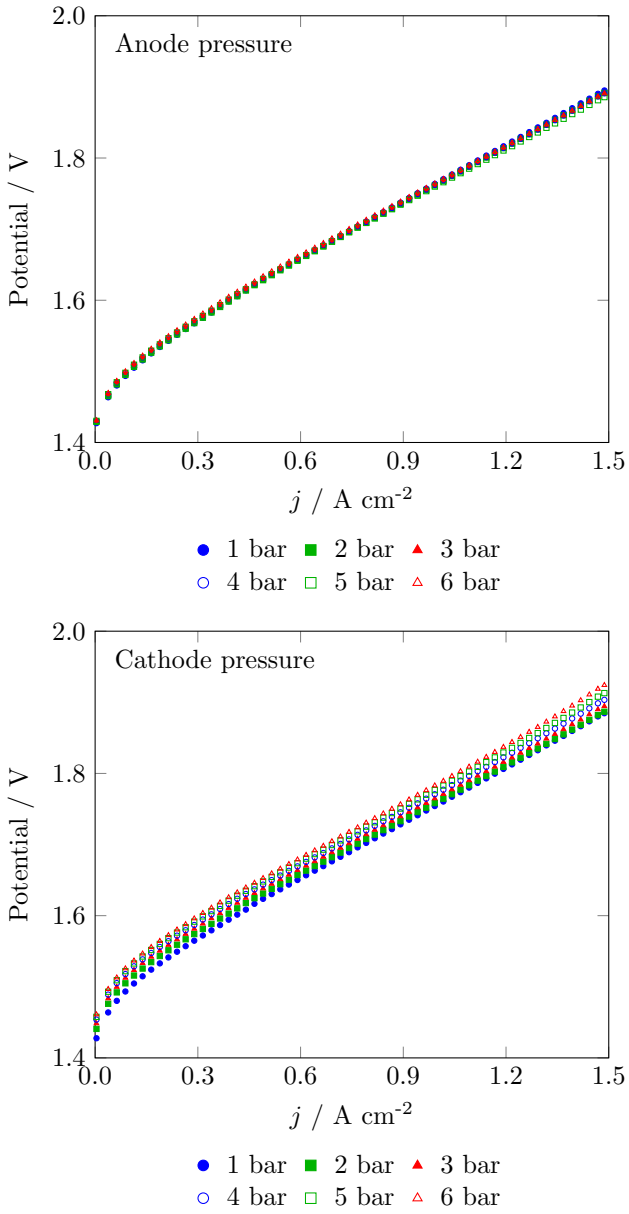

Figure 5.3: V(I) curves as a function of pressure for anode (top) and cathode (bottom).

Figures 5.4 and 5.5 show the measured EIS spectra at 1.5 A cm^{-2} as a function of water flow and pressure, respectively. I subtracted the high-frequency resistance from each spectrum to have them all intersect at the origin and make the visual comparison of the resulting semicircles easier. In the Nyquist diagrams

we can observe two distinct semicircles, attributable to the kinetic resistance (the leftmost semicircle) and the mass transport resistance (the rightmost semicircle). The effect of each half-cell reaction on the obtained spectra cannot be visually distinguished; therefore, I decided to lump together both reactions in a single Voigt element on the equivalent circuit (Figure 5.1) used to fit the EIS spectra. We can see in Figures 5.4 and 5.5 that all tests but the anode pressure test show an increasingly large second semicircle (attributable to the mass transport kinetics) with the respective increases in the water flow or pressure. In magnitude, the cathode water flow seems to cause the highest mass transport resistance (measurable as the semcircle diameter), with the cathode pressure coming in second place. The high frequency semicircle appears unaffected by water flow or pressure, which was expected given that the Butler–Volmer equation (that calculates kinetic losses) is only a function of temperature.

Figure 5.6 shows the high frequency resistance (HFR) as a function of water flow and pressure. The HFRs depicted in Figure 5.6 correspond to the ohmic resistance of the PEM electrolyzer. We observe an increase in the HFR for all measurements with increasing water flow rate and with increasing pressure, save for the anode water flow test (which shows first an increase and, for water flows larger than 4 l h^{-1}, a decrease of the HFR). This phenomenon could be an indication that the increase in pressure or water flow affects the humidity of the membrane, the electrodes, or the interfacial area betwen membrane and electrode. However, the changes in ohmic resistance are small: the difference between the lowest and the highest HFR values is 10% for the cathode water flow test and 5% for the anode and cathode pressure tests. These results could imply that the humidity of the PEM electrolyzer might not always be at its maximum point (since the HFR is inversely proportional to humidity, see [90]), which is counterintuitive considering that liquid water flows to the cell on a constant basis. I can argue that liquid water does not necessarily flood the Nafion™ N115 membrane at all times, due to gas evolving and displacing the water that surrounds the electrode. The electro-osmotic drag can also be affected by the gas evolution on the electrodes; Medina and Santarelli reported

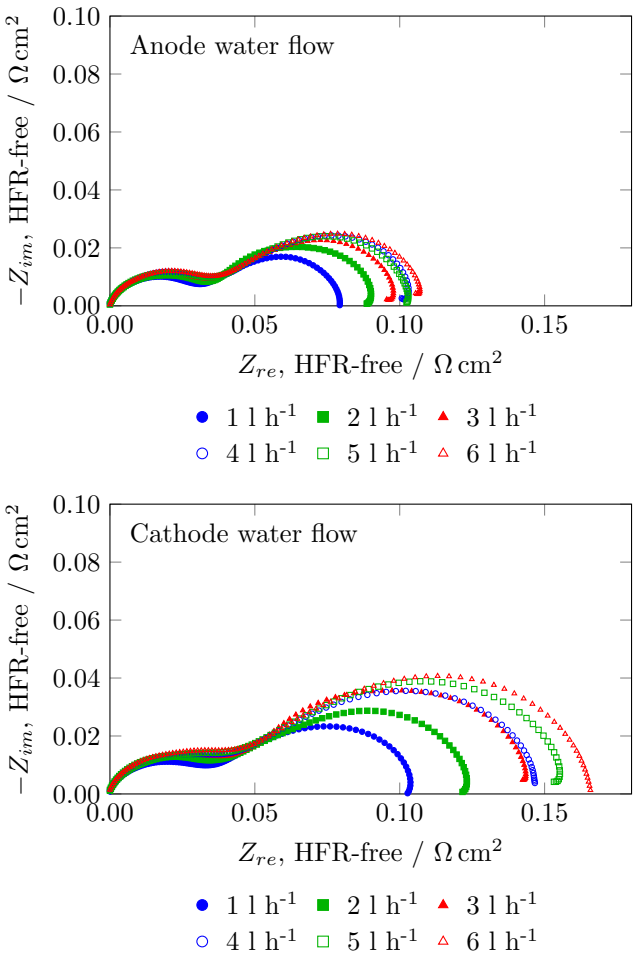

Figure 5.4: EIS spectra (measured at 1.5 A cm^{-2}, subtracting the High-Frequency Resistance, HFR) as a function of water flow for anode (top) and cathode (bottom).

that the electro-osmotic drag decreases with increasing current density, and this could affect the water content of the membrane enough to cause a HFR increase of up to 10% [63]. A third possibility is a changing contact area between membrane and electrodes due to forces induced by water flow and pressure changes. A fourth possibility could be a moderate temperature variation due to changes in the operating conditions. A fifth possibility can also be the increase in the cell potential due to pressure, according to the Nernst equation, although this effect should only be a function of pressure; therefore, water flow

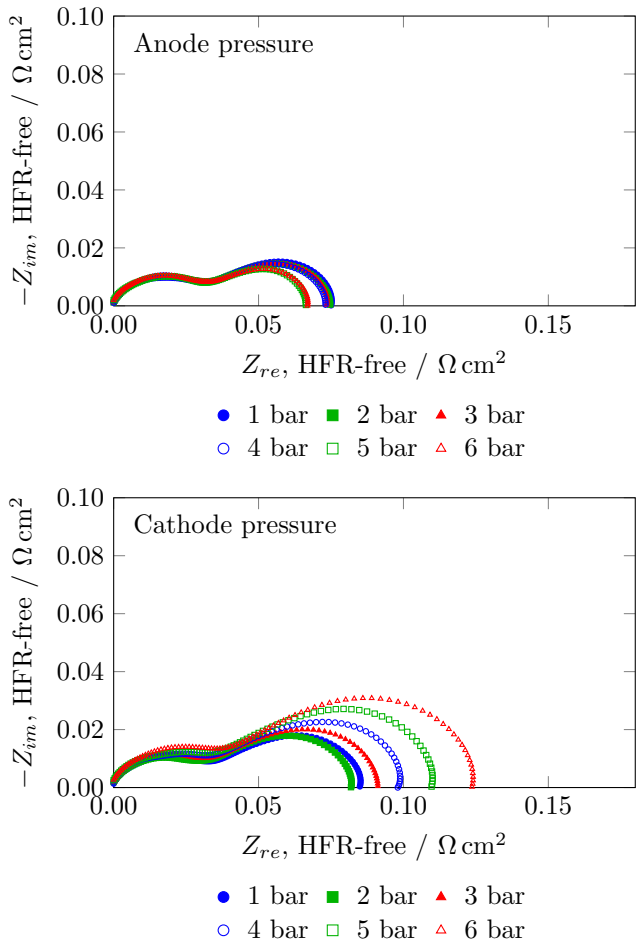

Figure 5.5: EIS spectra (measured at 1.5 A cm^{-2}, subtracting the HFR) as a function of pressure for anode (top) and cathode (bottom).

should not affect the reversible cell potential, as can be seen in the cathode water flow test (filled squares in Figure 5.6). Presently I cannot exclude any of these possibilities.

The main conclusion to draw from the experimental data is that there is indeed a relationship between mass transport overpotential and water flow and pressure; to explain such relationship, I am proposing to use the electrode tortuosity as the main parameter that controls the mass transport overpotential. I introduced the concept of tortuosity in chapter 4 4.28. I defined the tortuosity as the increase of the effective diffusion path between the catalytically active

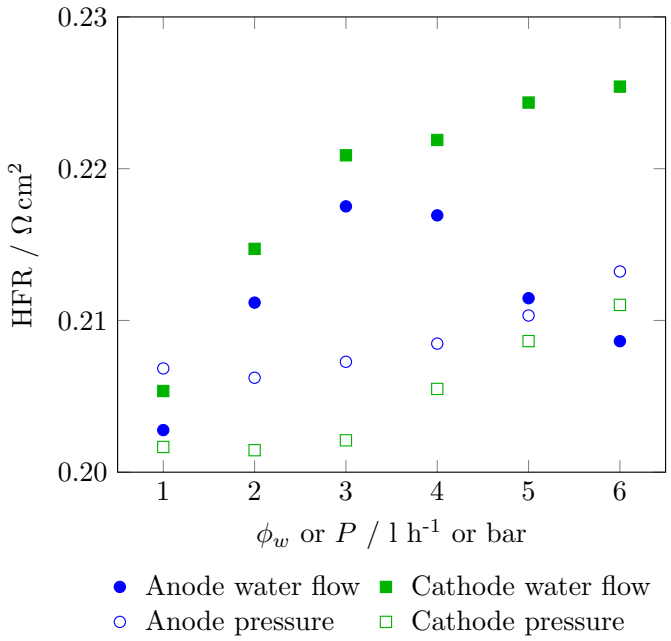

Figure 5.6: HFR of the EIS spectra, for anode (blue circles) and cathode (green circles), as a function of water flow (top) and pressure (bottom).

site and the bubble nucleation site. There are two kinds of tortuosity that we must distinguish: the intrinsic tortuosity and the apparent tortuosity. The intrinsic tortuosity is related to the morphology of the electrode (in particular to the electrode porosity according to Bruggeman's correlation, equation 5.3). Changes done to the intrinsic tortuosity will necessarily be irreversible and it is unlikely that either water flow or pressure affect the intrinsic tortuosity. Apparent tortuosity, on the other hand, is defined as the temporary (and reversible) increase in the mass transport losses and it will not cause a change of the electrode morphology (at least in the short-term future). I can express the apparent tortuosity as a function of the intrinsic tortuosity

$$\tau_{ap} = \tau_{int} k_{\tau}^{ex} \tag{5.29}$$

where τ_{int} is the intrinsic tortuosity and k_{τ}^{ex} is a coefficient that quantifies the excess tortuosity i.e., the increase of the measured tortuosity; changes in k_{τ}^{ex} are going to be caused by changes in the operating conditions (water flow and/or pressure).

If the operating conditions are not impeding the mass transport inside the PEM electrolyzer whatsoever but the PTL is nevertheless porous, the apparent porosity would be equal to the intrinsic tortuosity; thus, the value of k_{τ}^{ex} would be 1. An increase in the measured (apparent) tortuosity due to any changes in the experimental conditions need not be related to morphology changes of the PTL but rather to mass transport impediments caused by pressure or water flow changes; in such cases, the value of the parameter k_{τ}^{ex} would be larger than 1.

5.3.2 *Tortuosity and mass transport overpotential*

Figure 5.7 shows the calculated tortuosities (circles) and mass transport overpotentials (squares). All four tested operating parameters show a tortuosity that trends upwards, meaning that there is a correlation between increasing the water flow or pressure and an increase in the diffusion path for the evolved gas. The behavior of the mass transport overpotential correlates with the tortuosity except for the anode pressure, where we see an actual decrease in the mass transport overpotential (consistent with the data displayed in Figures 5.3 and 5.5, top). I can argue that there are several parameters that affect the mass transport overpotential, so that the increase in apparent tortuosity can be counteracted with the change in another parameter that ultimately caused the decrease of the mass transport overpotential. The parameter β_{lim} (equation 5.27) is a function of design parameters (electrode thickness, coated surface) but also a function of operating parameters (tortuosity and gas concentration). Generally speaking, the system of equations depicted on this chapter has two unknowns (tortuosity, τ_{ap} and gas concentration, C_g, which are interdependent as well) and one measurement to calculate them both (EIS); a decreasing mass transport overpotential can be due to both parameters changing at different rates (Figure 5.7).

To calculate the apparent tortuosity (Figure 5.8), I assumed that the tortuosity calculated at 1 l h^{-1} or 1 bar, corresponds to the intrinsic tortuosity of the

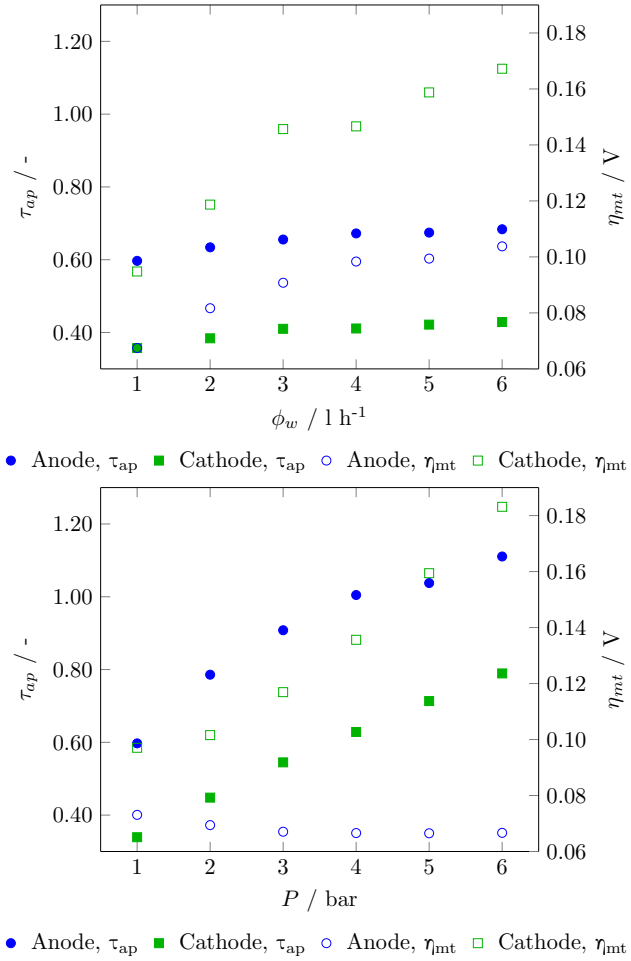

Figure 5.7: Tortuosity (filled markers, left axis) as a function of water flow (top) and pressure (bottom). Mass transport overpotential (hollow markers, right axis) calculated with equation 5.14, as a function of water flow (top) and pressure (bottom).

samples. The intrinsic tortuosities I calculated (Figure 5.7) at 1 l h^{-1} or 1 bar lie between 2.13 and 2.98; these values correspond to porosities of, respectively, 0.22 and 0.11 (using equation 5.3). Figure 5.8 shows the calculated apparent tortuosities, dividing each tortuosity curve in Figure 5.8 by the respective intrinsic tortuosity. We can notice that pressure increases lead to higher tortuosities (which does not necessarily translate to a higher mass transport overpotential, as I argued earlier), and that the cathode shows higher tortuosities than the anode at all studied values of water flow and pressure. All four curves in

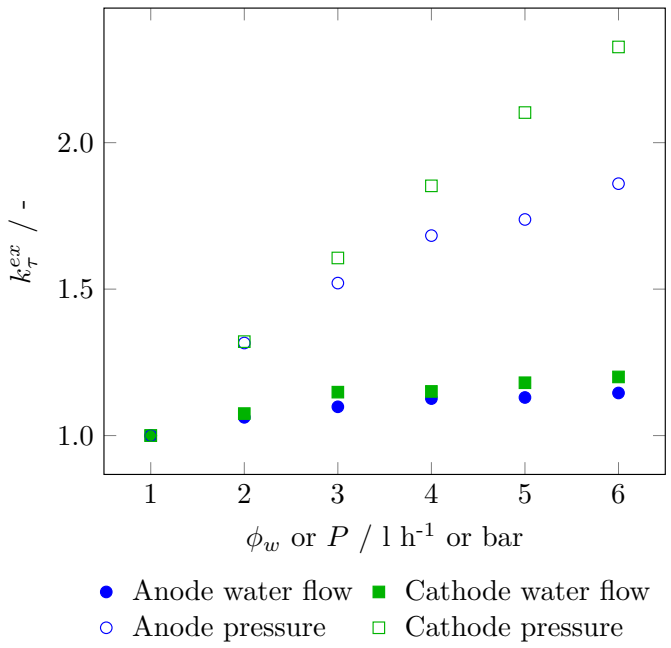

Figure 5.8: Apparent tortuosity (equation 5.29) as a function of water flow and pressure for both electrodes, calculated using data from Figure 5.7 and applying equation 5.29.

Figure 5.8 exhibit the same upward trend, although they all tend to reach an asymptote (the water flow tests appear to have reached a plateau while the pressure tests are likely to keep increasing). Since the PTL used is thought to have the optimal pore sizes to minimize transport losses [35], I expect the mass transport overpotential to be a function solely of the electrode; however, the results depicted in chapter 4 indicate that the PTL can play a significant role in determining the mass transport losses.

The main question that arises is, how does tortuosity exactly affect mass transport? Vogt and Stephan argue that the mass transport in gas-evolving electrodes is divided in two steps: transport from the active sites to the water that surrounds them (characterized by Sh_1, see equation 5.16), and transport from the water around the active sites to the evolving bubble (characterized by

a second Sherwood number, which we can call Sh_2) [100][102]. The relationship between both Sherwood numbers is [102]

$$\frac{Sh_2}{Sh_1} = 1 + \theta_{elec} \tag{5.30}$$

According to equation 5.30, Sh_2 will always be larger than Sh_1, considering that θ_{elec}, the fraction of the electrode covered by bubbles, is a number between 0 and 1. What equation 5.30 implies is that the mass transport between the active sites and the surrounding water is the limiting mass transport step; this statement is within reason due to the gas diffusing in a liquid medium. In this case, tortuosity can be understood as the lengthening of the diffusion path of the evolved gases. Nevertheless, tortuosity is not the only parameter controlling the mass transport between active sites and surrounding liquid; equation 5.28 shows that the electrode thickness, l_e, and the electrode surface, A_e, also play a critical role in the mass transport overpotential. The electrode thickness affects the mass transport in a straightforward manner: a thinner electrode allows for a shorter path for the evolved gases to diffuse to the surrounding water (assuming a constant electrode porosity); this does not necessarily mean that electrode thickness and porosity can independently be controlled during coating or drying of the catalyst ink. The electrode surface plays an opposite role as the thickness: an electrode with higher contact between the catalyst and the electrolyte will have more active sites; thus, effectively increasing the rate of gas production per unit area of coated surface.

An increase of the tortuosity with respect to the cathode pressure can be understood in terms of the Reynolds number of the gas, Re_g (see equation 5.17). An increased gas partial pressure will cause a lower Reynolds number, which subsequently causes a decrease in the Sherwood number (equation 5.16) as well as a decrease in the bubble detachment diameter (equation 5.20). I calculated values of the Sherwood number, Sh_1, between 0.65 (at lower water flow rates/pressures) and 0.35 (at higher water flow rates/pressures) meaning that the gas transport will always be dominated by diffusion rather than convection. At higher water flow and pressure values, a decreased Sherwood number

	6 l h^{-1}		6 bar	
	Anode	Cathode	Anode	Cathode
η_{ac} / V	0.10	0.10	0.10	0.09
η_{ohm} / V	0.32	0.33	0.31	0.31
η_{mt} / V	0.10	0.17	0.07	0.18

Table 5.2: Activation, ohmic and mass transport overpotentials of tests carried out at 6 l h^{-1} and 6 bar and 1.5 A cm^{-2}, calculated using the measured V(I) and EIS spectra (Figures 5.2, 5.3, 5.4 and 5.5).

causes gas to undergo a slower mass transport therefore causing an apparent increase in the diffusion path, given that the gases' destination (the gas bubble) is smaller due to a high current density and a high pressure, see equations 5.19 and 5.20. A strategy to counteract the effect of pressure on the tortuosity (or at least to alleviate it) can include increasing the hydrophobicity of the electrode (I measured the contact angle of the anode to be 76° 3.1) to force bubbles to grow bigger before detaching, keeping the diffusion path short, although larger bubbles will likely cause water starvation to the active area (bubble shading) and a subsequent increase in the mass transport losses. Optimization of the electrode hydrophobicity is a key parameter in controlling the mass transport losses.

Table 5.2 shows the contribution breakdown of each overpotential to the total system voltage at 1.5 A cm^{-2} and 6 l h^{-1} and 6 bar (the points with the largest mass transport overpotentials, see Figures 5.4 and 5.5). Figure 5.9 depicts a more detailed contribution breakdown analysis. I estimated the activation overpotential directly from the V(I) curves (total system voltage at 0.1 A cm^{-2}). I used the values for the ohmic and mass transport overpotential that I obtained with fitting the EIS model. We can observe in Table 5.2 that the ohmic overpotential dominates the operation overpotentials and that, in the anode water flow and pressure cases, the mass-transport and activation overpotentials have similar values at 1.5 A cm^{-2}.

The ohmic resistance has the largest contribution to the total overpotential and we can spot a slight pressure dependence, although it is not really significant (see Figure 5.6, bottom). Causes of the pressure effect on the ohmic overpotential could include a worsened contact between MEA and PTL due to mechanical differences of both materials as well as a decreased electro-osmotic drag coefficient (albeit Medina and Santarelli actually measured an increase in the electro-osmotic drag with respect to pressure, see [63]). There was a consistently larger effect of water flow and pressure on the cathode mass transport overpotentials as compared with the anode. I could attribute the effect to the amount of evolved gas (the electrolysis cell produces twice as much H_2 as O_2). Another possibility is that the saturation concentration of H_2 is lower than of O_2 (considering that both Henry coefficients are smaller for H_2, see Table 5.1); therefore, the cathode could have a smaller concentration gradient to drive the mass transport.

Another point to mention is the fact that measuring and modeling mass transport losses at electrode level does not necessarily mean that the losses actually occur at the electrode; the PTL could actually play a fundamental role when it comes to mass transport losses (as I discussed in the previous chapter). I used a sintered Ti PTL for the cathode, where the usual PTLs are Sigracet (carbon paper) layers. The fact that I find larger mass transport losses in the cathode side could be symptomatic of the PTL used (likely to be unfavorable to mass transport due to the small pore size and large thickness) rather than being caused by an unfavorable electrode structure (for mass transport). One more possibility is that the measured mass transport losses were actually caused by mass transport through the PTLs. A consequence of these losses at the PTL level in the mathematical model is that now the bubble evolving sites are more likely to be close to the pores of the PTL, if the bubbles are not in fact evolving underneath them. Therefore, we can look at the PTL pore distribution and pore size as potentially optimizable parameters for the mass transport overpotential.

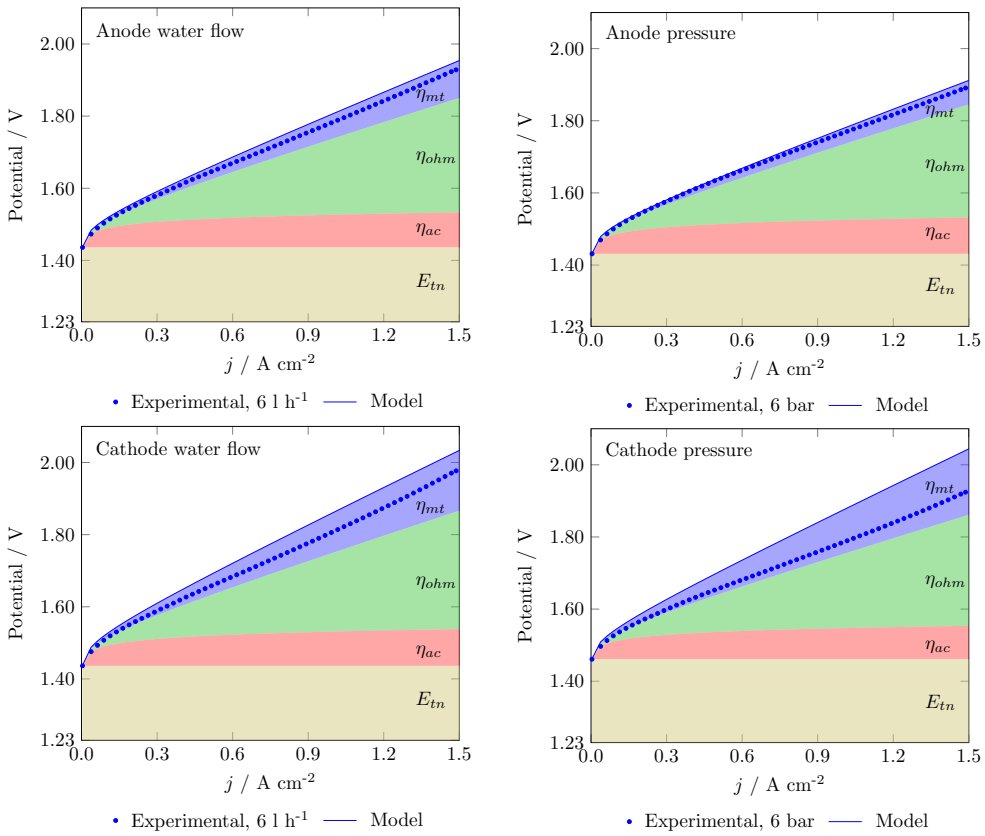

Figure 5.9: Contributions to the total reaction overpotential for anode (top) and cathode (bottom) for 6 l h^{-1} (left) and 6 bar (right). The dotted line is the averaged V(I) curve measured (Figure 5.2), and the solid line corresponds to the parameters obtained with the averaged EIS spectra (see Figure 5.4) using the equivalent circuit depicted in Figure 5.1, including the mass transport overpotential equation (equation 5.26).

5.3.3 *Sensitivity analysis*

As I mentioned in the modeling section, the term A_e in equation 5.1 does not necessarily refer to the coated area of the membrane (25 cm^2). An increase in the apparent tortuosity of the diffusion path for both evolved gases means that the dominant step in the mass transport occurs increasingly far from the active sites i.e., at higher pressures, the evolved gases will diffuse through paths that exceed the electrode thickness (see Figure 5.8). This situation led me to use the geometric (coated) area of the electrode in the tortuosity calculations. At

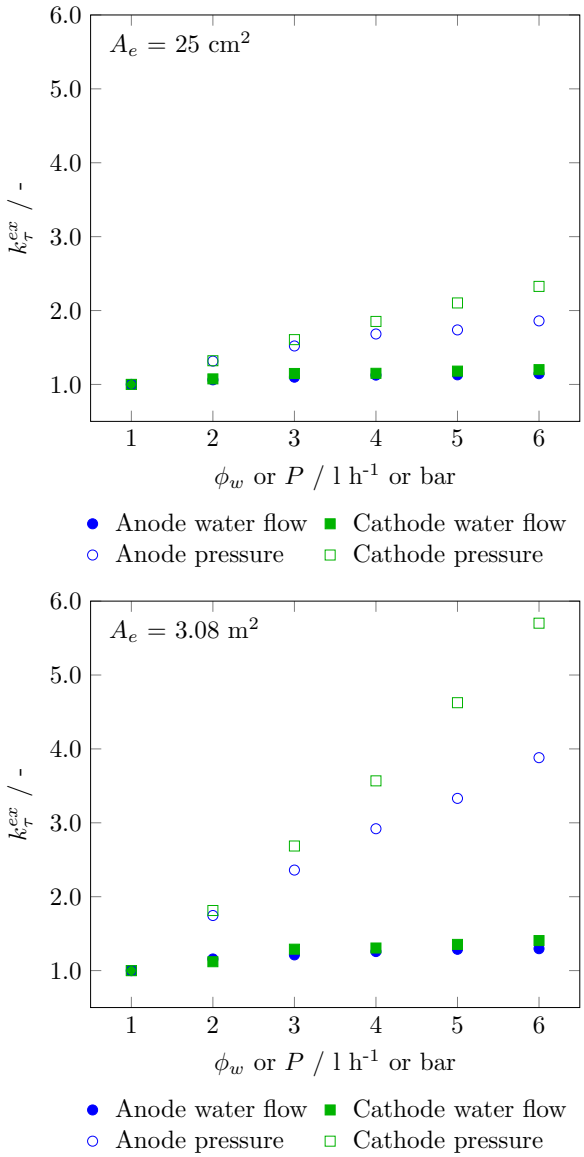

Figure 5.10: Excess tortuosity parameter (equation 5.29) as a function of water flow and pressure for both electrodes, when the parameter A_e is equal to the geometric area of the electrode (A_e = 25 cm²) (top), and to the electrochemical area of the electrode (A_e = 3.08 m²) (bottom).

low pressures and all studied water flows, however, the excess tortuosity parameter (equation 5.29) is relatively close to 1, which means that the previously

described assumption may not hold and I need to calculate the tortuosity using the electrochemical area of the electrode.

Figure 5.10 shows the sensitivity of the excess tortuosity parameter to the area. I estimated the electrochemical electrode area using equation 5.4 and the capacitance data measured with EIS (Table A.1) and obtained an area of 3.08 m^2, three orders of magnitude larger than the geometric area. I solved the system of equations depicted in the modeling section using the electrochemical area instead of the geometric area. Using the electrochemical area of the electrode resulted in a substantial increase in the apparent tortuosity at higher pressures. Higher tortuosities mean that the diffusion path of the evolved gases will be lengthened; therefore, at higher tortuosities the working surface for diffusion will become the geometric area of the electrode instead of the electrochemical area. The apparent tortuosity caused by the increase in the water flow was not affected by the choice of area, which was expected considering that the apparent tortuosity is a function of $A_e^{0.33}$ (equation 5.13) and that τ_{ap} is in general more sensitive to pressure than to water flow (see Figure 5.7).

5.4 CONCLUSION

In this chapter, I showcased an alternative methodology to measure and model the mass transport losses in PEM electrolyzers. I presented a model derived directly from the finite diffusion EIS model (the mass transport impedance) and combined it with Vogt and Stephan's mass transport model in gas-evolving electrodes. I defined the electrode tortuosity as the primary parameter governing the mass transport in PEM electrolyzers. Additionally, I proposed an equation to model mass transport losses as a function of a single parameter namely, the limiting current density, which I found to depend on parameters included in the mass transport impedance, such as tortuosity, electrode thickness, double layer surface and gas concentration.

I applied the proposed modeling framework to measure the effect of water flow and pressure on the mass transport losses. I found a consistent correla-

tion between increasing water flow and pressure, and increased mass transport overpotential, visible on EIS spectra performed at 1.5 A cm^{-2}. The cathode of the PEM electrolyzer appeared to be more sensitive to water flow and pressure, where we saw that a small change in the tortuosity leads to a more substantial change in the mass transport overpotential than in the anode. I measured a more considerable increase of the tortuosity with pressure than with water flow, which is an indication that pressure effects a more substantial change in the diffusion path of the evolved gases than the water flow; nevertheless, water flow plays a significant role in determining the mass transport losses in PEM electrolyzers.

Part III

FINAL REMARKS

General conclusions and future work proposed for the topic of mass transport in PEM electrolyzers.

6

FINAL REMARKS

6.1 GENERAL CONCLUSIONS

Chapter 3 of this thesis described the characterization of a two-phase flow in an operating PEM electrolyzer, comprised of water and evolved O_2, on three different stages of the gas transport namely, on the electrode, through the PTL and in the flow field channels. Images from a flow field channel revealed the dependence of the two-phase flow configurations on the type of pump utilized to circulate water; a transition was observed between bubbly and slug flows that is consistent with the motion cycle of a positive displacement pump. The main effect of the different flow regimes on the operation of a PEM electrolyzer would be on the pressure loss caused to the pump, albeit this energy loss would be significantly small compared to the energy required to drive the PEM electrolysis. We observed two types of bubbles evolving through the pores of a PTL: small bubbles (with a diameter smaller than 50 µm), and bubbles that fill the complete volume of the pore before detaching. The presence of pore-filling bubbles is in line with previously reported findings and collides with the current interpretation of mass transport through PTLs, which predicted the development of two-phase flows in pores, comprised of gas flowing through the center and water close to the walls in porous media. The observation of pore-filling bubbles lead me to conclude that the mass transport losses in PEM electrolyzers might be related to the energy expenditure of gas that displaces water in a hydrophilic pore. I analyzed a series of images of a gas-evolving electrode during operation and found that the average bubble detachment radius is independent of the in-plane water flow. To explain these results, I used a bubble force balance model; I argued that the forces affecting the bubble de-

tachment radius are the forces orthogonal to the bubble growth and that the detachment radius is largely determined by the surface tension force, which in turn is a function of the contact angle of the electrode and the surface tension of the water.

Chapter 4 depicts the gas permeation measurements I carried out in a commonly used PTL in PEM electrolyzers (sintered Ti), following the hypothesis that mass transport losses could be related to gas displacing water, which is a potentially energy-intensive process due to the small pore sizes (14 µm) and the hydrophilic character of the porous Ti substrate. I simulated the operation of a PEM electrolyzer by bubbling gas through a sintered Ti PTL and pumping water on one side of the PTL as is normally done in a PEM electrolysis system. Both H_2 and N_2 (which I assumed to have similar rheological properties as O_2) were forced through the PTL, and the pressure losses of the gas at different stages of the process were measured. The results point at a correlation between water flow and pressure losses, which I modeled using an energy balance that incorporates the permeability of both phases through the porous medium. Pumping water on one side of the PTL seemed to increase the apparent flow path of the gas that tries to displace it; therefore, I utilized the apparent tortuosity (which takes into account the increase in the apparent flow path) to represent the increased pressure losses. I discussed different phenomena where the shear stress of water is used to exert stress on another flow, namely air curtains and water-jet cutters, thereby setting a precedent on the phenomenon I detected. These measurements led me to believe that there can be a methodology to measure the apparent tortuosity and correlate it to the mass transport losses of a real PEM electrolysis working system.

Chapter 5 rounds out this thesis work. I showed the results of measuring mass transport losses in a working PEM electrolysis system, motivated by the findings regarding apparent tortuosity and water flow from the previous chapters. The literature survey presented in chapter 1 revealed that the effects of pressure in PEM electrolyzers has not yet been fully understood; therefore, I explored the potential effect of water flow and pressure on the mass transport

losses using EIS. Both the V(I) curves and EIS measurements showed increased mass transport losses with respect to pressure and water flow for both anode and cathode, being the effect more pronounced on the cathode side. I modeled the results deriving a model that combines the finite-length diffusion in EIS theory with a mass transport model derived for gas-evolving electrodes. Moreover, I proposed a single-parameter equation to calculate the mass transport overpotential, with a parameter (the limiting current density) being a function of measurable variables, obtainable from EIS spectra. The results seemed to agree with the findings from the gas permeation measurements namely, that the apparent tortuosity is proportional to water flow and pressure (more evident for pressure than for water flow). The results from this chapter can potentially serve for future design improvements of PEM electrolyzers that aim at minimizing the effect of operating parameters on the energy losses (in particular mass transport overpotentials).

The motivation for this work arose from a lack of consensus regarding the characterization and modeling of mass transport phenomena in PEM electrolyzers. The key finding of this thesis is that the flow through a PTL pore is not what the literature thinks it to be. Gas permeates through the pores displacing water instead of forming bubbles that allow water to flow in between them or along the pore walls. The primary consequence of this discovery was correlating the gas permeation to mass transport losses; it was apparent that evolved gas from the electrodes needs to exit the system by pushing the incoming water that also fills the pores of the PTLs, causing gas to extract energy from the reaction (or the electric current) to compensate the energy loss of permeation. I found that mass transport losses can occur at both the PTL and at electrode level, and that water flow and pressure cause a non-negligible increase in the mass transport losses; therefore, the choice of operating conditions (in particular pressure and water flow) has to be coupled with the material properties and the PEM electrolyzer design. The results depicted in this thesis can set up a precedent for the PEM electrolysis research to optimize their component

designs, thereby further optimizing PEM electrolyzers with regard to cost and efficiency.

6.2 FURTHER WORK

This work created more questions than answers. The central hypothesis was based on challenging the common understanding of the interaction between gas and liquid in the PTL of a PEM electrolyzer. Several publications have pointed out that no two-phase flow occurs inside pores of sufficiently small size (with a diameter of less than 50 µm); these findings have appeared during simulations of porous structures and have been confirmed by the in-plane imaging of large PTL pores I carried out. Two-phase flows in capillaries have indeed been observed, but the pore diameters that have been researched in the literature are in the order of hundreds of microns and up to 1 mm; therefore, an extrapolation of those observations (to smaller pores) can lead to improper conclusions. Irrefutable evidence can only be obtained by using through-plane imaging i.e., filming the cross-section of a PTL of a functioning PEM electrolyzer via neutron imaging or using a liquid tracer. The principal limitation of such an approach is the need for high resolution images, given that a PTL cross-section is typically thinner than 1 mm (the PTLs I used were 1 mm thick but the industry standard uses much thinner PTLs, < 100 µm).

In my opinion there is a major flaw that often occurs in the PEM electrolysis research namely, that lessons learned from research on homologous solid electrolyte electrochemical devices (PEM fuel cells, for example) is often used directly to explain the results obtained in PEM electrolysis, without acknowledging the underlyingly different phenomena between the different electrochemical devices (in particular regarding transport phenomena and gas-liquid interactions). For example, the first iterations of PTLs for fuel cells consisted of arrangements of metallic meshes of different sizes; consequently, arrangements of metallic meshes have been considered to use in PEM electrolyzers. More often than not, researchers who work in PEM electrolysis are (or were)

active in the PEM fuel cells field, and this leads to skewing of both the experiments that are carried out in PEM electrolysis and the interpretation of the obtained results. Both PEM electrolyzers and PEM fuel cells share similarities in the physico-chemical phenomena that occurs in both processes, but PEM electrolysis needs to be comprehended as a process that has unique governing physical phenomena and its own challenges regarding operation, such as have been showcased in this thesis.

Understanding the multiphase rheology in porous materials can radically change the comprehension of mass transport phenomena in PEM electrolyzers. I showed that there is a correlation between (evolved) gas permeation and pore tortuosity (which is proportional to the mass transport losses). This work proved that mass transport is relevant on both cathode and anode, contrary to the popular opinion in the field that most of the overpotentials in a PEM electrolysis cell occur in the anode. Since the cathode materials and structure were imported from the PEM fuel cells field, there has not been enough attention paid on whether the materials used are optimal for the PEM electrolyzers; further research should be carried out on this topic.

Another topic worthy of investigation is the effect of the surface tension on a PEM electrolysis cell. I pointed out the important role of surface tension on the detachment radius of freely evolving bubbles (i.e., with no PTL); surface tension appears to be the force that dominates the interaction between water and evolved gas. I believe that the next natural step is to assess the effect of changing the surface tension of deionized water on the mass transport losses. Theoretically speaking, an optimal pore size in a PTL would actually show a two-phase flow occurring inside the pore, where the bubbles flow in the middle of the pore and water flows alongside the pore walls but in the opposite direction. Such a flow arrangement does not happen in the common operating conditions of PEM electrolyzers because the surface tension of water is sufficiently small that gas bubbles can grow larger than the PTL pores. Moreover, typical gas bubbles produced on gas-evolving electrodes have diameters between 50 and 100 µm; using a PTL with pore sizes of less than 50 µm would

prevent a bubble from breaking off, favoring the formation of a gas channel that starts at the electrode and gets broken off on the other side of the PTL, after contact with the water in the flow field channels. I showed that an increase in the surface tension can lead to smaller bubbles; thus, future research can attempt to alter the water surface tension to the point that a 50 µm or smaller pore can house a two-phase flow while conserving the plentiful contact between electrode and PTL. The contact angle between water and electrode/PTL also plays a central role in determining the detachment diameter of evolved bubbles, thus there are two interfacial variables that can be researched to find an optimal design and optimal operating conditions for a PEM electrolyzer.

I found PEM electrolysis to be a fascinating subject that requires multidisciplinary knowledge to fully harvest its potential to become a key technology in the renewable energy mixture of the short-term future. It will be well worth it to further invest knowledge and resources on continuing to understand the multifaceted technology that is PEM electrolysis, in particular with regard to the subjects of multiphase rheology and interfacial chemistry.

Part IV

BIBLIOGRAPHY

BIBLIOGRAPHY

[1] A. H. Abdol Rahim, A. S. Tijani, S. K. Kamarudin, and S. Hanapi. "An overview of polymer electrolyte membrane electrolyzer for hydrogen production: Modeling and mass transport." *J. Power Sources* 309 (2016), pp. 56–65. DOI: 10.1016/j.jpowsour.2016.01.012.

[2] R. A. M. Al-Hayes and R. H. S. Winterton. "Bubble diameter on detachment in flowing liquids." *Int. J. Heat Mass Tran.* 24.2 (1981), pp. 223–230. DOI: 10.1016/0017-9310(81)90030-2.

[3] K. Aldas, N. Pehlivanoglu, and M. Mat. "Numerical and experimental investigation of two-phase flow in an electrochemical cell." *Int. J. Hydrogen Energy* 33.14 (2008), pp. 3668–3675. DOI: 10.1016/j.ijhydene.2008.04.047.

[4] F. Arbabi, A. Kalantarian, R. Abouatallah, R. Wang, J. S. Wallace, and A. Bazylak. "Feasibility study of using microfluidic platforms for visualizing bubble flows in electrolyzer gas diffusion layers." *J. Power Sources* 258 (2014), pp. 142–149. DOI: 10.1016/j.jpowsour.2014.02.042.

[5] F. Aubras, J. Deseure, J. J. A. Kadjo, I. Dedigama, J. Majasan, B. Grondin-Perez, J. P. Chabriat, and D. J. L. Brett. "Two-dimensional model of low-pressure PEM electrolyser: Two-phase flow regime, electrochemical modelling and experimental validation." *Int. J. Hydrogen Energy* 42.42 (2017), pp. 26203–26216. DOI: 10.1016/j.ijhydene.2017.08.211.

[6] R. W. Aul and W. L. Olbricht. "Stability of a thin annular film in pressure-driven, low-Reynolds-number flow through a capillary." *J. Fluid Mech.* 215 (1990), p. 585. DOI: 10.1017/S0022112090002774.

[7] K. E. Ayers, E. B. Anderson, C. Capuano, B. Carter, L. Dalton, G. Hanlon, J. Manco, and M. Niedzwiecki. "Research Advances towards Low Cost, High Efficiency PEM Electrolysis." *ECS Trans.* (2010), pp. 3–15. DOI: 10.1149/1.3484496.

[8] F. Barbir. "PEM electrolysis for production of hydrogen from Renew. Energ. sources." *Sol. Energy* 78.5 (2005), pp. 661–669. DOI: 10.1016/j.solener.2004.09.003.

[9] E. Barsoukov and J. R. Macdonald. *Impedance spectroscopy: theory, experiment, and applications*. John Wiley & Sons, 2018. ISBN: 978-1119381860.

[10] J. Bear. *Dynamics of fluids in porous media*. Courier Corporation, 2013. ISBN: 978-0486656755.

[11] H. J. C. Berendsen, J. R. Grigera, and T. P. Straatsma. "The missing term in effective pair potentials." *J. Phys. Chem.* 91.24 (1987), pp. 6269–6271. DOI: 10.1021/j100308a038.

[12] R. Berker. "Intégration des équations du mouvement d'un fluide visqueux incompressible. (French) [Integration of the equations of movement of an incompressible viscous fluid]." *Handbuch der Physik* 3 (1963), pp. 1–384. DOI: 10.1007/978-3-662-10109-4_1.

[13] Q. C. Bi and T. S. Zhao. "Taylor bubbles in miniaturized circular and noncircular channels." *Int. J. Multiphas. Flow* 27.3 (2001), pp. 561–570. DOI: 10.1016/S0301-9322(00)00027-6.

[14] R. B. Bird, W. E. Stewart, and E. N. Lightfoot. *Transport phenomena*. John Wiley & Sons, 2002. ISBN: 978-1118078815.

[15] J. J. Bloomer. *Practical fluid mechanics for engineering applications*. Marcel Dekker New York, 2000. ISBN: 978-0824795757.

[16] F. P. Bretherton. "The motion of long bubbles in tubes." *J. Fluid Mech.* 10.2 (1961), pp. 166–188. DOI: 10.1017/S0022112061000160.

[17] M. Carmo, D. L. Fritz, J. Mergel, and D. Stolten. "A comprehensive review on PEM water electrolysis." *Int. J. Hydrogen Energy* 38.12 (2013), pp. 4901–4934. DOI: 10.1016/j.ijhydene.2013.01.151.

[18] D. Chisholm and D. K. Laird. "Two-phase flow in rough tubes." *Trans. ASME* 80.2 (1958), pp. 276–286.

[19] J. Chun, W. Lee, C. Park, and U. Lee. "Development of the critical film thickness correlation for an advanced annular film mechanistic dryout model applicable to MARS code." *Nucl. Eng. Des.* 223.3 (2003), pp. 315–328. DOI: 10.1016/S0029-5493(03)00079-7.

[20] D. Chung, M. Ebner, D. R. Ely, V. Wood, and R. Edwin García. "Validity of the Bruggeman relation for porous electrodes." *Model. Simul. Mater. Sc.* 21.7 (2013), p. 074009. DOI: 10.1088/0965-0393/21/7/074009.

[21] F. Civan. "Effective Correlation of Apparent Gas Permeability in Tight Porous Media." *Transport Porous Med.* 82.2 (2010), pp. 375–384. DOI: 10.1007/s11242-009-9432-z.

[22] DOE. *The fuel cell technologies office multi-year research, development, and demonstration Plan. 3.1 hydrogen production.* Tech. rep. US Department of Energy, 2015, pp. 1–44.

[23] I. Dedigama, P. Angeli, K. Ayers, J. B. Robinson, P. R. Shearing, D. Tsaoulidis, and D. J. L. Brett. "In situ diagnostic techniques for characterisation of polymer electrolyte membrane water electrolysers – Flow visualisation and electrochemical impedance spectroscopy." *Int. J. Hydrogen Energy* 39.9 (2014), pp. 4468–4482. DOI: 10.1016/j.ijhydene.2014.01.026.

[24] I. Dedigama, P. Angeli, N. van Dijk, J. Millichamp, D. Tsaoulidis, P. R. Shearing, and D. J. L. Brett. "Current density mapping and optical flow visualisation of a polymer electrolyte membrane water electrolyser." *J. Power Sources* 265 (2014), pp. 97–103. DOI: 10.1016/j.jpowsour.2014.04.120.

[25] O. R. Enríquez, C. Sun, D. Lohse, A. Prosperetti, and D. van der Meer. "The quasi-static growth of bubbles." *J. Fluid Mech.* 741 (2014), p. 54. DOI: 10.1017/jfm.2013.667.

[26] M. Espinosa-López, C. Darras, P. Poggi, R. Glises, P. Baucour, A. Rakotondrainibe, S. Besse, and P. Serre-Combe. "Modelling and experimental validation of a 46 kW PEM high pressure water electrolyzer." *Renew. Energ.* 119 (2018), pp. 160–173. DOI: 10.1016/j.renene.2017.11.081.

[27] S. H. Frensch, A. C. Olesen, S. S. Araya, and S. K. Kær. "Model-supported characterization of a PEM water electrolysis cell for the effect of compression." *Electrochim. Acta* 263 (2018), pp. 228–236. DOI: 10.1016/j.electacta.2018.01.040.

[28] D. L. Fritz, J. Mergel, and D. Stolten. "PEM Electrolysis Simulation and Validation." *ECS Trans.* 58.19 (2014), pp. 1–9. DOI: 10.1149/05819.0001ecst.

[29] T. Fukano and A. Kariyasaki. "Characteristics of gas-liquid two-phase flow in a capillary tube." *Nucl. Eng. Des.* 141.1-2 (1993), pp. 59–68. DOI: 10.1016/0029-5493(93)90092-N.

[30] J. C. Garcia-Navarro, M. Schulze, and K. A. Friedrich. "Detecting and modeling oxygen bubble evolution and detachment in proton exchange membrane water electrolyzers." *Int. J. Hydrogen Energy* 44 (2019), pp. 27190–27203. DOI: 10.1016/j.ijhydene.2019.08.253.

[31] J. C. Garcia-Navarro, M. Schulze, and K. A. Friedrich. "Measuring and modeling mass transport losses in proton exchange membrane water electrolyzers using electrochemical impedance spectroscopy." *J. Power Sources* 431 (2019), pp. 189–204. DOI: 10.1016/j.jpowsour.2019.05.027.

[32] J. C. Garcia-Navarro, M. Schulze, and K. A. Friedrich. "Understanding the role of water flow and the porous transport layer on the performance of Proton Exchange Membrane Water Electrolyzers." *ACS Sustain. Chem. Eng.* 7.1 (2019), pp. 1600–1610. DOI: 10.1021/acssuschemeng.8b05369.

[33] H. Giráldez, C. D. Pérez Segarra, I. Rodríguez, and A. Oliva. "Improved semi-analytical method for air curtains prediction." *Energ. Buildings* 66 (2013), pp. 258–266. DOI: 10.1016/j.enbuild.2013.07.011.

[34] S. A. Grigoriev, M. M. Khaliullin, N. V. Kuleshov, and V. N. Fateev. "Electrolysis of water in a system with a solid polymer electrolyte at elevated pressure." *Russ. J. Electrochem+* 37.8 (2001), pp. 819–822. DOI: 10.1023/A:1016735003101.

[35] S. A. Grigoriev, P. Millet, S. A. Volobuev, and V. N. Fateev. "Optimization of porous current collectors for PEM water electrolysers." *Int. J. Hydrogen Energy* 34.11 (2009), pp. 4968–4973. DOI: 10.1016/j.ijhydene.2008.11.056.

[36] S. A. Grigoriev, V. I. Porembskiy, S. V. Korobtsev, V. N. Fateev, F. Auprêtre, and P. Millet. "High-pressure PEM water electrolysis and corresponding safety issues." *Int. J. Hydrogen Energy* 36.3 (2011), pp. 2721–2728. DOI: 10.1016/j.ijhydene.2010.03.058.

[37] S. Grigoriev, V. Porembsky, and V. Fateev. "Pure hydrogen production by PEM electrolysis for hydrogen energy." *Int. J. Hydrogen Energy* 31.2 (2006), pp. 171–175. DOI: 10.1016/j.ijhydene.2005.04.038.

[38] B. Han, J. Mo, Z. Kang, G. Yang, W. Barnhill, and F. Zhang. "Modeling of two-phase transport in proton exchange membrane electrolyzer cells for hydrogen energy." *Int. J. Hydrogen Energy* 42.7 (2017), pp. 4478–4489. DOI: 10.1016/j.ijhydene.2016.12.103.

[39] S. M. Hassanizadeh, M. A. Celia, and H. K. Dahle. "Dynamic Effect in the Capillary Pressure-Saturation Relationship and its Impacts on Unsaturated Flow." *Vadose Zone J.* 1.1 (2002), pp. 38–57. DOI: 10.2113/1.1.38.

[40] T. Hibiki and K. Mishima. "Flow regime transition criteria for upward two-phase flow in vertical narrow rectangular channels." *Nucl. Eng. Des.* 203.2-3 (2001), pp. 117–131. DOI: 10.1016/S0029-5493(00)00306-X.

[41] C. K. Ho and S. W. Webb, eds. *Gas transport in porous media*. Springer, 2006. ISBN: 978-1402039614.

[42] M. Ishii. *One-dimensional drift-flux model and constitutive equations for relative motion between phases in various two-phase flow regimes*. Tech. rep. Argonne National Lab., Ill. (USA), 1977.

[43] H. Ito, T. Maeda, A. Nakano, Y. Hasegawa, N. Yokoi, C. M. Hwang, M. Ishida, A. Kato, and T. Yoshida. "Effect of flow regime of circulating water on a proton exchange membrane electrolyzer." *Int. J. Hydrogen Energy* 35.18 (2010), pp. 9550–9560. DOI: 10.1016/j.ijhydene.2010.06.103.

[44] H. Ito, T. Maeda, A. Nakano, C. M. Hwang, M. Ishida, A. Kato, and T. Yoshida. "Experimental study on porous current collectors of PEM electrolyzers." *Int. J. Hydrogen Energy* 37.9 (2012), pp. 7418–7428. DOI: 10.1016/j.ijhydene.2012.01.095.

[45] H. Ito, T. Maeda, A. Nakano, A. Kato, and T. Yoshida. "Influence of pore structural properties of current collectors on the performance of proton exchange membrane electrolyzer." *Electrochim. Acta* 100 (2013), pp. 242–248. DOI: 10.1016/j.electacta.2012.05.068.

[46] K. Ito, Y. Maeda, T. Sakaguchi, S. Tsukamoto, A. Inada, Y. Tsuchiya, and H. Nakajima. "Analysis and visualization of water flow impact on hydrogen production efficiency in solid polymer water electrolyzer under high-pressure condition." *Int. J. Hydrogen Energy* 40.18 (2015), pp. 5995–6003. DOI: 10.1016/j.ijhydene.2015.03.045.

[47] S. S. Lafmejani, A. C. Olesen, and S. K. Kær. "VOF modelling of gas–liquid flow in PEM water electrolysis cell micro-channels." *Int. J. Hydrogen Energy* 42.26 (2017), pp. 16333–16344. DOI: 10.1016/j.ijhydene.2017.05.079.

[48] A. Lasia. "Electrochemical impedance spectroscopy and its applications." In: *Modern aspects of electrochemistry*. Springer, 2002, pp. 143–248. ISBN: 978-0306469169.

[49] C. H. Lee, R. Banerjee, F. Arbabi, J. Hinebaugh, and A. Bazylak. "Porous Transport Layer Related Mass Transport Losses in Polymer Electrolyte Membrane Electrolysis: A Review." In: *ASME 2016 14th International Conference on Nanochannels, Microchannels, and Minichannels*. ASME, 2016, pp. 1–7. DOI: 10.1115/ICNMM2016-7974.

[50] C. H. Lee, J. Hinebaugh, R. Banerjee, S. Chevalier, R. Abouatallah, R. Wang, and A. Bazylak. "Influence of limiting throat and flow regime on oxygen bubble saturation of polymer electrolyte membrane electrolyzer porous transport layers." *Int. J. Hydrogen Energy* 42.5 (2017), pp. 2724–2735. DOI: 10.1016/j.ijhydene.2016.09.114.

[51] P. Lettenmeier, S. Kolb, N. Sata, A. Fallisch, L. Zielke, S. Thiele, A. S. Gago, and K. A. Friedrich. "Comprehensive investigation of novel pore-graded gas diffusion layers for high-performance and cost-effective proton exchange membrane electrolyzers." *Energy Environ. Sci.* 10.12 (2017), pp. 2521–2533. DOI: 10.1039/C7EE01240C.

[52] H. Li, A. Inada, T. Fujigaya, H. Nakajima, K. Sasaki, and K. Ito. "Effects of operating conditions on performance of high-temperature polymer electrolyte water electrolyzer." *J. Power Sources* 318 (2016), pp. 192–199. DOI: 10.1016/j.jpowsour.2016.03.108.

[53] K. Li and R. N. Horne. "An Experimental and Analytical Study of Steam/Water Capillary Pressure." *SPE Reserv. Eval. Eng.* 4.06 (2001), pp. 477–482. DOI: 10.2118/75294-PA.

[54] Y. Li, Z. Kang, J. Mo, G. Yang, S. Yu, D.A. Talley, B. Han, and F. Zhang. "In-situ investigation of bubble dynamics and two-phase flow in proton exchange membrane electrolyzer cells." *Int. J. Hydrogen Energy* 43.24 (2018), pp. 11223–11233. DOI: 10.1016/j.ijhydene.2018.05.006.

[55] H. Liu, C. O. Vandu, and R. Krishna. "Hydrodynamics of Taylor Flow in Vertical Capillaries: Flow Regimes, Bubble Rise Velocity, Liquid Slug Length, and Pressure Drop." *Ind Eng. Chem. Res.* 44.14 (2005), pp. 4884–4897. DOI: 10.1021/ie049307n.

[56] L. Liu. "The phenomenon of negative frictional pressure drop in vertical two-phase flow." *Int. J. Heat Fluid Fl.* 45 (2014), pp. 72–80. DOI: 10.1016/j.ijheatfluidflow.2013.12.003.

[57] Y. Liu, C. Ji, W. Gu, D. R. Baker, J. Jorne, and H. A. Gasteiger. "Proton Conduction in PEM Fuel Cell Cathodes: Effects of Electrode Thickness and Ionomer Equivalent Weight." *J. Electrochem. Soc.* 157.8 (2010), B1154. DOI: 10.1149/1.3435323.

[58] R. W. Lockhart and R. C. Martinelli. "Proposed correlation of data for isothermal two-phase, two-component flow in pipes." *Chem. Eng. Prog* 45.1 (1949), pp. 39–48.

[59] S. Lubetkin. "The motion of electrolytic gas bubbles near electrodes." *Electrochim. Acta* 48.4 (2002), pp. 357–375. DOI: 10.1016/S0013-4686(02)00682-5.

[60] F. Marangio, M. Santarelli, and M. Cali. "Theoretical model and experimental analysis of a high pressure PEM water electrolyser for hydrogen production." *Int. J. Hydrogen Energy* 34.3 (2009), pp. 1143–1158. DOI: 10.1016/j.ijhydene.2008.11.083.

[61] M. Mat and K. Aldas. "Application of a two-phase flow model for natural convection in an electrochemical cell." *Int. J. Hydrogen Energy* 30.4 (2005), pp. 411–420. DOI: 10.1016/j.ijhydene.2004.04.002.

[62] H. Matsushima, Y. Fukunaka, and K. Kuribayashi. "Water electrolysis under microgravity." *Electrochim. Acta* 51.20 (2006), pp. 4190–4198. DOI: 10.1016/j.electacta.2005.11.046.

[63] P. Medina and M. Santarelli. "Analysis of water transport in a high pressure PEM electrolyzer." *Int. J. Hydrogen Energy* 35.11 (2010), pp. 5173–5186. DOI: 10.1016/j.ijhydene.2010.02.130.

[64] K. Mishima and T. Hibiki. "Some characteristics of air-water two-phase flow in small diameter vertical tubes." *Int. J. Multiphas. Flow* 22.4 (1996), pp. 703–712. DOI: 10.1016/0301-9322(96)00010-9.

[65] J. Mo, Z. Kang, G. Yang, W. Barnhill, F. Zhang, and D. Talley. "Visualization on rapid and micro-scale dynamics of oxygen bubble evolution in PEMECs." In: *2017 IEEE 12th International Conference on Nano/Micro Engineered and Molecular Systems (NEMS)*. IEEE, 2017, pp. 101–105. DOI: 10.1109/NEMS.2017.8016983.

[66] N. Nagai. "Existence of optimum space between electrodes on hydrogen production by water electrolysis." *Int. J. Hydrogen Energy* 28.1 (2003), pp. 35–41. DOI: 10.1016/S0360-3199(02)00027-7.

[67] D. J. Nicklin. "Two-phase bubble flow." *Chem. Eng. Sci.* 17.9 (1962), pp. 693–702. DOI: 10.1016/0009-2509(62)85027-1.

[68] J. Nie and Y. Chen. "Numerical modeling of three-dimensional two-phase gas–liquid flow in the flow field plate of a PEM electrolysis cell." *Int. J. Hydrogen Energy* 35.8 (2010), pp. 3183–3197. DOI: 10.1016/j.ijhydene.2010.01.050.

[69] A. Nouri-Khorasani, E. T. Ojong, T. Smolinka, and D. P. Wilkinson. "Model of oxygen bubbles and performance impact in the porous transport layer of PEM water electrolysis cells." *Int. J. Hydrogen Energy* 42.48 (2017), pp. 28665–28680. DOI: 10.1016/j.ijhydene.2017.09.167.

[70] H. N. Oguz and A. Prosperetti. "Dynamics of bubble growth and detachment from a needle." *J. Fluid Mech.* 257 (1993), p. 111. DOI: 10.1017/S0022112093003015.

[71] E. T. Ojong, J. T. H. Kwan, A. Nouri-Khorasani, A. Bonakdarpour, D. P. Wilkinson, and T. Smolinka. "Development of an experimentally validated semi-empirical fully-coupled performance model of a PEM electrolysis cell with a 3-D structured porous transport layer." *Int. J. Hydrogen Energy* 42.41 (2017), pp. 25831–25847. DOI: 10.1016/j.ijhydene.2017.08.183.

[72] A. Christian Olesen, C. Rømer, and S. K. Kær. "A numerical study of the gas-liquid, two-phase flow maldistribution in the anode of a high pressure PEM water electrolysis cell." *Int. J. Hydrogen Energy* 41.1 (2016), pp. 52–68. DOI: 10.1016/j.ijhydene.2015.09.140.

[73] S. J. Paddison, D. W. Reagor, and T. A. Zawodzinski Jr. "High frequency dielectric studies of hydrated Nafion®." *J. Electroanal. Chem.* 459.1 (1998), pp. 91–97. DOI: 10.1016/S0022-0728(98)00321-0.

[74] E. E. Petersen. "Diffusion in a pore of varying cross section." *AIChE J.* 4.3 (1958), pp. 343–345. DOI: 10.1002/aic.690040322.

[75] B. E. Poling, J. M. Prausnitz, J. P. O'Connell, and R. C. Reid. *The properties of gases and liquids*. McGraw-Hill New York, 2001. ISBN: 978-0070116825.

[76] C. Rakousky, U. Reimer, K. Wippermann, M. Carmo, W. Lueke, and D. Stolten. "An analysis of degradation phenomena in polymer electrolyte membrane water electrolysis." *J. Power Sources* 326 (2016), pp. 120–128. DOI: 10.1016/j.jpowsour.2016.06.082.

[77] A. Roy, S. Watson, and D. Infield. "Comparison of electrical energy efficiency of atmospheric and high-pressure electrolysers." *Int. J. Hydrogen Energy* 31.14 (2006), pp. 1964–1979. DOI: 10.1016/j.ijhydene.2006.01.018.

[78] C. Rozain and P. Millet. "Electrochemical characterization of Polymer Electrolyte Membrane Water Electrolysis Cells." *Electrochim. Acta* 131 (2014), pp. 160–167. DOI: 10.1016/j.electacta.2014.01.099.

[79] R. Sander. "Compilation of Henry's law constants (version 4.0) for water as solvent." *Atmos. Chem. Phys.* 15.8 (2015). DOI: 10.5194/acpd-14-29615-2014.

[80] M. Santarelli, P. Medina, and M. Cali. "Fitting regression model and experimental validation for a high-pressure PEM electrolyzer." *Int. J. Hydrogen Energy* 34.6 (2009), pp. 2519–2530. DOI: 10.1016/j.ijhydene.2008.11.036.

[81] L. W. Schwartz, H. M. Princen, and A. D. Kiss. "On the motion of bubbles in capillary tubes." *J. Fluid Mech.* 172 (1986), p. 259. DOI: 10.1017/S0022112086001738.

[82] Ö. F. Selamet, M. C. Acar, M. D. Mat, and Y. Kaplan. "Effects of operating parameters on the performance of a high-pressure proton exchange membrane electrolyzer." *Int. J. Energ. Res.* 37.5 (2013), pp. 457–467. DOI: 10.1002/er.2942.

[83] Ö. F. Selamet, F. Becerikli, M. D. Mat, and Y. Kaplan. "Development and testing of a highly efficient proton exchange membrane (PEM) electrolyzer stack." *Int. J. Hydrogen Energy* 36.17 (2011), pp. 11480–11487. DOI: 10.1016/j.ijhydene.2011.01.129.

[84] Ö. F. Selamet, U. Pasaogullari, D. Spernjak, D. S. Hussey, D. L. Jacobson, and M. Mat. "In Situ Two-Phase Flow Investigation of Proton Exchange Membrane (PEM) Electrolyzer by Simultaneous Optical and Neutron Imaging." *ECS Trans.* (2011), pp. 349–362. DOI: 10.1149/1.3635568.

[85] D. Shapiro, J. Duffy, M. Kimble, and M. Pien. "Solar-powered regenerative PEM electrolyzer/fuel cell system." *Sol. Energy* 79.5 (2005), pp. 544–550. DOI: 10.1016/j.solener.2004.10.013.

[86] S. Siracusano, V. Baglio, N. Briguglio, G. Brunaccini, A. Di Blasi, A. Stassi, R. Ornelas, E. Trifoni, V. Antonucci, and A. S. Aricò. "An electrochemical study of a PEM stack for water electrolysis." *Int. J. Hydrogen Energy* 37.2 (2012), pp. 1939–1946. DOI: 10.1016/j.ijhydene.2011.06.019.

[87] S. Siracusano, S. Trocino, N. Briguglio, V. Baglio, and A. Aricò. "Electrochemical impedance spectroscopy as a diagnostic tool in polymer electrolyte membrane electrolysis." *Materials* 11.8 (2018), p. 1368. DOI: 10.3390/ma11081368.

[88] K. Sirén. "Technical dimensioning of a vertically upwards blowing air curtain—part I." *Energ. Buildings* 35.7 (2003), pp. 681–695. DOI: 10.1016/S0378-7788(02)00223-2.

[89] D. Spernjak, A. K. Prasad, and S. G. Advani. "Experimental investigation of liquid water formation and transport in a transparent single-serpentine PEM fuel cell." *J. Power Sources* 170.2 (2007), pp. 334–344. DOI: 10.1016/j.jpowsour.2007.04.020.

[90] T. E. Springer, T. A. Zawodzinski, and S. Gottesfeld. "Polymer electrolyte fuel cell model." *J. Electrochem. Soc.* 138.8 (1991), pp. 2334–2342. DOI: 10.1149/1.2085971.

[91] D. Stolten, ed. *Hydrogen and Fuel Cells: Fundamentals, Technologies and Applications*. Wiley-VCH, 2010. ISBN: 978-3527327119.

[92] M. Suermann, A. Pătru, T. J. Schmidt, and F. N. Büchi. "High pressure polymer electrolyte water electrolysis: Test bench development and electrochemical analysis." *Int. J. Hydrogen Energy* 42.17 (2017), pp. 12076–12086. DOI: 10.1016/j.ijhydene.2017.01.224.

[93] M. Suermann, T. J. Schmidt, and F. N. Büchi. "Investigation of Mass Transport Losses in Polymer Electrolyte Electrolysis Cells." *ECS Trans.* 69.17 (2015), pp. 1141–1148. DOI: 10.1149/06917.1141ecst.

[94] M. Suermann, T. J. Schmidt, and F. N. Büchi. "Cell Performance Determining Parameters in High Pressure Water Electrolysis." *Electrochim. Acta* 211 (2016), pp. 989–997. DOI: 10.1016/j.electacta.2016.06.120.

[95] S. Takagi, A. Prosperetti, and Y. Matsumoto. "Drag coefficient of a gas bubble in an axisymmetric shear flow." *Phys. Fluids* 6.9 (1994), pp. 3186–3188. DOI: 10.1063/1.868097.

[96] A. S. Tijani and A. H. Abdol Rahim. "Numerical Modeling the Effect of Operating Variables on Faraday Efficiency in PEM Electrolyzer." *Proc. Tech.* 26 (2016), pp. 419–427. DOI: 10.1016/j.protcy.2016.08.054.

[97] K. A. Triplett, S. M. Ghiaasiaan, S. I. Abdel-Khalik, and D. L. Sadowski. "Gas–liquid two-phase flow in microchannels Part I: two-phase flow patterns." *Int. J. Multiphas. Flow* 25.3 (1999), pp. 377–394. DOI: 10.1016/S0301-9322(98)00054-8.

[98] K. Tüber, D. Pócza, and C. Hebling. "Visualization of water buildup in the cathode of a transparent PEM fuel cell." *J. Power Sources* 124.2 (2003), pp. 403–414. DOI: 10.1016/S0378-7753(03)00797-3.

[99] H. Vogt. "The problem of the departure diameter of bubbles at gas-evolving electrodes." *Electrochim. Acta* 34.10 (1989), pp. 1429–1432. DOI: 10.1016/0013-4686(89)87183-X.

[100] H. Vogt. "On the gas-evolution efficiency of electrodes I – Theoretical." *Electrochim. Acta* 56.3 (2011), pp. 1409–1416. DOI: 10.1016/j.electacta.2010.08.101.

[101] H. Vogt and R. J. Balzer. "The bubble coverage of gas-evolving electrodes in stagnant electrolytes." *Electrochim. Acta* 50.10 (2005), pp. 2073–2079. DOI: 10.1016/j.electacta.2004.09.025.

[102] H. Vogt and K. Stephan. "Local microprocesses at gas-evolving electrodes and their influence on mass transfer." *Electrochim. Acta* 155 (2015), pp. 348–356. DOI: 10.1016/j.electacta.2015.01.008.

[103] J. Wang. "Predictive depth of jet penetration models for abrasive water-jet cutting of alumina ceramics." *Int. J. Mech. Sci.* 49.3 (2007), pp. 306–316. DOI: 10.1016/j.ijmecsci.2006.09.005.

[104] J. R. Welty, C. E. Wicks, G. Rorrer, and R. E. Wilson. *Fundamentals of momentum, heat, and mass transfer*. John Wiley & Sons, 2009. ISBN: 978-0470504819.

[105] F. Weng, A. Su, and C. Hsu. "The study of the effect of gas stoichiometric flow rate on the channel flooding and performance in a transparent fuel cell." *Int. J. Hydrogen Energy* 32.6 (2007), pp. 666–676. DOI: 10.1016/j.ijhydene.2006.06.066.

[106] H. Yang, T. S. Zhao, and Q. Ye. "In situ visualization study of CO2 gas bubble behavior in DMFC anode flow fields." *J. Power Sources* 139.1-2 (2005), pp. 79–90. DOI: 10.1016/j.jpowsour.2004.05.033.

[107] F. Y. Zhang, X. G. Yang, and C. Y. Wang. "Liquid water removal from a polymer electrolyte fuel cell." *J. Electrochem. Soc.* 153.2 (2006), A225–A232. DOI: 10.1149/1.2138675.

[108] M. Zhang, L. Pan, P. Ju, X. Yang, and M. Ishii. "The mechanism of bubbly to slug flow regime transition in air-water two phase flow: A new transition criterion." *Int. J. Heat Mass Tran.* 108 (2017), pp. 1579–1590. DOI: 10.1016/j.ijheatmasstransfer.2017.01.007.

[109] W. G. J. van Helden, C. W. M. van der Geld, and P. G. M. Boot. "Forces on bubbles growing and detaching in flow along a vertical wall." *Int. J. Heat Mass Tran.* 38.11 (1995), pp. 2075–2088. DOI: 10.1016/0017-9310(94)00319-Q.

Part V

APPENDIX

APPENDIX

A.1 IMPEDANCE SPECTROSCOPY OF MASS TRANSPORT PHENOMENA

A.1.1 *Typical fit of the equivalent circuit*

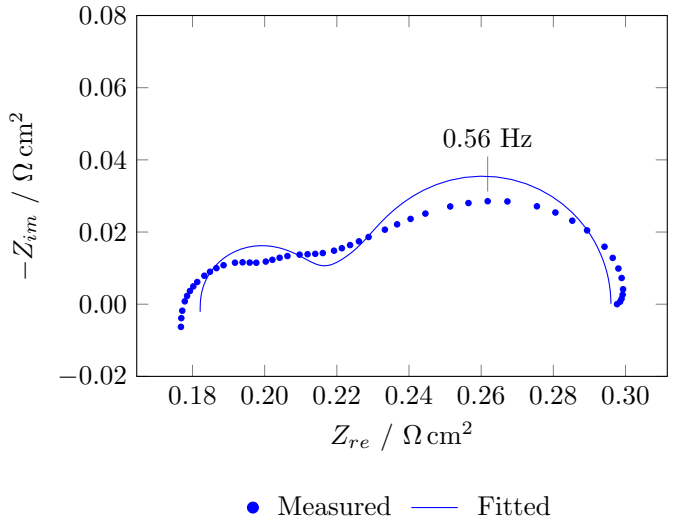

Figure A.1: Typical fit of a measured EIS spectrum (dots) to the equivalent circuit depicted in Figure 5.1 (line). I decided to use the equivalent circuit from Figure 5.1 to minimize the number of fitted parameters, especially since I was primarily interested in the frequencies below 1 Hz.

A.1.2 *Fitted EIS data*

Electrode	ϕ_w or P	L_1	R_s	R_{ct}	W	k	C_{dl}
	$l\,h^{-1}$ or bar	nH	mΩ	mΩ	$m\Omega\,s^{-0.5}$	s^{-1}	F
Anode	1	2.65	8.11	1.00	1.87	1.07	0.80
	2	2.78	8.45	1.04	2.32	1.13	0.75
	3	2.72	8.70	1.10	2.49	1.05	0.71
	4	2.73	8.68	1.14	2.63	1.00	0.72
	5	2.84	8.46	1.12	2.72	1.05	0.70
	6	2.92	8.35	1.15	2.75	0.99	0.73
Cathode	1	2.73	8.21	1.09	2.81	1.24	0.67
	2	2.57	8.59	1.22	3.33	1.11	0.67
	3	2.44	8.84	1.26	4.11	1.12	0.62
	4	2.43	8.88	1.30	4.19	1.15	0.62
	5	2.38	8.97	1.33	4.43	1.09	0.60
	6	2.36	9.02	1.39	4.68	1.10	0.62
Anode	0	1.78	8.05	1.02	2.00	1.24	0.83
	1	1.79	8.00	1.01	1.97	1.26	0.87
	2	1.82	7.99	1.00	1.97	1.30	0.88
	3	1.82	8.02	0.99	1.98	1.34	0.84
	4	2.08	7.95	1.00	1.90	1.66	0.97
	5	2.13	8.02	1.01	1.98	1.74	0.90
Cathode	0	2.67	7.85	1.06	2.23	1.07	0.81
	1	2.94	7.75	1.02	2.32	1.18	0.90
	2	3.06	7.70	1.09	2.69	1.17	0.55
	3	3.09	7.79	1.10	2.98	1.15	0.92
	4	3.14	7.86	1.13	3.46	1.15	0.92
	5	3.13	7.91	1.25	3.91	1.16	0.93

Table A.1: Averaged EIS parameters, obtained from fitting the measured EIS spectra at different water flows (top, see Figure 5.4) and pressures (bottom, see Figure 5.5) to the equivalent circuit depicted in Figure 5.1.

ABOUT THE AUTHOR

Julio César García Navarro was born in 1989 in Mexico City, Mexico. He attended the National Autonomous University of Mexico, where he studied Chemical Engineering and minored in rheology and polymer processing, and graduated *cum laude* in 2012. Afterwards, he emigrated to the Netherlands to attend Delft University of Technology, where he obtained a Master of Science degree in Sustainable Energy Technology in 2014. His thesis presented the derivation of a non-equilibrium thermodynamics model of a PEM fuel cell, and he obtained a *cum laude* distinction for his work. During his Master studies, he was named "Best Student of his Cohort" by the director of the study program. During his studies regarding sustainable energy, he developed an affinity for electrochemistry, in particular for hydrogen-based electrochemical devices, which led him to the German Aerospace Center in Stuttgart, Germany, to pursue a PhD in PEM electrolysis. Between 2015 and 2018 he carried out his PhD research at the Institute of Engineering Thermodynamics of the German Aerospace Center under the supervision of Prof. K. Andreas Friedrich, and this thesis is the product of his work. After completing his PhD studies, he obtained a position as R&D Manager at HyET Hydrogen in Arnhem, the Netherlands, where he is working on developing electrochemical hydrogen compressors based on his previous experience with PEM-based technologies.